Growth kinetics evaluation of hydrothermally synthesised $Co_2(OH)_3Cl$ nanoparticles for application in solar thermal heat transfer fluids

by

Patricia Tshibasu Ntumba

Thesis submitted in fulfilment of the requirements for the degree

Master of Engineering: Chemical Engineering

In the Faculty of Engineering

At the Cape Peninsula University of Technology

Supervisor: Ass. Prof. Veruscha Fester

Co-Supervisor: Dr. Betrand Sone

Co-Supervisor: Dr. Saleh Khamlich

Bellville campus

January 2024

CPUT copyright information

The thesis may not be published either in part (in scholarly, scientific or technical journals), or as a whole (as a monograph), unless permission has been obtained from the University

DECLARATION

I, Patricia Tshibasu Ntumba, declare that the contents of this thesis represent my own unaided work, and that the thesis has not previously been submitted for academic examination towards any qualification. Furthermore, it represents my own opinions and not necessarily those of the Cape Peninsula University of Technology.

5th January 2024

Signed

Date

ABSTRACT

Nanofluids are advanced heat transfer fluids utilized to enhance the properties of common fluids used in solar thermal collectors. Prior experimental studies demonstrated the dependency of the thermal conductivity and viscosity of different nanofluids on their particle size, shape, concentration, material, hosting fluid properties, acidity (pH value), additives and fluid temperature. Co_3O_4 nanoparticles of higher aspect ratio have been reported to enhance the thermal conductivity of their water based nanofluids. Moreover, it has been reported that the synthesis of cobalt oxide nanoparticles in the presence of different propanol concentrations can significantly alter their size, thus improving the properties of the resulting nanofluids. Despite numerous studies investigating its applications in the energy storage industry, cobalt hydroxychloride, a precursor to cobalt oxide, has never been used as nano-heat transfer fluid. The impact of propanol concentration on the size of cobalt oxide nanoparticles has been studied, but no similar study has been conducted for cobalt hydroxychloride. Although the relationship between the thermal conductivity of cobalt oxide nanoparticle-based nanofluids and the impact of their shape has been previously documented, there has been no other study exploring the utilization of cobalt hydroxychloride nanoparticles in nanofluid applications. Conflicting trends about the impact of particle size and shape on the viscosity of various aqueous nanofluids show the need to investigate the influence of cobalt hydroxychloride particle size and shape on the viscosity of their nanofluids. A simultaneous Ostwald ripening (OR) and oriented attachment (OA) based growth of cobalt hydroxychloride micro/nanostructures in the presence of triethanolamine/water solvent has been reported. Therefore, time course experiments have been conducted to understand the growth of cobalt hydroxychloride in the presence of propanol and water.

In the presence of cobalt chloride hexahydrate, cobalt hydroxychloride nanopowders were synthesised in pure water and solutions of pure propanol at concentrations ranging from 10% to 100%. A synthesis temperature and time of 105 ±5 °C and 6 h were maintained. The resulting powders were characterised using HR-TEM, XRD, ATR-FTIR and UV-VIS-NIR after their dispersion in pure water then, their thermal conductivity and viscosity were measured. In the presence of cobalt chloride hexahydrate, cobalt hydroxychloride nanopowders were synthesised in 70% propanol concentration solvent and pure water. Synthesis times were varied from 60 min to 960 min for both solvents, but at a constant synthesis temperature of 105 ±5 °C. The resulting powders were characterised using XRD and HR-TEM. Both pink and lavender β-cobalt hydroxychloride nanoparticles were produced from propanol concentrations ranging from 70% to 100%. Green nanopowders of mixed phases were encountered for the rest of propanol concentrations. A conversion of the shape of cobalt hydroxychloride particles from hexagonal nano-plates to spherical-shaped nanoparticles

occurred at 70% propanol concentration. Contrary to a prior trend, increasing propanol concentration from 0% to 100% led to the size reduction of cobalt hydroxychloride nanoparticles. Time dependent experiments revealed that changing the solvent medium from water to 70% propanol while retaining the same processing time modify the morphology of cobalt hydroxychloride from hexagonal nanoplate to spherical. However, the morphology of cobalt hydroxychloride was not altered despite the change in solvent medium from pure water to water:propanol solution (30:70)% at aging times ranging from 9h to 16h. The production of smaller spherical cobalt hydroxychloride particles in the presence of 70% propanol was achieved at reaction times ranging from 1 h to 6 h. In water, cobalt hydroxychloride nanoplates grew first via OR kinetics then OA kinetics while a simultaneous OR and OA growth kinetics occurred for nanospheres. In propanol, the growth of cobalt hydroxychloride nanospheres were controlled first by OR kinetics, then by OA kinetics.

An increase in temperature led to reducing the viscosity of cobalt hydroxychloride nanofluids while increasing their thermal conductivity. All cobalt hydroxychloride nanofluids displayed absorption peaks in the near infrared region and a considerable increase in light absorption in the visible range compared to water, demonstrating their potential solar absorption ability. At 303 K, the cobalt hydroxychloride nanofluid made of cobalt hydroxychloride nanoplates at ~58 nm displayed the highest increase in viscosity of ~11%. The thermal conductivity of the nanofluid made of cobalt hydroxychloride nanospheres at ~10 nm exhibited the highest augmentation in thermal conductivity at all temperatures with ~14% at 308 K. The thermal conductivity enhancement was due to the Brownian motion-induced convection mechanism. The thermal conductivity enhancement of the aqueous nanofluids was affected by the cobalt hydroxychloride particle size while their viscosity increase was rather affected by the shape of cobalt hydroxychloride.

DEDICATION

To my loving parents,

Joseph Tshibasu and Brigitte Lusamba Tshibasu

To my dearest siblings,

Melissa, Benita and Elie Tshibasu

My sincere gratitude goes out to you for all the love, prayers, sacrifices, and encouragements you have shown me since the beginning of this project. I love you all deeply.

ACKNOWLEDGEMENTS

I wish to thank:

- God Almighty for granting me good health, courage and strength which allowed me to complete this project. In spite of the many challenges, I faced throughout this project, God has always made a way out for me and for that I give him all the glory.
- Professor Veruscha Fester, for giving me the opportunity to pursue this degree under her guidance. I appreciate all the advice and support you provided which motivated me to do better.
- Dr Bertrand Sone, for his advice and assistance.
- Dr Saleh Khamlich (CPUT) for helping with thermal conductivity measurements.
- Dr Solly Motaung (CSIR) for XRD and TEM characterisation.
- Dr Nasheeta Hanief (UCT) for assisting with TEM characterisation.
- Dr Remy Bucher (iThemba labs) for his assistance with XRD analysis.
- Dr Steve Tshilumbu from FPRC (CPUT), for helping with viscosity measurements.
- Ms Whitney Heuvel (PhD student at CPUT) for her assistance during this project.
- Mrs Wendy Heuvel for her aid in acquiring the purchase orders for nanoparticle analyses.
- All my fellow students from CPUT, for their encouraging words.

The financial assistance of the Cape Peninsula University of Technology (CPUT) towards this research is acknowledged. Opinions expressed in this thesis and the conclusions arrived at, are those of the author, and are not necessarily to be attributed to the Cape Peninsula University of Technology (CPUT).

TABLE OF CONTENTS

LIST OF FIGURES

LIST OF TABLES

TERMS AND CONCEPTS

Brownian motion: a phenomenon describing the random movement of particles suspended in a fluid.

Growth kinetics: refers to the rate at which the number of individual particles changes in a given system.

Hydrothermal synthesis: A synthesis method for the formation of crystallized nanomaterials by using high temperature aqueous solutions at high pressure.

Nanofluid: refers to a fluid consisting in a mixture of base fluid and nanoparticles.

Nanoparticle: a particle that is 100 nm or smaller in size.

Oriented attachment: the spontaneous growth and self-organization of neighbouring nanocrystals, leading to crystal growth through the addition of solid nanoparticles that possess a shared crystallographic orientation.

Ostwald ripening: is a process in which larger particles in a mixture grow at the expense of smaller ones. In short, it is the phenomenon where small particles dissolve and redeposit onto larger particles.

Rheological properties: properties related to the flow behaviour of materials or their response when submitted to applied forces.

Solar thermal heat transfer fluid: a superior thermal-fluid utilized to carry heat through solar thermal collectors.

Thermal properties: are thermophysical properties associated with the material-dependent response when heat is supplied to it.

ABBREVIATIONS AND ACRONYMS

ATR-FTIR: Attenuated Total Reflectance-Fourier Transform Infrared

CTAB: Cetyltrimethyl ammonium bromide

DIW: Deionised water

DLVO: Derjaguin, Landau, Verwey, and Overbeek

EG: Ethylene glycol

IUPAC: International Union of Pure and Applied Chemistry

ICDD: International Centre for Diffraction Data

JCPDS: Joint Committee on Powder Diffraction Standards

LSW: Lifshitz-Slyozov-Wagner

OA: Oriented attachment

OR: Ostwald ripening

PEG: Polyethylene glycol

PSD: Particle size distribution

STC: Solar thermal collectors

TEM: Transmission electron microscopy

UV-VIS-NIR: Ultraviolet-visible and near-infrared

VEROS: Vacuum evaporation onto a running oil substrate

CHAPTER 1 INTRODUCTION

1.1 Background and motivation

Energy generation from unsustainable sources (coal, petroleum) is one of the major challenges facing society today. Moreover, the global dependence on unsustainable sources brings another problem, namely associated emissions (Höök & Tang, 2013). Consequently, sustainable energy sources such as solar energy are gaining ground over unsustainable resources (Shafiee & Topal, 2009). According to Rashidi et al. (2017), solar energy use can provide humans with all the energy they need over an entire year with little impact on the environment. One of the principal methods for collecting solar energy is through solar thermal collectors (STCs) where the collected energy is converted into thermal energy (Suman et al., 2015) then, transferred to a working fluid (a gas or liquid) flowing inside the tubes attached to the absorber plate. The efficiency of STC systems is dependent on how effective the used solar receivers in STCs captures solar energy, and how effectively the thermal energy or heat is transferred to the working fluid (Otanicar et al., 2010). To address the considerable heat losses from the absorber plate to the surroundings in conventional STCs, Minardi and Chuang (1975) developed direct absorption receiver based STC system which absorb solar flux directly within the fluid volume. However, conventional fluids (water, ethylene glycol, etc.) used in direct absorption or volumetric STC have been reported to exhibit poor thermal conductivity and low optical properties over the solar spectrum range (Li et al., 2020). Nanotechnology has enabled the development of nanosized particles (nanoparticles) that possess superior properties. Thus, nanoparticles were added to conventional fluids in volumetric STC to enhance the thermal and optical properties of the working liquid (Otanicar et al., 2009; Otanicar et al., 2010). Generally, nanofluids, as initially discovered by Choi and Eastman (1995), represent an advanced category of fluids formed by dispersing nano-sized particles, typically ranging in size from 1 to 100 nm, within conventional fluids (e.g., water, ethylene glycol, etc.)

Different nanoparticles are available on the market for nanofluid formulation including metals, metal oxides, carbon materials (carbon nanotube, graphene, etc.), carbides and nitrides (Suganthi & Rajan, 2017). Transition metal oxides nanoparticles have attracted the attention of many researchers because of their magnetic, optical, catalytic, and electronic properties (Sinkó et al., 2011). Cobalt (II, III) oxide (Co_3O_4) which is both a magnetic and transition metal oxide has been applied as light absorber and hole transporting layer in all-oxide photovoltaic and polymer solar cells (Kupfer et al., 2015; Wang et al., 2015). The incorporation of nanoparticles dramatically enhances the thermophysical properties of nanofluids (Patil et al., 2016). Thermal conductivity and viscosity are two of the most studied thermophysical properties of nanofluids because of their impact on the thermal efficiency of

STC systems (Yu et al., 2008; Özerinç et al., 2010; Kleinstreuer & Feng, 2011; Sundar et al., 2013). Nanofluids containing Co_3O_4 nanoparticles dispersed in water have been studied for their thermal conductivity and viscosity (Sekhar et al., 2017; Sekhar et al., 2018; Mitra et al., 2021; Alsboul et al., 2022; Manoram & Moorthy, 2022). Among the most influential parameters affecting the thermal conductivity and viscosity are particle concentration, particle size, particle shape and temperature (Karimi-Nazarabad et al., 2015; Sarviya & Fuskele, 2017). Thermal conductivity of water based Co_3O_4 nanofluids increased with increasing nanoparticle concentration and temperature. In contrast, the viscosity of Co_3O_4 nanofluids increased with decreasing temperature and increasing particle concentration. Mitra et al. (2021) prepared rod-based nanofluids with nanorods of 27 nm in size, while nanoflowers with 32 nm in size were used for flower-based nanofluids. Rod-based Co_3O_4 nanofluids exhibited higher thermal conductivity due to the higher aspect ratios of nanorods (Gu et al., 2013) resulting in an increased contact area with the heat source, and hence increased heat transfer rates (Ghosh et al., 2013). The authors, however, did not discuss the effect of nanoparticle size on thermal conductivity enhancement of Co_3O_4 nanofluids. Furthermore, no study investigated the impact of Co_3O_4 particle size and shape on the viscosity of their nanofluids. Among the methods used to synthesize Co_3O_4 nanoparticles is the synthesis of solid cobalt precursors followed by their calcination to produce Co_3O_4 nanoparticles (Nassar & Ahmed, 2011). The synthesis of Co_3O_4 nanoparticles from the calcination of $Co_2(OH)_3Cl$ nanoparticles has been reported (Cui et al., 2009; Yang et al., 2010; Mansournia & Rakhshan, 2017; Meng & Deng, 2017; Ranganatha et al., 2017). $Co_2(OH)_3Cl$ is part of the family of cobalt layered basic salts and has different uses including electrode materials for batteries, electrochemical supercapacitors, microwave absorbers and catalysts (Ma et al., 2014; Zhao et al., 2019; Wang et al., 2020; Ma et al., 2021). Furthermore, cobalt hydroxychloride ($Co_2(OH)_3Cl$) has also been studied due to the significant electric, magnetic, and catalytic properties of Co_3O_4 formed upon their thermal decomposition (Ma et al., 2017; Mansournia & Rakhshan, 2017; Meng & Deng, 2017). It has been shown that the use of alcohols can control the nanoparticle size and shape, since the properties of alcohols change as the alkyl chain length increases (He et al., 2004a; Athawale et al., 2010; Chowdhury et al., 2014). Heuvel et al. (2021) synthesised Co_3O_4 rhombic like particles by dissolving $CoCl_2.6H_2O$ in different alcohols (methanol, ethanol, propanol, butanol and octanol) at 50% and 100% concentrations. Co_3O_4 nanoparticle size increased with increasing alcohol concentration. For instance, the size of Co_3O_4 nanoparticles increased from 34 nm to 66 nm with propanol concentration increase from 50% to 100%, respectively. This shows that the use of propanol during the synthesis of nanoparticles can provide a means of control over their size, thus improving the properties of the resulting nanofluids.

1.2 Research problem

STC systems are being investigated as a potential sustainable solution for harnessing solar energy, aiming to generate both useful heat and electrical energy. The efficiency of these systems in transferring the generated heat for various technological applications is significantly influenced by the choice and performance of the used heat transfer fluids (HTFs). HTFs containing nanoparticles (also known as nanofluids) have been shown to demonstrate enhanced heat absorption and heat transfer properties depending on the size, shape, and concentration of nanoparticles in the base fluid. Similarly, to several metal oxide nanoparticles, Co_3O_4 nanoparticles have been dispersed in heat transfer fluids and then studied for their viscosity and thermal conductivity as functions of temperature, particle shape and particle concentration. However, for $Co_2(OH)_3Cl$ nanofluids, the relationship between the particle size and shape of $Co_2(OH)_3Cl$ nanoparticles, and the viscosity and thermal conductivity of their resultant nanofluids has not been investigated systematically in one study. This study undertakes to accomplish this, by first understanding how to achieve controlled synthesis of $Co_2(OH)_3Cl$ nanoparticles of desired sizes and shapes, then investigating the effect of temperature, particle size and shape on the viscosity and thermal conductivity of the ensuing $Co_2(OH)_3Cl$ nanofluids. The attainment of these objectives will pave the way for the possibility of synthesising $Co_2(OH)_3Cl$ based nanofluids at industrial scale for application in solar thermal technologies.

1.3 Research question

What is the effect of propanol on the growth kinetics of $Co_2(OH)_3Cl$ nanoparticles prepared under different hydrothermal processing conditions (of varying solvent ratios and synthesis time)? What are the thermal and rheological properties of the resultant $Co_2(OH)_3Cl$ nanofluids ? What is the relationship between thermal conductivity of $Co_2(OH)_3Cl$ nanofluids and the size, shape of $Co_2(OH)_3Cl$ nanoparticles in solution.

1.4 Aims and objectives

The aim of this research is to investigate the effect of propanol in various mixed solvents ratio, and reaction times on the growth kinetics of $Co_2(OH)_3Cl$ nanoparticles during hydrothermal synthesis, as well as the application of $Co_2(OH)_3Cl$ nanoparticles as solar heat transfer fluid.

The objectives are as follows:

1. To investigate the effect of propanol on the $Co_2(OH)_3Cl$ crystal growth kinetics under different hydrothermal processing conditions (solvent ratio and synthesis time).
2. To investigate the temperature-dependent viscosity of $Co_2(OH)_3Cl$ nanofluids and analyse its variation concerning particle size and shape.

3. To measure the thermal conductivity of $Co_2(OH)_3Cl$ nanofluids as functions of temperature, particle size and shape.
4. To establish the relationship between the viscosity of $Co_2(OH)_3Cl$ nanofluids and the size, shape of $Co_2(OH)_3Cl$ nanoparticles in solution as well as temperature.
5. To establish the relationship between the thermal conductivity of $Co_2(OH)_3Cl$ nanofluids and the size, shape of $Co_2(OH)_3Cl$ nanoparticles in solution and temperature.

1.5 Significance

This research will result in the development of $Co_2(OH)_3Cl$ nano-heat transfer fluid to enhance the heat transfer properties of a conventional fluid for application in solar energy harvesting devices. This project will help to better understand the growth mechanisms as well as the factors that facilitate controlled synthesis of $Co_2(OH)_3Cl$ nanoparticles of desired sizes and shapes. Moreover, this research aims to enhance solar energy harvesting, diversify the applications of $Co_2(OH)_3Cl$ nanopowders, and establish a manufacturing facility for synthesizing $Co_2(OH)_3Cl$ nanoparticles. Ultimately, the transition of this research from laboratory experimentation to industrial implementation holds the potential to create essential employment opportunities in South Africa.

1.6 Delineation

This work will not consist in the synthesis of $Co_2(OH)_3Cl$ nanoparticles hybrids or those coupled with other elements or compounds. Only the synthesis of $Co_2(OH)_3Cl$ nanoparticles in the presence of varying mixed solvent ratios (propanol/water) forms part of this research. Further testing of the nanofluid in pilot solar thermal technologies falls outside the scope of this work.

1.7 Organisation of the thesis

This thesis is structured in different chapters as follows:

Chapter 1: Introduction

Chapter 2: Literature review

The use, properties of $Co_2(OH)_3Cl$ and Co_3O_4 nanoparticles, prior literature on the growth mechanisms of $Co_2(OH)_3Cl$ and Co_3O_4 nanoparticles, as well as the effects of various synthesis parameters on their growth are covered. This chapter also comprises former research on the stability and measurements of Co_3O_4 nanofluids properties.

Chapter 3: Research methodology

The preparation of $Co_2(OH)_3Cl$ nanoparticles via the hydrothermal route at different processing conditions are presented in detail. The procedures used for the preparation of

$Co_2(OH)_3Cl$ nanofluids and the measurement of their properties are described in detail. In addition, the characterisation techniques used in each part are presented.

Chapter 4: Effects of propanol on the characteristics and growth kinetics of $Co_2(OH)_3Cl$ nanoparticles

This chapter provides the results obtained from the effect of propanol concentration on the phase, size and shape of $Co_2(OH)_3Cl$ nanoparticles, at constant synthesis temperature and time. The effect of propanol concentration on the growth of $Co_2(OH)_3Cl$ nanoparticles at different synthesis times is also reported.

Chapter 5: Impacts of particle size/shape and temperature on the properties of $Co_2(OH)_3Cl$ nanofluids

Results from the change in $Co_2(OH)_3Cl$ particle size and shape on the viscosity and thermal conductivity of their aqueous nanofluids were provided. The results obtained from measuring the viscosity and thermal conductivity of $Co_2(OH)_3Cl$ nanofluids at varying temperature were also presented.

Chapter 6: Conclusions

Outlines the conclusions of the study and provides recommendations for future research.

CHAPTER 2 LITERATURE REVIEW

2.1 Introduction

STC systems convert solar energy into heat that is widely used in applications such as domestic and industrial heating (Evangelisti et al., 2019). Nevertheless, the utilization of solar energy presents several challenges, including high initial costs and the relatively low efficiency seen in traditional STCs (Otanicar et al., 2010; Gupta et al., 2015). This reduced efficiency is often attributed to the inherently low thermal conductivity of conventional heat transfer fluids such as water, air, and thermal oils. Micron-sized particles were dispersed in fluids to enhance their thermal conductivity, but they generated some problems, such as particle settling, pipe clogging, abrasion of devices, etc. (Yoo et al., 2007). It was reported that nanoparticles exhibit large surface-to-volume ratios, which can result in a significant enhancement of the thermal conductivity of fluids (Hong et al., 2005). Different nanosized particles including metals, metal oxides, and carbon nanotubes can be dispersed in common fluids. Metal oxide nanoparticles are the most applicable materials for nanofluid preparation because they are chemically stable, less prone to oxidation (Saidina et al., 2020) and settle less during nanofluid preparation due to their lower density (Suganthi & Rajan, 2017). The thermal conductivity of Co_3O_4-based nanofluids have been investigated (Singh, 2008; Ahmadi et al., 2018). It was reported that the thermal conductivity of nanofluids is greatly influenced by the particle size, particle shape, nanofluid temperature and particle concentration (Ahmadi et al., 2018). The following section goes in-depth concerning the parameters affecting the synthesis of $Co_2(OH)_3Cl$ nanoparticles, its application as well as the parameters affecting its growth mechanisms.

2.2 Cobalt hydroxychloride

The calcination (heat treatment) of solid cobalt precursors is one of the most used methods to produce Co_3O_4 nanoparticles (Nassar & Ahmed, 2011). Co_3O_4 nanoparticles have been manufactured from the calcination of different type of precursors. One of them is cobalt hydroxychloride ($Co_2(OH)_3Cl$) which is part of the cobalt layered hydroxy salts (cobalt basic salts). According to Zenmyo and Tokita (2009), $Co_2(OH)_3Cl$ has a hexagonal structure with lattice constants a = b = 6.84 Å and c = 14.5 Å as well as a rhombohedral space group R3m. Figure 2.1 shows the crystal structure of $Co_2(OH)_3Cl$ which is composed of Co^{2+} ions forming a three dimensional network of linked tetrahedrons where stacked layers of Kagome and triangular lattice planes alternate in the [001/00$\bar{1}$] directions. There exist two kinds of Co atoms in lattice with different coordination patterns (features 1 and 2 in Figure 2.1). One which is the Kagome Co^{2+} surrounded by four O atoms and two Cl atoms; the other one which is the triangular Co^{2+} surrounded by six O atoms (Zenmyo & Tokita, 2009; Jiang et al., 2019).

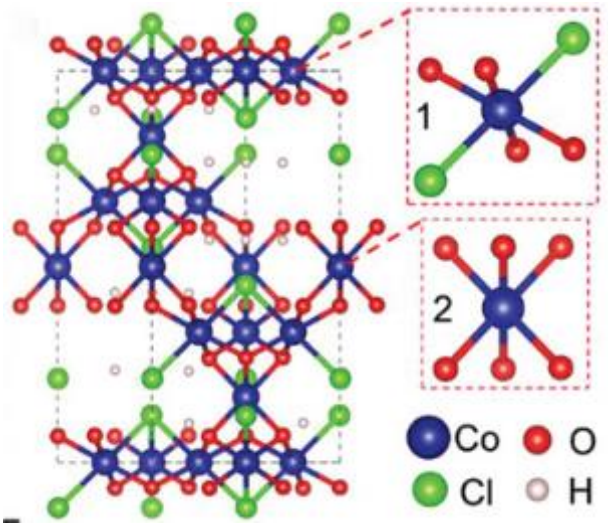

Figure 2.1: Crystal structure of $Co_2(OH)_3Cl$ with two types of Co atoms with different coordination patterns (Jiang et al., 2019)

Different polymorphs of $Co_2(OH)_3Cl$ have been reported namely, the green $Co_2(OH)_3Cl$ (Feitknecht & Fischer, 1935), the lavender-coloured β-$Co_2(OH)_3Cl$ (Feitknecht, 1935; de Wolff, 1953; Oswald & Feitknecht, 1964) and the pink β-$Co_2(OH)_3Cl$ (García-Martínez et al., 1988). According to García-Martínez et al. (1988), the green $Co_2(OH)_3Cl$ is less stable than the lavender-coloured β-$Co_2(OH)_3Cl$, hence the latter has been extensively studied (Feitknecht, 1935; de Wolff, 1953; Oswald & Feitknecht, 1964; Meng & Deng, 2017). A range of applications exist for $Co_2(OH)_3Cl$, including electrode materials for batteries, electrochemical supercapacitors, microwave absorbers and catalysts (Ma et al., 2014; Zhao et al., 2019; Wang et al., 2020; Ma et al., 2021).

2.3 Hydrothermal synthesis of $Co_2(OH)_3Cl$ particles

Various researchers have reported different methods for the synthesis of $Co_2(OH)_3Cl$ particles including, epoxide assisted precipitation, spray pyrolysis, hydrothermal synthesis, sol-gel and solvothermal synthesis (Cui et al., 2009; Park et al., 2014; Ma et al., 2017; Mansournia & Rakhshan, 2017; Jiang et al., 2019; Wang et al., 2019; Wang et al., 2022; Liang et al., 2023). Among these methods, the hydrothermal or solvothermal method offers a versatile method for regulating the particle size, particle shape, microstructure, and phase composition by altering parameters like reaction temperature, reaction time, reaction media and pH value (Tang et al., 2009). Moreover, this method is simple to use, can produce uniform products, requires low energy consumption and is less expensive than other methods, thus, this approach was used to synthesize $Co_2(OH)_3Cl$ nanostructures with unique shape and controlled particle size. Rabenau (1985) defined hydrothermal synthesis as a heterogeneous reaction taking place in an aqueous media beyond critical conditions (100 °C and 1 bar). In the case where organics are used as solvent medium, the process is referred

to as “solvothermal”. Generally, the hydrothermal synthesis occurs within a sealed reactor called autoclave, pressure vessel, or high-pressure bomb. The synthesis of $Co_2(OH)_3Cl$ particles may be accomplished by using anhydrous or hydrated cobalt (II) chloride salts coupled with hydroxyl sources in the required medium. Depending on the process, a surfactant might be added to the solution. The resulting solution is then transferred to the autoclave in which the reaction takes place at the required temperature for a certain amount of time. As the synthesis process concludes, the wet precipitates (cobalt precursor) are collected then they are washed and dried. During the $Co_2(OH)_3Cl$ particle synthesis, different reactions occur. The use of ammonium hydroxide, allows for the hydroxyl ions to be utilised as follows:

$$NH_4OH \rightarrow NH_4{}^+ + OH^- \quad \textbf{(2.1)}$$

Dissolving cobalt (II) chloride in aqueous medium:

$$CoCl_2 + 6H_2O \rightarrow [Co(H_2O)_6]^{2+} + 2Cl^- \quad \textbf{(2.2)}$$

Resulting in:

$$2[Co(H_2O)_6]^{2+} + Cl^- + 3OH^- \rightarrow Co_2(OH)_3Cl + 12H_2O \quad \textbf{(2.3)}$$

2.4 Factors affecting the size and shape of $Co_2(OH)_3Cl$ particles

Here the effects of processing conditions on the phase, size and shape of $Co_2(OH)_3Cl$ particles are discussed.

2.4.1 Effect of solvent medium

Wang et al. (2019) prepared $Co_2(OH)_3Cl$ nanoparticles via the solvothermal method. They dissolved $CoCl_2.6H_2O$ and urea ($Co(NH_2)_2$) in various solvent ratios of water/glycol to determine the effect of solvent on the formation of $Co_2(OH)_3Cl$. Then, the mixture was heated at 180 °C in an autoclave for 12 h. In a water/glycol volume ratio of 1:0, they obtained a mixture of two phases: Co_3O_4 and $Co_2(CO_3)(OH)_2$ nanowires with 2 μm in length and 60 nm in diameter. Increasing the water/glycol ratio to 1:1 resulted in a mixture of two phases: $Co_2(CO_3)(OH)_2$ and $Co_2(OH)_3Cl$ nanowires with 5.5 μm in length and 110 nm in diameter along with some scattered granular nanocubes. In 1:2, 1:3, and 1:4, only pure $Co_2(OH)_3Cl$ nanocubes were obtained. This shows that glycol facilitated the formation of $Co_2(OH)_3Cl$ nanocubes. Wang et al. (2019) suggested that the disappearance of the nanowire structure was caused by a reduction in nucleation rates and an activation of substrates due to a higher amount of glycol during the synthesis. Wang et al. (2022) synthesised $Co_2(OH)_3Cl$ particles via the hydrothermal route using a binary triethanolamine (TEOA)/water solvent and

$CoCl_2.6H_2O$ at 200 °C for 24 h. To investigate the formation of $Co_2(OH)_3Cl$, the amine was varied. Replacing TEOA with diethanolamine (DEA) resulted in the formation of a mixture of $Co_2(OH)_3Cl$ and $Co(OH)_2$. When using monoethanolamine (MEA), only $Co(OH)_2$ was produced. The amines used have the following alkaline ranking: MEA>DEA>TEOA. The weak alkaline environment provided by TEOA allows for the formation of $Co_2(OH)_3Cl$, whereas a high alkaline environment led to the formation of $Co(OH)_2$.

2.4.2 Effect of synthesis temperature

To the best of our knowledge, no study investigated the influence of temperature on the synthesis of $Co_2(OH)_3Cl$ microparticles via the hydro/solvothermal route. However, Park et al. (2014) synthesised $Co_2(OH)_3Cl$ nanoparticles via spray pyrolysis from a 0.15 M $CoCl_2$ solution under nitrogen atmosphere at different temperatures. At 500 °C, they obtained $CoCl_2(H_2O)_2$ microparticles while at 700 °C a mixture of $Co_2(OH)_3Cl$, $CoCl_2(H_2O)_2$ and CoO microparticles were produced with $Co_2(OH)_3Cl$ being the major phase product. At 900 °C, more CoO microparticles were obtained. Therefore, the suitable temperature for preparing $Co_2(OH)_3Cl$ particles via spray pyrolysis is between 500 °C and 900 °C. Park et al. (2014) did not report the impact of aging time on the size of $Co_2(OH)_3Cl$ microparticles.

2.4.3 Effect of synthesis time

Mansournia and Rakhshan (2017) prepared $Co_2(OH)_3Cl$ nanoparticles by mixing a dichlorobis(thiourea)cobalt(II) ethanolic solution (0.01 M) with ammonia solution (0.1 M) as precipitating agent. The mixture was heated in an oven at 50 °C for different times. After 1 h of synthesis, nucleation was observed. After 6 and 24 h of synthesis, the growth of $Co_2(OH)_3Cl$ nanoparticles occurred. Meng and Deng (2017) synthesised $Co_2(OH)_3Cl$ particles which were obtained from the reaction of aqueous $CoCl_2$ solution (1 M), surfactant cetyltrimethyl ammonium bromide (CTAB) and NaOH (1 M) in an eggshell reactor which was placed in an oven at 50 °C for different synthesis times. After 6 h of synthesis, they obtained $Co_2(OH)_3Cl$ nanoplates and small particles which was interpreted as the initial nucleation and growth on the surface of eggshell membrane. After 12 h of synthesis, they observed $Co_2(OH)_3Cl$ nanoplates and plate shaped aggregates. After 1 day of reaction, $Co_2(OH)_3Cl$ microparticles (0.5 to 1 µm in size) with a highly rough surface were produced. The growth of microparticles is believed to have resulted from the dissolution and recrystallisation mechanism of aggregated nanoplates. In 3 days of reaction, the size of $Co_2(OH)_3Cl$ microparticles increased and its surface became smooth. Wang et al. (2022) synthesised $Co_2(OH)_3Cl$ particles by the hydrothermal reaction of a binary TEOA/water solvent and $CoCl_2.6H_2O$ at 200 °C for different reaction times. After 1 and 3 h of reaction, some regular $Co(OH)_2$ nanosheets were produced. Further increase to 6, 12 and 24 h resulted in the transformation of $Co(OH)_2$ nanosheets into $Co_2(OH)_3Cl$ octahedrons which then self-assembled to form microspheres. It is believed that $Co_2(OH)_3Cl$ octahedrons grew via

Ostwald ripening mechanism. Therefore, controlling the reaction time is crucial for the formation of $Co_2(OH)_3Cl$.

Based on the above studies changes in synthesis conditions such as solvent medium, synthesis temperature or synthesis time can affect the formation of $Co_2(OH)_3Cl$ or result in $Co_2(OH)_3Cl$ particles of different sizes and shapes.

2.5 Basic concepts on the growth process of nanoparticles

One of the challenges encountered in the field of nanotechnology has to do with the precise control over size, size distribution and surface chemistry of nanoparticles. This control is necessary to generate nanoparticles with unique properties (Nguyen & Do, 2011). Lee et al. (2016) stated that there is a gap between the understanding of the mechanisms leading to nanoparticle formation and the necessity for synthesizing them purposefully. Therefore, it is necessary to investigate the mechanisms responsible for nanoparticle formation. According to Jolivet et al. (2000), the formation of nanoparticles from both liquid and gaseous solutions, is divided in four steps namely, the precursor formation, nucleation, growth and aging processes as illustrated in Figure 2.2 below.

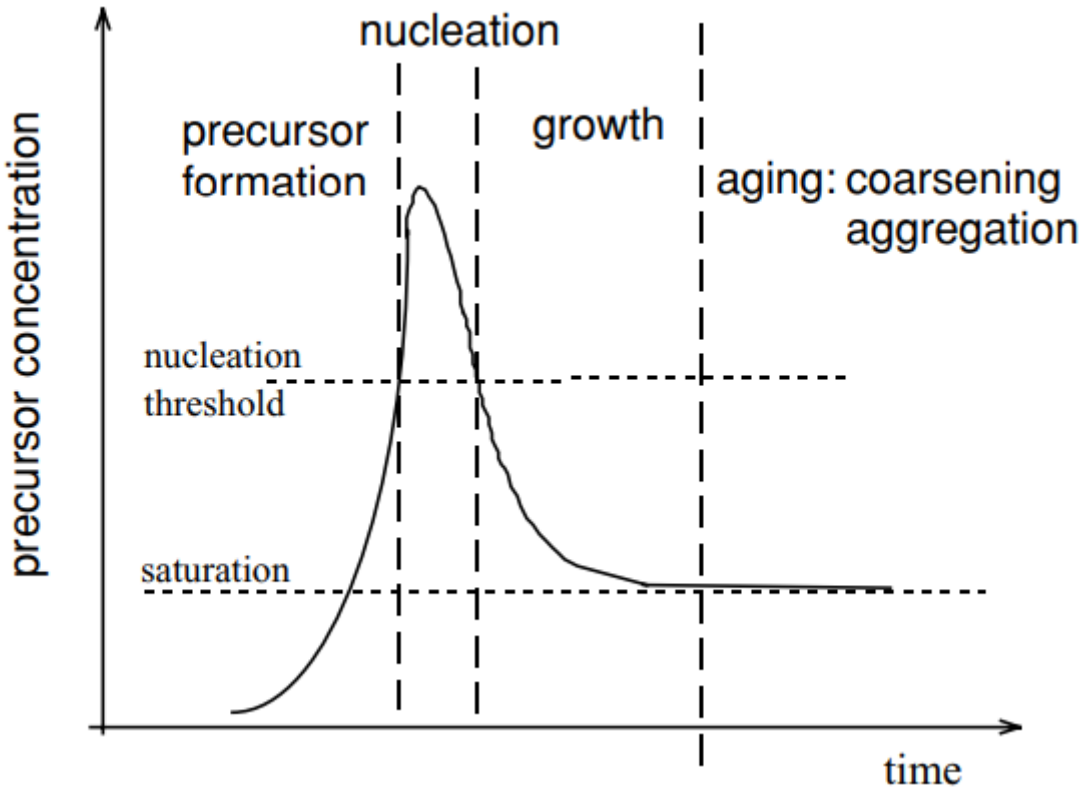

Figure 2.2: Precursor concentration against time for the formation and growth of nanoparticles (LaMer & Dinegar, 1950)

2.5.1 Precursor formation

Initially, precursor molecules are formed by hydroxylation and hydrolysis reactions to facilitate condensation (Oskam, 2006). An increase in the concentration of precursor molecules leads to a state of supersaturation as illustrated in Figure 2.2. Due to the instability of the supersaturated system, the process enters the second part of nanoparticle formation, which is the nucleation of particles.

2.5.2 Nucleation

Once the precursor concentration is above the nucleation threshold, nucleation can occur until the precursor concentration is again below that threshold (Oskam, 2006). Nucleation is defined as a process whereby an initial solid of critical size (n*) called “cluster” is formed from a chemical reaction. It is possible for the reaction to be reversible in that the cluster can dissolve back into ions as shown in Figure 2.3.

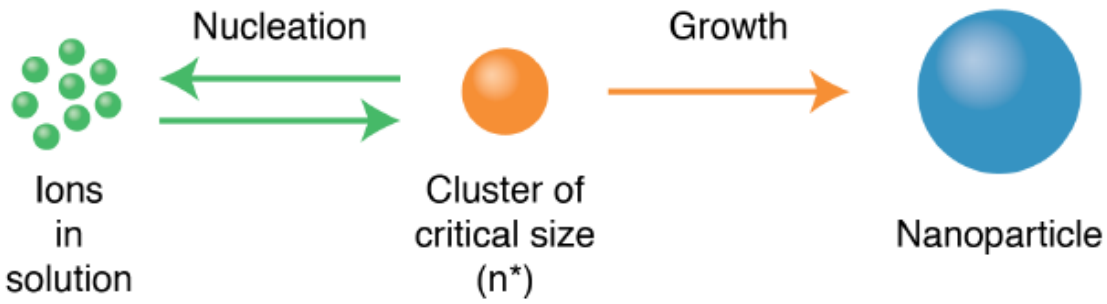

Figure 2.3: Reversible nucleation and growth of nanoparticle (Denis et al., 2015)

The process of nucleation may occur naturally or may be induced artificially (Mullin, 2001). During nucleation, the formation of a cluster from solution is because of the difference between the chemical potential of the cluster molecule (μ_c) and that of the species in solution (μ_g) as illustrated in Equation 2.4 (Kashchiev, 1982) below:

$$\Delta\mu = \mu_g - \mu_c \quad \textbf{(2.4)}$$

Where $\Delta\mu$ is the thermodynamic driving force for nucleation.

The thermodynamic driving force can also be written as:

$$\Delta\mu = k_B T \ln(S) \quad \textbf{(2.5)}$$

Where k_B, T and S are the Boltzmann constant, the temperature and the supersaturation.

In the case of insufficient supersaturation, there will be no formation of critical size cluster (Kashchiev & Van Rosmalen, 2003). If a cluster has a size larger than the critical size, it will

become stable and grow to form a nanoparticle. However, in the case where a cluster does not reach the critical size, it may dissolve (Denis et al., 2015).

2.5.3 Growth of nanoparticles

Once the precursor concentration is below the supersaturation level, the growth of nanoparticles from solution can occur. Depending on the incorporation kinetics of precursor atoms to the formed cluster turned stable nanoparticle, nanoparticle growth can either be diffusion limited or kinetic limited (Cushing et al., 2004). In case of a fast incorporation of precursor atoms to the particles, the growth will be diffusion limited. In the other case, for a slow incorporation of precursor atoms to the particles, the growth will be dependent on the rate of reaction (kinetically limited) (Cushing et al., 2004; Sugimoto, 2007). According to Jolivet et al. (2000), the growth rate for kinetically limited growth is expected to be proportional to the particle surface area. The diffusion limited growth rate is determined by diffusion to a small spherical object and is proportional to the inverse radius of the object. Hence, smaller particles grow at a faster rate (Oskam, 2006). Due to the possibility of smaller particles catching up with larger particles, diffusion-limited growth could result in a narrow particle size distribution. In general, diffusion-limited growth is expected for the synthesis of metal oxide nanoparticles (Jolivet et al., 2000).

2.5.4 Aging process of nanoparticles

The aging process is responsible for further changes in the particle size, particle shape and particle size distribution (Oskam, 2006). Nanoparticles possess high surface energy, which causes them to attract nearby precursor atoms and small clusters to their surfaces (Jolivet et al., 2000). This results in an increase in particle size whereas the number of particles decreases (Zhang et al., 2010). In this process, other mechanisms come into action: the classical Ostwald ripening (OR), coalescence and oriented attachment (OA).

- **Ostwald Ripening mechanism**

According to the terminology of the International Union of Pure and Applied Chemistry (IUPAC), the OR mechanism which is also known as “coarsening” mechanism (Figure 2.4) refers to the growth of larger particles from those of smaller size which have a higher solubility than the larger ones (Ostwald, 1897; Ostwald,1900). In a system consisting of solid particles in a liquid at chemical equilibrium. Larger particles have a lower equilibrium concentration of solute ions at their surfaces than smaller ones, which results in concentration gradients that cause the solute ions to flow from small particles to larger ones (Campbell et al., 2002). OR mechanism is driven by the decrease in the total surface free energy associated with particle-liquid interfaces (Zhang et al., 2010). There are two ways in which OR mechanism kinetics can be controlled: either by the diffusion rate of solute ions between large and small particles (Khamlich et al., 2011), or by the rates of growth (or

dissolution) at solid-liquid interfaces (Wagner, 1961). Moreover, nanoparticle growth via OR mechanism normally results in an unsymmetrical particle size distribution curve due to the systematic growth of particles (Chowdhury et al., 2014).

The Lifshitz-Slyozov-Wagner (LSW) kinetic model, which is based on the Gibbs-Thomson equation (Kirchner, 1971; Joesten & Kerrick, 1991; Huang et al., 2003), describes the OR mechanism and the general kinetic equation used in this case is:

$$D = D_0 + k(t)^{\frac{1}{n}} \quad \textbf{(2.6)}$$

Where D, D_0, t, k, n is the average particle diameter, initial average particle diameter, time, rate constant for the limiting step that is a function of temperature and exponent that is determined by the nature of coarsening mechanism, respectively.

Interface-controlled OR growth occurs if the value of n is 2, which means that the crystal growth is controlled by ions diffusing along the matrix-particle boundary. An exponent, n, value of 3 corresponds to diffusion-controlled OR growth where a volume diffusion of ions in the matrix occurs. A dissolution-controlled kinetics occurs at the particle-matrix interface if the value of n is 4 (Wagner, 1961; Huang et al., 2003; Ribeiro et al., 2005). The OR particle growth is not governed by the first order kinetics model because the exponent n can never be equal to 1 and the ratio 1/n will always be less than 1 (Tehrani et al., 2019).

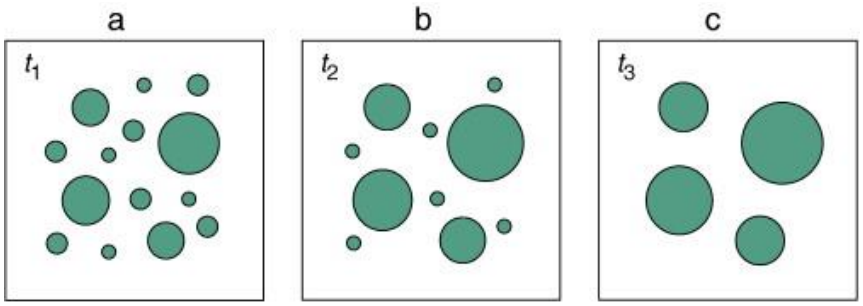

Figure 2.4: Illustration of Ostwald ripening process (Werz et al., 2014)

The only study reporting an OR-based growth of $Co_2(OH)_3Cl$ particles is that of Wang et al. (2022), where $Co_2(OH)_3Cl$ octahedrons grew via the OR mechanism. $Co_2(OH)_3Cl$ octahedrons were prepared via the hydrothermal route with a binary TEOA/water solvent and $CoCl_2.6H_2O$ at 200 °C for different reaction times. Some regular $Co(OH)_2$ nanosheets were produced after 1 h and 3 h of reaction. Extending the synthesis to 6, 12 and 24 h resulted in the production of $Co_2(OH)_3Cl$ octahedrons from $Co(OH)_2$ nanosheets. OR based growth of Co_3O_4 particles of different shapes has been reported in previous studies. For instance, Liu and Zeng (2005) synthesised asymmetrical Co_3O_4 semi-hollow nanostructures (8.7- 21.2 nm) via the hydrothermal reaction of $Co(NO_3)_2.6H_2O$, pure ethanol, ammonia solution and NaOH

aqueous solution at 100 °C for 12 and 24 h in an autoclave. After 12 h of synthesis, they obtained solid Co_3O_4 crystallite aggregates. After 24 h of synthesis, they obtained asymmetrical Co_3O_4 semi-hollow nanostructures via OR mechanism as shown in Figure 2.5. Asymmetrical semi-hollow nanostructures resulted from the evacuation of smaller Co_3O_4 crystallites (for only certain regions) that dissolved in solution to reduce the total energy of the system and then they regrew on larger crystallites (Liu & Zeng, 2005).

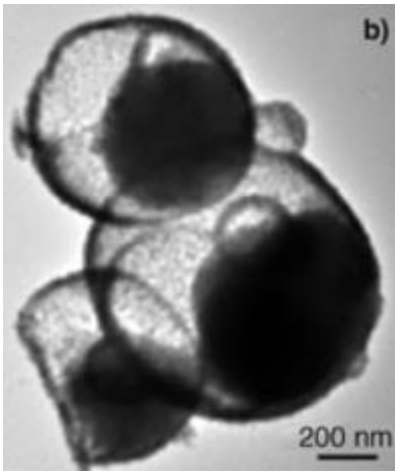

Figure 2.5: TEM image of asymmetrical Co_3O_4 semi-hollow nanostructures (Liu & Zeng, 2005)

Tian et al. (2011) obtained hollow Co_3O_4 nanocubes using the solvothermal method at 180 °C for different reaction times. They mixed cobalt (II) acetate tetrahydrate ($Co(CH_3COO)_2.4H_2O$) in a mixture of n-butanol, ammonia, and distilled water (DW). After 3 h of reaction, they obtained hexagonal flower like β-$Co(OH)_2$ particles. After 6 and 12 h, they obtained a mixture of hexagonal β-$Co(OH)_2$ nanoflakes and cubic spinel Co_3O_4 nanocubes. After 18 h, the products obtained were pure cubic spinel Co_3O_4 nanocubes with tiny hollow interiors. When the reaction was extended to 24 h, the smaller crystals located in the centre of the crystal particles dissolved continuously due to their higher thermodynamic solubility, and were relocated then evacuated, while the larger crystals did not move. This resulted in hollow Co_3O_4 nanocubes with larger cavities (nanoboxes) as shown in Figure 2.6, which were attributed to OR mechanism.

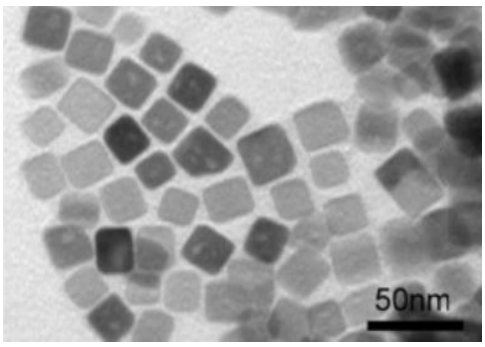

Figure 2.6: TEM image of hollow Co_3O_4 nanocubes with larger cavities (Tian et al., 2011)

Cao et al. (2014) prepared Co_3O_4 octahedra hollow particles via solvothermal synthesis at 200 °C for different synthesis times by dissolving $CoCl_2.6H_2O$ in a mixture of ethanol and deionised water (DIW) as well as a certain amount of NaOH solution. After 1.5 h of synthesis, they obtained a mixture of CoOOH (cobalt oxide hydroxide) and Co_3O_4 nanocrystals. When increasing the synthesis time to 2 h, they obtained quasi-octahedra Co_3O_4 along with some dispersed nanoparticles. After 4 h, they noticed the dissolution of the core region of quasi-octahedra Co_3O_4 which recrystallized on the outer nanocrystalline particles of the octahedron to reduce the surface energy and form regular Co_3O_4 octahedra hollow particles with an increased crystallite size. They attributed the formation of hollow nanostructures to OR process (Liu & Zeng, 2005; Tian et al., 2011). Kanie et al. (2017) synthesised Co_3O_4 nanocubes by direct hydrothermal synthesis in a highly condensed system. $Co(NO_3)_2.6H_2O$ was used as cobalt source, tetramethylammonium hydroxide (TMAH) as basic agent and nitric acid (HNO_3) for pH adjustment in an autoclave at 250 °C for 3 h. The effect of reaction time at 250 °C was investigated. After 1 h, Co_3O_4 nanocubes were slightly formed. An increment in the reaction time from 3 to 6 h resulted in an increase in particle diameter of Co_3O_4 nanocubes from 61 nm to 65 nm. According to Voorhees (1985), OR process is a co-existing particle growth mechanism, in which both synthesis temperature and time increment results in an increase in particle diameter. At 250 °C, particle size increased from 3 h to 6 h, indicating particle growth dominated by OR. However, an opposite trend was noticed in the case of reaction temperature which was increased from 225°C to 250°C, resulting in a reduction in particle size (66 to 61 nm). Therefore, OR was not the predominant growth mechanism when increasing the synthesis temperature.

OR growth kinetics has been extensively investigated, however experimentally reported particle size distribution differs somewhat from that predicted by the OR mechanism. Below are some examples:

1. Peng et al. (1998) have reported the size distribution of different colloidal semiconductor nanocrystals and under these conditions; the smaller nanocrystals

grew faster than the larger ones. Their results were clearly incompatible with the OR theory.

2. Huang et al. (2003) found that Equation 2.6 could not fit the first growth stage of hydrothermal coarsening of nano-ZnS capped with mercaptoethanol that resulted in an exponent value (n>10) with no physical meaning.
3. Several studies obtained irregular morphologies (elongated crystals, butterflies) during the synthesis of nanostructured materials (Penn & Banfield, 1999; Sampanthar & Zeng, 2002). In addition, the microstructure features of nanocrystals often incorporate defects. However, such features are rare for materials formed via OR mechanism (Dalmaschio et al., 2010; Zhang et al., 2010; Zhan et al., 2020).

- **Coalescence and oriented attachment mechanism**

Coalescence and oriented attachment are other growth mechanisms that can result in a particle size increment. In both cases, two or more particles join to form a new particle. In case of a random attachment of particles, it is called coalescence. In case of an attachment occurring in a specific direction or on a specific plane, it is called OA mechanism (Huang et al., 2003; Penn, 2004; Zhang et al., 2010). The principal driving force for OA mechanism observed in particles is linked to their tendency to decrease the surface energy between particles. According to Chowdhury et al. (2014), particle growth via OA mechanism results in wider and asymmetrical size distribution curve due to random attachment symmetry. The microscopic growth process of particles via OA mechanism is divided in two steps (Penn, 2004; Ribeiro et al., 2005). The first one is the diffusion of particles in the solution until the formation of a complex due to collision. The second one is the attachment of particles having similar crystallographic orientation followed by desorption of the surface species. In the case where two particles collide without having the same orientation, the particles will be free to rotate into different orientations, which results in a low-energy configuration, thus forming a coherent grain–grain boundary and eliminating the common grain boundary, to produce a single larger nanoparticle. In this case, the OA mechanism is also called the grain-rotation-induced grain coalescence (GRIGC) mechanism (Moldovan et al., 2002; Leite et al., 2003). The coalescence of particles is a very instable state in terms of energy, which generally lead to an adjustment of morphology known as “self-recrystallization” (Zhuang et al., 2009). The self-recrystallization of particles, as shown in Fig. 2.7 starts with state A via OA mechanism and it is not easily noticed though transmission electron microscopy (TEM) images. Then, there is a quick change from state A to state B. Because of the slow rate of self-recrystallization from state B to state C, irregular small particle attachment geometries (state B) are often captured when the sizes of the assembling units are small (Zhang et al., 2010).

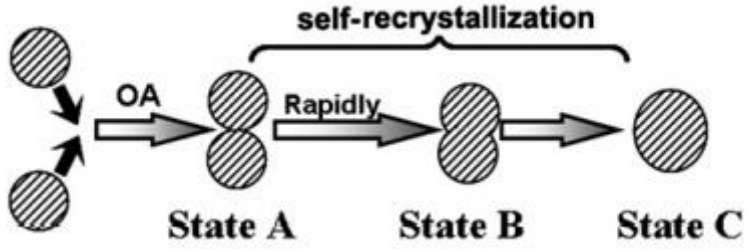

Figure 2.7: Self-recrystallization of primary particles via OA mechanism (Zhang et al., 2010)

The first model for OA growth kinetic was developed by Huang et al. (2003) as part of their efforts to explain the growth of mercaptoethanol-capped ZnS nanoparticles. In this model, the combination of two small particles into a larger particle, without either particles dissolving was assumed. Hence, the coalescence of two small nanoparticles in suspensions is as follows (Huang et al., 2003):

$$A_1 + A_1 \overset{k_1}{\rightarrow} B \qquad \textbf{(2.7)}$$

Where *B* is the product resulting from the coalescence of two particles and k_1 is the reaction kinetic constant. Hence, the OA based growth model is represented by the following equation (Huang et al., 2003):

$$D = \frac{D_0\left(\sqrt[3]{2k_1}t+1\right)}{(k_1 t+1)} \qquad \textbf{(2.8)}$$

Where D, D_0, k_1, t is the particle diameter, initial particle diameter, temperature dependent growth rate constant and time, respectively.

The only study to report an OA-based growth for $Co_2(OH)_3Cl$ particles is that of Wang et al. (2022), where hierarchical $Co_2(OH)_3Cl$ microspheres grew via OA mechanism. Microspheres of $Co_2(OH)_3Cl$ were synthesised hydrothermally using a binary TEOA/water solvent and $CoCl_2.6H_2O$ at 200 °C for different reaction times. An assembly of regular $Co(OH)_2$ nanosheets was obtained after 1 h and 3 h of reaction. Increasing the synthesis to 6, 12 and 24 h resulted in the production of self-assembled $Co_2(OH)_3Cl$ octahedrons then $Co_2(OH)_3Cl$ microspheres (Figure 2.8). A fast nucleation and crystal growth resulted in the formation of spheres while TEOA served as template for directing the self-assembly of first nanosheets then octahedrons into microspheres.

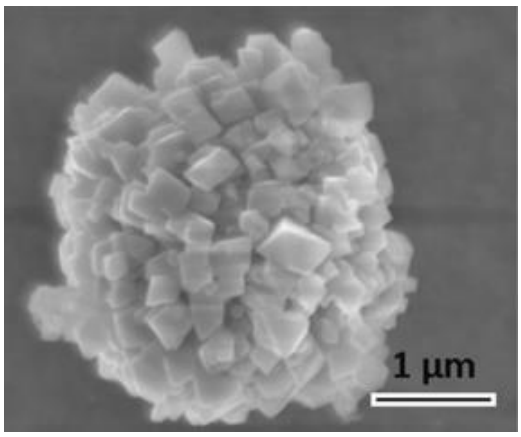

Figure 2.8: SEM image of $Co_2(OH)_3Cl$ microspheres (Wang et al., 2022)

Prior studies reported an OA based growth for Co_3O_4 particles of different shapes. He et al. (2004a) synthesised spherical mesoporous Co_3O_4 nanoparticles (with 2 nm wormlike pores) from the OA of primary Co_3O_4 nanocrystals (5-20 nm in size) as shown in Figure 2.9.

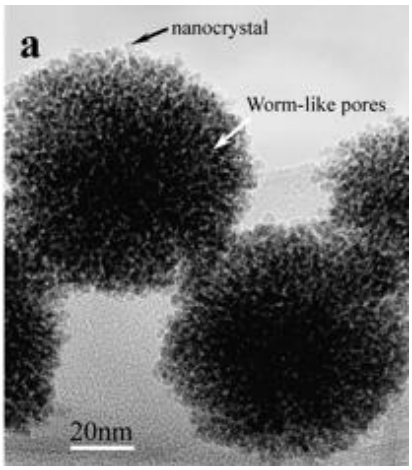

Figure 2.9: OA of primary Co_3O_4 nanocrystals (He et al., 2004a)

Initially, the intermediate product ($Co(NO_3)_2.7C_6H_{13}OH$) was obtained from the reaction of n-hexanol and $Co(NO_3)_2.6H_2O$. Monodispersed Co_3O_4 nanocrystals of 5-20 nm in size were produced from the thermal decomposition of $Co(NO_3)_2.7C_6H_{13}OH$ in the presence of n-octanol. Controlled addition of water to $Co(NO_3)_2.7C_6H_{13}OH$ in the presence of n-octanol resulted in the OA of Co_3O_4 nanocrystals forming spherical mesoporous nanoparticles. As the water content increased, so did the particle size of Co_3O_4 aggregates. When the molar ratio of water to ($Co(NO_3)_2.7C_6H_{13}OH$) was 1.5, some aggregates of 40 nm in size were yielded. When the ratio was increased up to 5 and 12, the aggregate particle size increased to 90 and 200 nm, respectively. Growth of aggregated particles occurred due to the conversion of water into surface hydroxyls that acted as binders between the primary particles (He et al., 2004a). However, when the water amount was reduced, the smaller

surface hydroxyl density on the nanoparticle surface resulted in the formation of smaller monodispersed particles. He et al. (2004a) also reported that an increase in synthesis temperature and time led to an increase in particle size and a broadening of particle size distribution. He et al. (2004b) produced hollow Co_3O_4 nanospheres via the solvothermal synthesis using $Co(NO_3)_2.6H_2O$, water, absolute methanol and sodium dodecyl benzenesulfonate (SDBS) as surfactant. The solvothermal process was performed at 180 °C for 1 h, which yielded spherical $Co(OH)_2$ –NO_3 particles of ~ 400 nm in size. When the synthesis time was increased to 4h, there was a formation of 200 nm Co_3O_4 hollow nanospheres. The presence of "dimples" and "creases," as well as nanocrystals in the hollow nanospheres, indicated that the walls were constructed by aggregated Co_3O_4 nanocrystals (Figure 2.10).

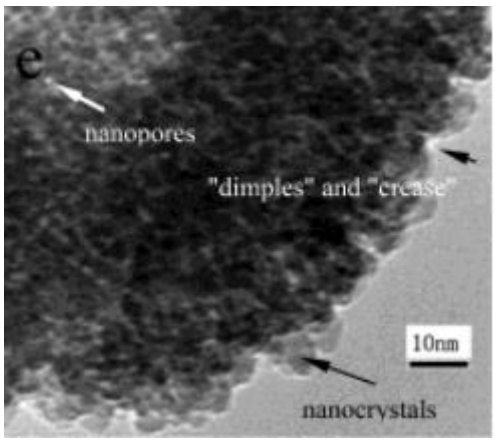

Figure 2.10: Dimples and creases in hollow nanospheres (He et al., 2004b)

Ganguli et al. (2019) synthesised pure Co_3O_4 nanocubes using $CoCl_2.6H_2O$ in water-ethylamine mixture and ethylamine in water-ethanol mixture, respectively. The synthesis was conducted at 120 °C for different synthesis times via the solvothermal method. In the case of water-ethylamine mixture, large β-$Co(OH)_2$ sheets along with a small amount of Co_3O_4 nanocubes were obtained after 30 minutes (min). The majority of β-$Co(OH)_2$ sheets had converted into larger Co_3O_4 nanocubes and small aggregated nanocubes after 90 min. The small aggregated nanocubes resulted from the progressive OA of particles as their identical planes perfectly coalesced at their intersection. When extending the synthesis to 360 min, larger Co_3O_4 nanocubes were produced. In the case of ethylamine in an equal water-ethanol ratio, an imperfect attachment of nanocubic Co_3O_4 particles along with multiple cracks was reported. Fuchigami et al. (2020) obtained a raspberry like structure of Co_3O_4 nanoparticles using cobalt glycolate, ethylene glycol (EG), water and sodium sulphate solution via the hydrothermal route. The synthesis occurred at 180 °C from 0.5 to 24 h. After 0.5 h, they observed the self-accumulation of Co_3O_4 particles in the form of raspberry via OA mechanism along with dispersed particles (10-20 nm). When increasing the synthesis to 1 h,

the raspberry structure of nanoparticles was retained, and they were integrated into a larger secondary particle still via OA mechanism. After 6 and 12.5 h, particles were said to have grown by a dissolution-precipitation process due to the presence of small gaps among primary particles. After 24 h, primary particles grew further then split leading to the decomposition of raspberry like structure and their crystallographic orientation. In addition, Fuchigami et al. (2020) reported an increase in the size of primary particles on the outer surface from 6.8 to 11.2 nm, whereas the size of raspberry shaped particles remained unchanged (~100 nm) from 1 to 12.5 h.

It has been reported that both OR and OA based growth of $Co_2(OH)_3Cl$ particles is influenced by an increase in synthesis time resulting in larger particles. The OA based growth of $Co_2(OH)_3Cl$ particles is also affected by the type of solvent used during synthesis. It was shown in the study of Heuvel et al. (2021) that synthesizing Co_3O_4 nanoparticles in solvents at 50% and 100% propanol concentration via solvothermal synthesis can result in a decrease in particle size from ~34 nm to ~67 nm. There is however no study examining the growth mechanism of $Co_2(OH)_3Cl$ particles using propanol as a solvent, to our knowledge. Therefore, the microscopic structures of $Co_2(OH)_3Cl$ particles grown in propanol will be observed then, the corresponding growth kinetic models will be proposed to explain the particle growth mechanisms identified from the microscopic structures.

The following section reviews previous experimental studies on the preparation and properties of Co_3O_4 nanofluids. Considering that no study has previously dispersed $Co_2(OH)_3Cl$ nanoparticles in any solar heat transfer fluid, the following review will serve as a guide for the preparation and measurement of some properties of $Co_2(OH)_3Cl$ nanofluids

2.6 Application of Co_3O_4 nanoparticles in solar thermal heat transfer fluids

2.6.1 Introduction

In flat-plate solar thermal collectors (STCs) , solar irradiation passes through a transparent cover then it hits the absorber plate. The heated plate transfers heat via conduction. In contrast, heat transfer via convection occurs in the working fluid. Researchers have investigated different techniques to develop efficient flat plate STCs with a high thermal efficiency. The techniques include modifying the geometry of the absorber tube and/or collector, using nanofluids, coating the absorber with solar selective coatings, using heat pipes, and mini/macro channels in the collector (Khamlich et al., 2012; Khamlich et al., 2013; Alam et al., 2021). This issue can be minimized by allowing the direct absorption of solar irradiation by the working fluid without heating any other structures within the receiver . In flat plate STCs, heat is extracted from the plate by means of heat transferring fluids possessing desirable heat transfer characteristics (Alam et al., 2021). However, conventional

fluids such as DIW, EG, polyethylene glycol (PEG), therminol VP-1 used in STC have been reported to be transparent to solar radiant energy (Drotning, 1978; Otanicar et al., 2009).

As a result of that, additives are needed to enhance the optical properties of conventional fluids. Although, micron sized particles have the ability of enhancing the thermal and optical properties of heat transfer fluids, they are denser than nanosized particles leading them to settle out of suspension, causing sedimentation and eventually clogging problems in microchannels (Dharmalingam et al., 2014; Ilyas et al., 2014). The settling out of particles occurs because of the competing forces (Brownian motion and gravitational force) occurring between particles in a suspension, which is discussed in detail in section 2.7. In recent years, nanofluids have gained popularity due to their superior properties (high surface to volume ratio, high thermal conductivity etc.) in comparison with those of the base fluids (Sani et al., 2011). Furthermore, an enhanced stability coupled with high solar energy absorption capability make nanofluids suitable for solar energy absorption in solar thermal systems (Tyagi et al., 2009; Khullar et al., 2012; Lenert & Wang, 2012).

2.6.2 Impact of Co_3O_4 optical band gap for solar energy absorption

Nanosized semiconductors such as Co_3O_4 exhibit properties between molecules and bulk solid materials (Ghobadi, 2013). The energy bandgap which is known as the states nearby the valence and conduction bands of semiconductor materials is useful for determining the semiconductor abilities for future device applications (Zanatta, 2019). The light emitted from the sun is a form of electromagnetic radiation energy. The sun gives off gamma rays, X-rays, ultraviolet, visible light, infrared, microwaves and radio waves radiations. However, sunlight reaches the Earth mainly through visible and near-infrared radiations (Liu et al., 2018). Hence, a semiconductor with the capability of absorption in the visible and near-infrared region of the solar spectrum would be ideal for applications in STC systems. Semiconductors with wide band gaps such as titanium dioxide (TiO_2) or ZnO are restricted to absorption in the ultraviolet region of solar spectrum (Gondal et al., 2015; Ravi Dhas et al., 2015; Zhang et al., 2019). Co_3O_4 has been reported to have a narrow band gap of 2.1-1.2 eV (Li et al., 2021; Serrano de la Rosa et al., 2021). The reported band gap range for Co_3O_4 is equivalent to wavelength values ranging from approximately 590 to 1033 nm. According to Zwinkels (2015), the visible to near-infrared region of the electromagnetic spectrum corresponds to wavelength values ranging from ~400 to 2500 nm therefore, Co_3O_4 can absorb solar radiation in this region.

2.6.3 Types of nanofluids

According to Chamsa-ard et al. (2017), several studies was conducted on nanofluids, which included different types of nanoparticles such as pure metals (Au, Ag, Cu, Al, and Fe), metal oxides (Al_2O_3, CuO, Fe_3O_4, SiO_2, TiO_2 and ZnO), a variety of carbon materials (diamond,

graphite, single/multi wall carbon nanotubes) and carbides (SiC, TiC). Because of the cost of noble metals, researchers have turned to metal oxide nanoparticles (Al_2O_3, CuO, Fe_3O_4, SiO_2, TiO_2, etc.) for nanofluid preparation. Nanoparticles of these types have been dispersed in fluids such as water, EG, water/EG mixtures and oils (thermal oil, silicon oil etc.)(Li et al., 2010; Teng et al., 2010; Nallusamy, 2015; Kamila & Venugopal, 2019). Prior to discussing the properties of Co_3O_4 nanofluids, it is essential to understand the techniques used for their preparation.

2.6.4 Preparation methods for nanofluids

A nanofluid is obtained through the dispersion of powdered nanoparticles within a conventional fluid. Two techniques are used to prepare nanofluids (Devendiran & Amirtham, 2016):

- **One-step technique**

This technique refers to the simultaneous production and dispersion of nanoparticles in the base fluid in a single step. Different one-step techniques exist such as the one-step direct evaporation method (Akoh et al., 1978) that is similar to vacuum evaporation onto a running oil substrate (VEROS). One of the common one-step methods is “vapour deposition” which consists in producing nanofluids when gaseous nanoparticles solidify when in contact with the base liquid film (Ali et al., 2018b). Another example of the one-step technique is the laser ablation method used to prepare alumina-DIW, Cu-DIW and Cu-EG based nanofluids (Piriyawong et al., 2012; Khamliche et al., 2021; Aligholami et al., 2023; Khamlich et al., 2023).The major problem of the one-step technique is that only low vapour pressure fluids are compatible with it.

- **Two-step technique**

This technique consists in first producing nanoparticles via various routes (biological, chemical or physical) then dispersing them in the required base fluid. Nowadays, various chemical companies sell different nanopowders, which have made this method widely applicable on an industrial scale. However, stability is a big concern for this technique because nanoparticles easily aggregate due to strong van der Walls attractive forces between them. Regardless of such disadvantages, this technique is known as the most economic technique for the production of nanofluids (Mukherjee & Paria, 2013). Several studies reported the preparation of various metallic, non-metallic, and hybrid-based nanofluids using the two-step technique (Su et al., 2011; Hajian et al., 2012; Zafarani-Moattar & Majdan-Cegincara, 2012; Esmaeilzadeh et al., 2013).

2.7 Stability of nanofluids

2.7.1 Introduction

Stability poses a key challenge in nanofluid preparation due to its direct influence on the thermophysical properties of these fluids. Particles suspended in a fluid are subjected to three types of interactions namely molecular forces, electrical forces, and magnetic forces (Pietsch, 2004:7-23). Molecular forces comprise Van der Waals attractive forces, valence forces (or free chemical bonds) and non-valence forces (or hydrogen bonding). Particles can interact via electrical forces due to various factors such as electrical double layer repulsive forces, electrostatic forces or excess charge found on the particle surface (Pietsch, 2004:7-23; Ilyas et al., 2017). According to the classical Derjaguin, Landau, Verwey, and Overbeek (DLVO) theory (Verwey et al., 1948), when particles are dispersed in a fluid, the total interaction potential of particles is associated to Van der Waals attractive potential and electrical double layer repulsive potential. Particles in suspension are characterized by the Brownian motion of particles resulting from the collision between particles and surrounding fluid molecules (Mitchell & Kogure, 2006). A nanofluid is stable when the repulsive forces are large enough to overcome the attraction forces between particles resulting from the collision process. If the repulsive forces are not large enough, nanoparticles dispersed in the base fluid will adhere to one another, form agglomerates then settle out of suspension under the effect of gravity (Ali et al., 2018). According to McNaught and Wilkinson (2014), an agglomerate occurs when dispersed particles are held together by weak physical interactions, eventually resulting in sediments larger than the colloidal size (1 nm to 1 μm). The whole process is reversible. Aside from agglomeration, aggregation can also occur among dispersed particles in a fluid, namely when strong physical interactions hold dispersed particles together (McNaught & Wilkinson, 2014). Aggregation can result in cluster formation and is irreversible. Techniques used to obtain and/or maintain stable nanofluids are discussed in the next section followed by the inspection methods used to determine the stability of nanoparticles dispersed in heat transfer fluids via the two-step method in sections 2.7.2. and 2.7.3., respectively.

2.7.2 Stabilisation techniques for nanofluids

Stability of nanofluids is an important parameter because it plays a major role in not only the lifespan of nanofluids but also in conserving their thermophysical properties. Stability of nanofluids can be improved by the physical or chemical techniques listed below (Matusiak & Grządka, 2017):

- **Addition of surfactants**: This chemical technique is simple and economic. Surfactants are amphiphilic compounds containing hydrophobic groups (tail portion) and hydrophilic groups (polar head portion). The presence of the hydrophilic group is

responsible for increasing the hydrophilic behaviour between the dispersing medium and the nanoparticles (Ali et al., 2018a). Surfactants are used to lower the surface tension of the dispersing medium hence, improving the immersion of nanoparticles. According to Yu and Xie, (2012), surfactants are classified in four classes based on the head group composition as shown in Table 2.1 below:

Table 2.1: Classification of surfactants (Yu & Xie, 2012)

Surfactant class	Head group characteristics & classes	Examples
Cationic	Positively charged (long-chain quaternary ammonium compounds and long-chain amines).	e.g., dodecyl trimethyl ammonium chloride, CTAB.
Anionic	Negatively charged (carboxylates, sulphates, sulphonates, phosphates and others).	e.g., oleic acid (OA), sodium dodecyl sulphate (SDS) or sodium lauryl sulphate (SLS).
Non-ionic	Neutrally charged (alcohol ethoxylates, sorbitan ester ethoxylates, glucosides).	e.g., alcohols, triton X-100, decyl glucoside, polyethylene oxide, spans.
Amphoteric (and zwitterionic)	Positively and negatively charged (N-alkyl betaines, N-alkyl amino propionates).	e.g., dodecyl betaine, lauryl amido propyl dimethyl betaine.

The selection of a suitable surfactant for nanofluid stabilization is dependent on the base fluid to be used in the preparation of nanofluids. If the base fluid is a polar solvent, then a water-soluble surfactant is required; otherwise, an oil-soluble should be used instead (Yu & Xie, 2012). One of the disadvantages of using surfactant as a way of enhancing the stability of nanofluids is its sensitivity to hot temperature. When temperature rises, this causes the bonds between nanoparticles and the surfactant to be damaged and it results in the apparition of foams (Yu & Xie, 2012). Furthermore, excessive amounts of surfactants will alter the properties of nanofluid by increasing its viscosity and reducing its thermal conductivity (Mingzheng et al., 2012; Yu & Xie, 2012; Kong et al., 2017).

- **Surface modification technique**: is known as the surfactant free method, which consists in injecting functional nanoparticles in the dispersing medium to obtain stable nanofluids. Several examples on surface modification techniques have been reported. For instance, Chen and Xie (2010) improved the stability of carbon nanotubes (CNT) by introducing hydroxyl groups onto the surface of CNT. Yang and Liu (2011) maintained the dispersion of SiO_2/DIW nanofluids (30 nm in size and 10 wt%) for 12 months by functionalizing the nanoparticles with silanes of (3-glycidoxylpropyl) trimethoxysilane. Additional details regarding the surface modification techniques can be found in the study by Yu & Xie (2012).
- **Ultrasonic agitation**: is a homogenisation technique where above 20 kHz of ultrasonic rates/frequencies are used to agitate the agglomerated nanoparticles in the dispersing medium (Noroozi et al., 2014; Mahbubul et al., 2016). The instrument used

for this technique is called a sonicator, which aims to disperse nanoparticles in the base fluid while decreasing the nanoparticles size in the fluid (Zhang et al., 2008). There are two types of sonicators namely, bath-type and probe-type (Figure 2.11).

Figure 2.11: Probe-type and bath-type sonicators (Ali et al., 2018a)

Due to their high intensity, probe-type sonicators are more effective than the bath-type (Green & Hersam, 2010; Son et al., 2020). Petzold et al. (2009) investigated the distribution of fumed silica (aerosol) particles (7–40 nm in size) dispersed in water. Particles dispersion, within the base fluid, was performed using a magnetic stirrer, high intensity ultrasonic probe, and an ultraturrax, each for 10 min. Zeta potential analysis results have shown that, unlike the samples stabilized using the magnetic stirrer and ultraturrax, those prepared using the ultrasonic probe displayed a uniform particle dispersion. Among the disadvantages of ultrasonic agitation are the unknown optimum sonication time, wave, and pulse mode. Moreover, increasing the sonication time does not necessarily improve particle reduction. On the contrary, it may cause the particle size to increase (Kole & Dey, 2012).

- **pH control of nanofluids**: This chemical technique consists in adjusting the pH value of nanofluids hence, changing the surface charge of nanoparticles (Choudhary et al., 2017). It is known that the stability of nanofluids is dependent on their electro-kinetic properties therefore, this technique can improve their stability (Mukherjee & Paria, 2013). The pH value of a nanofluid can be increased or decreased via the addition of an appropriate nonreactive alkaline or acidic solution, respectively (Azizian et al., 2016). Numerous studies have been conducted on the effect of pH on the stability of nanofluids. For instance, Witharana et al. (2012) investigated the stability behaviour

of alumina (Al_2O_3)/H_2O nanofluids (0.5 wt% & 46 nm particle weight concentration and particle size, respectively) initially at pH 4.7. According to Gulicovski et al. (2008), the isoelectric point (IEP or pH_{IEP}) is the pH at which a molecule or surface of a dispersed solid has no zeta potential (no net charge). In the study of Witharana et al. (2012), the IEP was equal to 8.9. Using dilute NaOH solution, they found that the suspensions were stable at a pH value of 6.3 for more than 30 min compared with the pH value of 7.8 that displayed a complete particle separation and settlement after 30 min. A similar study was conducted by Vickers et al. (2009) regarding the stability of Co_3O_4-DIW nanofluids. Using 0.1 M HCl or NaOH solution, they adjusted the pH of Co_3O_4 nanofluids to pH values ranging from 2 to 12. They reported the zeta potential of Co_3O_4 nanofluids as function of different pH values. The IEP of particles was equal to 8. In a neutral medium, they noted that the zeta potential was +8.7 mV. In acidic media (~pH 2-2.5), the zeta potential was large and positive (~ +30 mV) whereas in basic media (~pH 10-11.5), the zeta potential was large and negative (~ -38 mV).

Leong et al. (2017) investigated the stability of TiO_2-water nanofluids by varying their pH values using acetic acid and ammonia hydroxide solutions. They found that the most stable suspension was at pH 5 (+38.9 mV) followed by the suspension at pH 3 (+14.5 mV) and that at pH 9 (+0.0182 mV).

2.7.3 Stability inspection techniques for nanofluids

This section contains detailed information on different techniques used to determine the stability of nanofluids:

- **Zeta potential analysis**: evaluates the quality of nanofluids stability through the observation of their electrophoretic behaviour (Ghadimi et al., 2011). In aqueous systems, most solid particle surfaces acquire charges which are balanced by oppositely counterions in solution forming an adsorbed double layer called electrochemical double layer (Předota et al., 2016). That layer comprises the stern layer and diffuse layer which are illustrated in Figure 2.12. Oppositely charged ions of the fluid get attracted to the negatively charged particle surface, hence forming the inner region (stern layer) where ions are firmly associated. The outer region is known as “diffuse layer” where same and oppositely charged ions are loosely bound. According to Kaszuba et al. (2010), the potential at the slip plane (shear plane) of a suspended particle moving under electric field is known as zeta potential (ζ). In other words, the zeta potential measures the degree of repulsion between similarly charged particles in dispersion by using an instrument called zeta sizer nano. Zeta potential is expressed in millivolts (mV) (Chang et al., 2007).

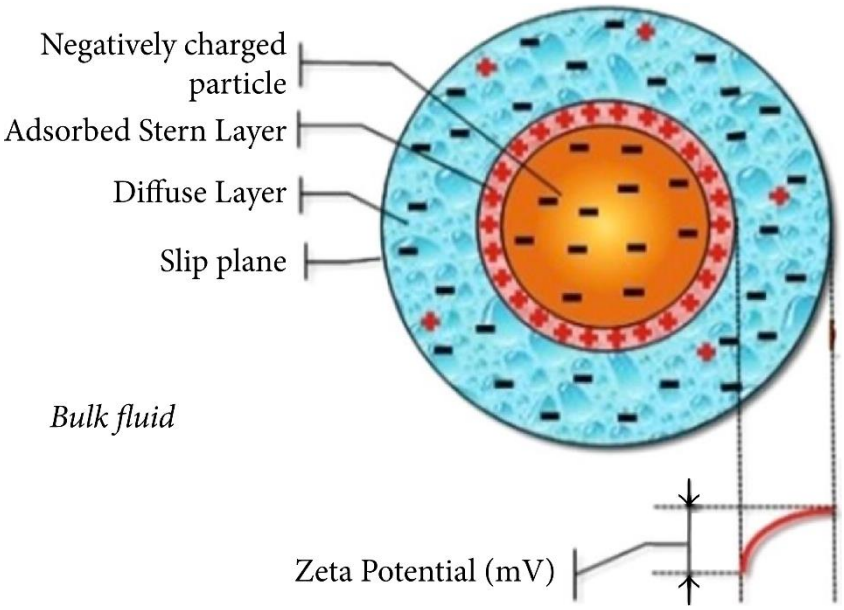

Figure 2.12: Zeta potential of nanoparticle dispersed in a fluid (Mukherjee & Paria, 2013)

If particles suspended in the fluid have a high zeta potential value (both positive and negative) this implies a higher repulsive force between them. Therefore, particles will not tend to come closer (Setia et al., 2013). As shown in Figure 2.13, a nanofluid with a zeta potential > ± 60 mV shows excellent stability and that with a zeta potential equal to ± (40 to 60) mV has a good stability. For a zeta potential that is equal to ± (30 to 40) mV, the nanofluid is relatively stable, and if the zeta potential is < ± 30 mV, the nanofluid undergo significant aggregation (Setia et al., 2013).

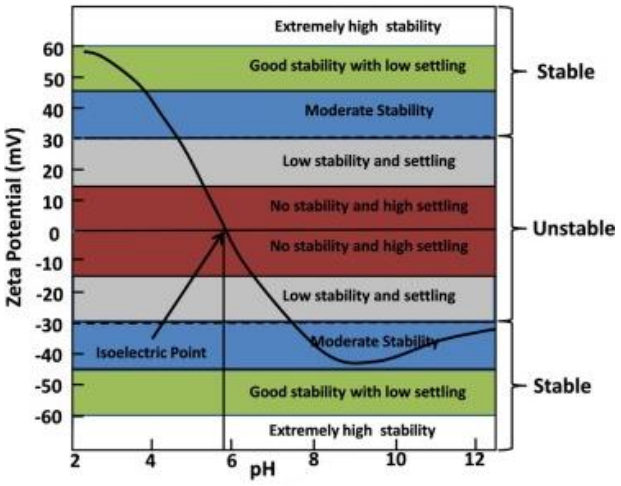

Figure 2.13: Zeta potential diagram against pH values (Chakraborty & Panigrahi, 2020)

- **Sedimentation photograph capturing technique:** is one of the simplest techniques for inspecting the stability of nanofluids (Wei & Wang, 2010). Sedimentation occurs when nanoparticles settle out of the base fluid and finally reach a resting point against

an external force. According to Wei et al. (2009) to observe the sedimentation process, a sample of the nanofluid is placed in a transparent glass vial; successive photographs of the vial are taken at equal intervals of time to observe the formation of sediments. A comparison of the captured images is then performed to assess the stability of the nanofluid. According to Ilyas et al. (2013), an unstable nanofluid can display three different behaviours of sedimentation namely: (1) dispersed sedimentation where the sediment height is gradually increasing as the solution clarifies, (2) flocculated sedimentation where the sediment height reduces as the solution becomes clear and (3) mixed sedimentation when previous phenomena occur simultaneously, as shown in Figure 2.14.

The characterised nanofluid is considered stable when the size of the nanoparticles and their dispersion remain constant over time (no sedimentation occurs) (Ilyas et al., 2013). Many researchers have confirmed that the stability of nanofluids can be indicated using the sedimentation method (Xian-Ju & Xin-Fang, 2009; Witharana et al., 2012; Ilyas et al., 2013). Though this method offers a high-performance analysis of nanofluid stability at a low cost, very few papers have been published on this subject (Lemes et al., 2017).

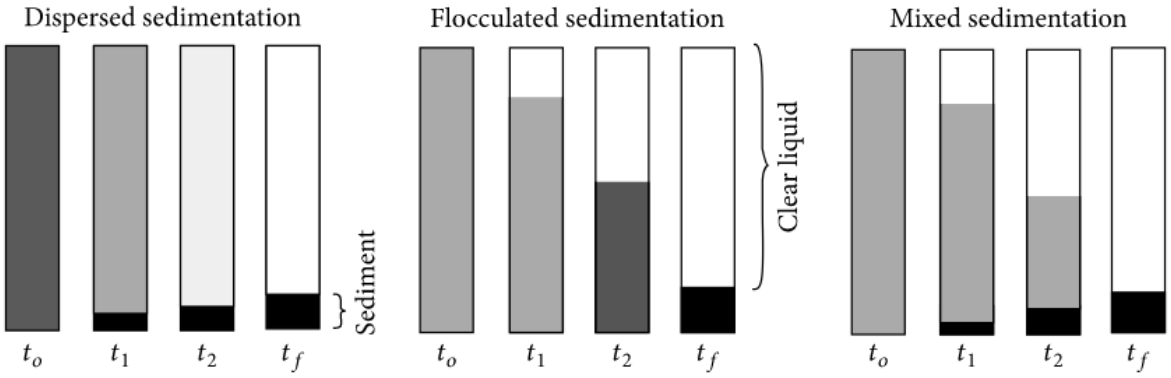

Figure 2.14: Different sedimentations in nanofluids (Ilyas et al., 2013)

The fact that this method requires a long observation period, which can be very time consuming, maybe an explanation for the slow adaption of such stability inspection technique (Mukherjee & Paria, 2013).

- **Centrifugation technique:** is preferred over sedimentation photograph capturing technique because results can be obtained quickly. Using a dispersion analyser centrifuge, this technique involves the visual examination of the nanofluid sedimentation. The results of Singh and Raykar (2008) showed that silver/ethanol nanofluids of 30–60 nm particle size and 0.0112–0.0114 vol% were stable (with no

sign of sedimentation) with the addition of polyvinylpyrrolidone surfactant and centrifugation for 10 h at 3000 rpm.

- **Spectral analysis technique:** was first introduced by Jiang et al. (2003) and can only be implemented if the dispersed nanoparticles absorb light between 190 and 1100 nm (Yu & Xie, 2012). This technique consists in monitoring the nanofluid stability by checking the absorption peak characteristics using an ultraviolet-visible (UV-VIS) spectrophotometer and their change over time. A transmittance measurement can also be applied to monitor the nanofluid stability. A reduction in absorbance over time indicates nanofluid instability, whereas an increase in transmittance over time indicates nanofluid instability. There is a linear relationship between absorbance and concentration of nanoparticles in suspension, but an inverse relationship between transmittance and concentration (Hwang et al., 2007; Jana et al., 2007). Jiang et al. (2003) prepared 0.5 wt% CNT-H_2O nanofluids with the addition of 2.0 wt% SDS as surfactant. Using UV-VIS spectroscopy, they found that CNT/SDS nanofluids exhibited extreme stability, with the CNT concentration decreasing only by 15% compared with 50% decrease for the bare CNT nanofluids. Sedimentation of nanoparticles reduced their concentration over time, resulting in a decrease in absorbance. However, this method is not applicable to nanofluids containing dark coloured nanoparticles and high particle concentrations (Ghadimi et al., 2011).
- **3ω-technique:** is used to evaluate the thermal conductivity change of nanofluids due to nanoparticle sedimentation. The study of Oh et al. (2008) focused on examining the stability of Al_2O_3/DIW and Al_2O_3/EG nanofluids, with 1-4 vol% and nanoparticles of 45 nm in size. The effective thermal conductivities of nanofluids were found to increase in value with time (up to 1 h). This enhancement was attributed to the clustering of nanoparticles in the base fluids where heat transfer occurred via conduction. However, thermal conductivity declines beyond an optimum value of particle clustering upon further agglomeration (Prasher et al., 2006a).
- **Electron microscopy techniques:** encompass a variety of techniques such as HR-TEM and HR-SEM, these methods are employed to explore the morphology, size, and particle size distribution of nanoparticles. These analyses prove beneficial in determining and evaluating the stability of nanofluids. If clusters of nanoparticles are spotted within the images, it is likely that the nanofluid will sediment (i.e., the nanofluid is unstable). SEM and TEM techniques have been used by Nallusamy (2015) to determine the stability of CuO nanoparticles in the base fluid. The SEM analysis revealed that the CuO nanoparticles were spherical in shape and uniformly scattered. The TEM analysis confirmed the homogeneity of the formed nanoparticles, without significant phase separation or coatings on the surface.

2.7.4 Preparation of Co_3O_4 nanofluids

Table 2.2 below summarizes the details of Co_3O_4 nanofluids preparation via the two-step method. In general, Co_3O_4 nanoparticles used for the preparation of nanofluids were either purchased from companies manufacturing nanopowders or synthesised via various routes. The majority of researchers only used commercially available Co_3O_4 nanopowders for nanofluid preparation. The rest of researchers utilized Co_3O_4 nanopowders produced via different methods (Vickers et al., 2009; Gupta et al., 2021; Rahman Salari et al., 2022). Only Mitra et al. (2021) utilized both commercially available Co_3O_4 nanopowders as well as those synthesised via the hydrothermal route for preparing nanofluids. The size of Co_3O_4 nanoparticles varied from one study to the other. Different particle shapes such as cubic, spherical, oblate, octahedron, rods and flowers were used. The choice of the base fluid for nanofluid preparation depends on the nanofluid application. It can be noted that DIW has been the most used base fluid for the preparation of Co_3O_4 nanofluids. This is due to water having a higher thermal conductivity (Choi & Eastman, 1995), specific heat capacity and low viscosity (Fanney & Klein, 1988). Hence, the utilisation of water-based nanofluids in low temperature solar collectors up to 90 °C (Rubbi et al., 2021). Other fluids have also been used: EG, PEG, paraffin, therminol 55 and neat diesel in the preparation of Co_3O_4 nanofluids. EG is the most common heat transfer fluid from the glycol family used in the solar thermal harvesting industry because of its good thermal and physical properties. However, it is relatively toxic, and degrades much faster at temperatures encountered in some solar thermal systems (Patil, 1975; San Martin & Fjeld, 1975; Vargas et al., 2009). PEG is a thermally stable fluid, non-toxic and non-corrosive. However, it has a lower thermal conductivity (Prasad et al., 2019). Oil-based nanofluids are well suited for medium-high temperature (100-350 °C) thermal energy application due to their high boiling point and exceptional thermophysical properties at higher temperatures (Rubbi et al., 2021).

Co_3O_4 particle concentration was reported using various metrics, either weight percent (wt%) or volume percent (vol%). Various methods have been used to maintain and determine the stability of Co_3O_4 nanofluids. Vickers et al. (2009) synthesised Co_3O_4 nanocubes using the one-step approach as done in the study by Feng and Zeng (2003) to disperse them in PEG. In order to determine the stability of Co_3O_4 nanoparticles dispersed in PEG, they performed a TEM analysis that showed that the particles were at most 65 nm in size, which is below the critical size of the particle in suspension ($d < 550$ nm). They did not observe any sedimentation during their study. Fazlali et al. (2012) prepared Co_3O_4 ferrofluids by dispersing Co_3O_4 nanoparticles and oleic acid (surfactant) in liquid paraffin. The suspensions were mixed in a ball mill at 150 rpm for 1 h. Then, they were sonicated in an ultrasonic bath (50-60 Hz) for 1 h to obtain a better distribution of nanoparticles and allow better covering of particles by OA. They noted that the nanofluids were stable during the tests. Hosseini et al.

(2012) followed the same procedure for preparing Co_3O_4 ferrofluids. However, they mixed them in a planetary mill for 5 h instead of 1 h (Fazlali et al., 2012). Then, the suspensions were sonicated for 10 min in an ultrasonic bath (5060 Hz). Mariano et al. (2015) dispersed Co_3O_4 nanoparticles in EG by using an ultrasonic homogeniser probe. To determine the stability of Co_3O_4-EG nanofluid (0.01 wt%), they used a UV-Vis spectrometer. The results revealed that the sample could absorb light at two wavelength values close to the maxima, λ = 205 nm, and λ = 410 nm. They also noticed that in each case; the absorbance decrease was lower than 1% in 24 h, so the sample was considered stable during the experimentation period. Katiyar et al. (2016) dispersed Co_3O_4 nanoparticles in EG and therminol oil, respectively. The dispersions were subjected to mechanical stirring for 20 min then; they were sonicated for 2 to 3 h using a probe type sonicator (65% amplitude and 10:10 pulse rate). To improve the stability of oil-based nanofluids, they added oleic acid as surfactant. In the case of EG based nanofluids, no surfactant was needed due to the low viscosity of the fluid. Bhalla and Tyagi (2017) prepared Co_3O_4-DIW nanofluids by dispersing Co_3O_4 nanoparticles in DIW.

Table 2.2: Summary of Co_3O_4 nanofluids preparation

Author (s)	Co_3O_4 particle size, shape & synthesis method	Base fluid	Particle concentration (vol% or wt%)	Nanofluid enhancement stability technique	Nanofluid stability inspection technique	Stability duration
Vickers et al. (2009)	D ≤ 65 nm Cubic One step approach	PEG-MW 400 (oligomeric)	0.1, 0.25, 0.60, 36, 39, 41 & 62 vol%.			Stable during experimentation period
Fazlali et al. (2012)	D < 50 nm (commercial)	Pure liquid paraffin	5, 10, 15, 20, 25, 30 & 40 wt%	Surfactant (OA) Ultrasonic agitation		Stable during experimentation period
Hosseini et al. (2012)	D < 50 nm (commercial)	Pure liquid paraffin	5, 10, 15, 20, 25, 30 & 40 wt%	Surfactant (OA) Ultrasonic agitation		
Mariano et al. (2015)	D < 50 nm (commercial)	EG	≤ 25 wt%	Ultrasonic agitation	Spectral analysis	Stable during experimentation period
Katiyar et al. (2016)	D~25 nm (commercial) Oblate	EG and therminol 55	1.0, 2.0, 3.0, 4.0, 5.0, 6.0 & 7.0 vol%	Surfactant (OA for oil-based nanofluids only) Ultrasonic agitation		
Bhalla and Tyagi (2017)	D = 10-30 nm (commercial)	DIW	0.002, 0.004 & 0.006 wt%	Surfactant (triton X-100) Ultrasonic agitation	Sedimentation photograph capturing technique	More than 24 h
Sekhar et al. (2017) & Sekhar et al. (2018)	D = 50 nm (commercial)	DIW	0.1, 0.2, 0.3 & 0.4 vol%	Surfactant (decyl glucoside) Ultrasonic agitation		Stable during experimentation period
Rajaee et al. (2020)	D = 10-30 nm (commercial)	DW	0.25, 0.50 & 1 %	Surfactant (arabic gum) Ultrasonic agitation		
Gupta et al. (2021)	D = 25-50 nm Truncated octahedron Co-precipitation	EG	0.2, 0.4, 0.6, 0.8 & 1.0 wt%	Ultrasonic agitation		
Mei et al. (2021)	D= 20 and 50 nm (commercial)	Neat diesel (0#)	0.006, 0.012 & 0.018 wt%	Surfactant (CTAB) Ultrasonic agitation	Zeta potential	3 days
Mitra et al. (2021)	D < 50 nm (commercial) Nanorods (27 nm) & nanoflowers (32 nm) Hydrothermal synthesis	DIW	0.0005, 0.003, 0.005, 0.008 & 0.011 wt%	Ultrasonic agitation	Zeta potential	
Raki et al. (2021)	D ± 45 nm (commercial) Semi-spherical	DIW	0.005, 0.01, 0.05, 0.1, and 0.2 vol%	Surfactant (SDS) Ultrasonic agitation	Zeta potential	

Alsboul et al. (2022)	D ≤ 50 nm (commercial)	DW, EG, 60EG/40DW, 40EG/60DW and 20EG/80DW	0.025, 0.05, 0.10, 0.20 & 0.40 vol%	Ultrasonic agitation		
Manoram and Moorthy (2022)	D = ± 50 nm (commercial) Spherical	DIW	0.2 & 0.4 vol%	Surfactant (CTAB) Ultrasonic agitation	Zeta potential	1 week (without surfactant) 25 days (with surfactant)
Rahman Salari et al. (2022)	D = 50 nm Cubic Precipitation	25DW/75EG	0.1, 0.3 and 0.5 wt%	Surfactant (SDS) Ultrasonic agitation pH control	Sedimentation photograph capturing technique	4 weeks

To prevent the agglomeration of particles, they added a non-ionic surfactant (triton X-100) below the critical micelle concentration. Then, the whole mixture was sonicated for ~40 min using a probe-type sonicator. Using the sedimentation photograph capturing technique, they reported that the samples were stable beyond 24 h. Sekhar et al. (2017) dispersed Co_3O_4 nanoparticles in DIW. Then, the mixture was mechanically stirred for 1 h at 60 °C to obtain a stable suspension. To improve the stability of Co_3O_4-DIW nanofluids, few drops of non-ionic surfactant (decyl glucoside) were added to the mixture, and it was subjected to ultrasonication at 70 W for 7 h using an ultrasonic cleaner (40 kHz). They obtained Co_3O_4-DIW nanofluids without agglomeration. Sekhar et al. (2018) conducted a similar study to that by Sekhar et al. (2017). In their case, the mixture of Co_3O-DIW nanofluids were mechanically stirred for 1 h at 30 °C to obtain stable suspensions. The rest of the nanofluids preparation procedure was similar to that used by Sekhar et al. (2017). Rajaee et al. (2020) prepared Co_3O_4-DIW nanofluids by adding the nanoparticles gradually to DIW while using a magnetic stirrer to disperse properly the nanoparticles in the fluid. To prevent the agglomeration of particles, a surfactant (arabic gum) was added to the mixture. Then, the mixture was subjected to sonication using an ultrasonic cleaner device (300 W) for 45 min. Gupta et al. (2021) dispersed Co_3O_4 nanoparticles in EG to obtain nanofluids at different weight concentrations. They sonicated the nanofluids for 4 h at a frequency of 4 MHz to obtain a uniform suspension. Mei et al. (2021) mixed Co_3O_4 nanoparticles with the surfactant CTAB which mass was the same as that of nanoparticles, to prevent the agglomeration of nanoparticles. The mixture was then added to a certain amount of the base fluid (neat diesel) to obtain the nano-fuels. Then, the mixture was oscillated in an ultrasonic processor (150 W and 40 Hz) for 30 min, under 25 °C as the water bath temperature. A zeta potential analysis was conducted to determine the stability of nanofluids, and the results revealed favourable stability even after 3 days. Mitra et al. (2021) dispersed flower and rod like Co_3O_4 nanoparticles in DIW, respectively. The mixture was sonicated for 1 h using a high-energy probe (750 W) in a water bath to control the temperature of the nanofluid. Then, the mixture was subjected to mechanical stirring at room temperature for 15 min. No surfactant was used to formulate the nanofluids. Results from the zeta potential analysis revealed that the flower like nanofluids (-21.3 mV) were more stable than rod like based nanofluids (-14.9 mV). Raki et al. (2021) prepared Co_3O_4-DIW nanofluids. To facilitate the homogenous dispersion of particles, a surfactant (SDS) was added to the suspension. The suspension was placed in a warm bath at 40 °C and while stirring at 1100 rpm for 24 h. Then, the mixture was sonicated in an ultrasonic device (60% intensity) for 1 h and 20 min to remove any agglomeration present in the suspensions. Zeta potential analysis was used to evaluate the stability of Co_3O_4-DIW nanofluids. In the absence of SDS, the results revealed that the zeta potential of Co_3O_4 nanoparticles in DIW is > -40 mV, which indicates the moderate stability of nanoparticles in DIW. However, in presence of SDS, the zeta potential of Co_3O_4

nanoparticles in DIW was -114.19 mV, which indicates the extremely good stability of the nanofluids. Alsboul et al. (2022) dispersed Co_3O_4 nanoparticles in various base fluids namely DW, EG, 60EG/40DW, 40EG/60DW and 20EG/ 80DW. Various volumetric concentrations ranging from 0.025 to 0.4 % were prepared, subjected to magnetic stirring for 3 h and finally sonicated in an ultrasonic cleaner at frequency of 40 Hz for 40 min. Manoram and Moorthy (2022) dispersed Co_3O_4 nanoparticles in DW then, they sonicated the mixture for 2 h with an ultrasonic vibrator (100 W and 50 Hz) for the homogenous dispersion of nanoparticles in the fluid. To prevent their agglomeration, a surfactant (CTAB) was added to the suspension. The amount of CTAB was taken as 10% of the mass of Co_3O_4 nanopowder. They determined the stability of nanoparticles in DW with and without surfactant by using the zeta potential technique. The 0.2 vol% nanofluid with surfactant was found to be more stable (39.3 mV) than that without surfactant (36.8 mV). The nanofluid with surfactant was stable for 25 days without any sedimentation. The stability of the nanofluid without surfactant lasted for 7 days and it required a periodical sonication of 1 h per week to diminish the chances of sedimentation. Rahman Salari et al. (2022) dispersed Co_3O_4 nanoparticles in 25DW/75EG. SDS (surfactant) which mass was equal to the mass of nanoparticles for each sample was added to improve the dispersion of particles in the fluid. Then, the best stabilization of nanofluids was obtained after sonicating the nanofluids for 360 min and maintaining the fluid pH at 8. The samples were observed to be stable for over 4 weeks.

Table 2.2 also provides information about the effect of Co_3O_4 particle size, particle shape and particle concentration on the stability of the resulting nanofluids:

- **Effect of particle size**

Mitra et al. (2021) dispersed Co_3O_4 nanoflowers and nanorods in DIW, respectively. Co_3O_4 nanoflowers had a particle size of 32 nm while that of nanorods was 27 nm. After 1 h of probe sonication (750 W) and 15 min of mechanical stirring at room temperature the flower based nanofluids (-21.3 mV) were found to be more stable than rod based nanofluids (-14.9 mV). Mitra et al. (2021) did not comment on the impact of Co_3O_4 particle size on the stability of their nanofluids. It can be hypothesized that the dispersion of large Co_3O_4 particles in DIW can improve the stability of Co_3O_4-DIW nanofluids. Previous studies have shown that particle size affects both the Van der Waals attractive force and electrical double layer repulsive force. For instance, He et al. (2008) investigated the effect of different particle sizes (12(±2), 32(±3), and 65(±3) nm) of hematite (α-Fe_2O_3) nanoparticles on the stability of their respective suspensions. At constant pH conditions and ionic conditions, the tendency of aggregation increased with decreasing particle size (He et al., 2008). They found that an increment in particle size caused a decrease in the attractive potential while the repulsive and total interaction potential increased significantly. These trends were due to the higher surface

energy of smaller particles which led smaller particles to aggregate more than larger particles to lower the free energy of the system (He et al., 2008).

- **Effect of particle shape**

Mitra et al. (2021) dispersed Co_3O_4 nanorods and nanoflowers in DIW, respectively. The mixture was sonicated for 1 h and mixed at room temperature for 15 min. No surfactant was used to formulate the nanofluids. Results from the zeta potential analysis revealed that the flower based nanofluids (-21.3 mV) were more stable than rod based nanofluids (-14.9 mV). Prior studies investigated the impact of different particle shapes on the stability of nanofluids. For instance, Kim et al. (2015) investigated the effect of brick shaped, platelet shaped and blade shaped alumina particles on the stability of alumina-H_2O nanofluids. Using the laser scattering method, brick shaped alumina nanofluids were more stable than platelet and blade shaped alumina nanofluids. Kim et al. (2015) validated their experimental results by calculating the total interaction potential of nanoparticles with respect to particle shape as per the classical DLVO theory. They observed that particle shape only affected the repulsive potential while the attractive potential depended on the particle concentration. Brick shaped particles exhibited the highest repulsive potential whereas the lowest was obtained for blade shaped particles. According to Kim et al. (2015), the repulsive interaction energy is affected by the surface area which is function of the particle shape. Since brick shaped particles have a greater surface area than other particles, they exhibit a higher repulsive interaction energy.

- **Effect of particle concentration**

Manoram and Moorthy (2022) reported the effect of Co_3O_4 particle concentration on the stability of Co_3O_4-DW nanofluids with and without surfactant (CTAB) by using the zeta potential analysis. In the absence of CTAB, an increase in particle concentration (from 0.2 to 0.4 vol%) induced a reduction in zeta potential from 36.8 to 30.9 mV. In presence of CTAB, the same trend was observed with zeta potential reducing from 39.3 to 36.6 mV. Previous studies also reported poor stability of nanofluids at higher particle concentration (Chakraborty et al., 2015; Chakraborty et al., 2018; Zhang et al., 2021). An increase in particle concentration induces a reduction in the average particle separation distance resulting in a greater Van der Waals attractive potential. It is known that when Van der Waals attractive potential dominates over electrostatic repulsive potential, particle agglomeration occurs thereby causing the above trend.

2.8 Properties of Co_3O_4 nanofluids

The addition of nanoparticles to a conventional fluid significantly alters the thermophysical and transport properties of the resulting nanofluids (Suganthi & Rajan, 2017). According to Chen and Ding (2009), the thermal conductivity and viscosity are the properties most relevant to the flow and heat transfer of nanofluids. Previous studies have shown that the

thermophysical properties of nanofluids affect their heat transfer performance (Xuan & Li, 2003; Anoop et al., 2009). In a system, the viscosity of a fluid directly affects its pressure drop and pumping power, while the thermal conductivity of a fluid indicates its heat transfer efficiency. For this study, the properties to be investigated are the thermal conductivity and viscosity of Co_3O_4 nanofluids.

2.8.1 Viscosity of Co_3O_4 nanofluids

In all heat transfer applications, viscosity is important, it is the internal resistance force of a fluid (Špeťuch et al., 2015). Rheology, however, describes how the viscosity of a fluid or suspension responds to different rates of shearing or stirring (Funk & Dinger, 1994). Viscosity (μ) is expressed as the ratio between shear stress (τ) and shear rate(γ) (Nadooshan et al., 2018). Shear stress is the shear force per unit area, while shear rate is the strain change over time. The rheological behaviour of fluids is governed by the relationship between the shear rate and shear stress. Based on rheology, two types of fluids can be distinguished namely Newtonian and non-Newtonian fluids as illustrated in Figure 2.15. According to Chhabra and Richardson (1999:1-5), a Newtonian fluid has a flow curve (plot of shear stress vs shear rate) which passes through the origin, at a fixed temperature and pressure. In other words, the viscosity of a Newtonian fluid is independent of the shear rate. A non-Newtonian fluid, on the other hand, has a flow curve that does not pass through the origin (Fester et al., 2012) (the apparent viscosity of a fluid is not constant at a given temperature and pressure, but is affected by flow conditions such as flow geometry and shear rate, and sometimes even by the kinematic history of the fluid). In other words, a non-Newtonian fluid has a viscosity that varies with shear rate.

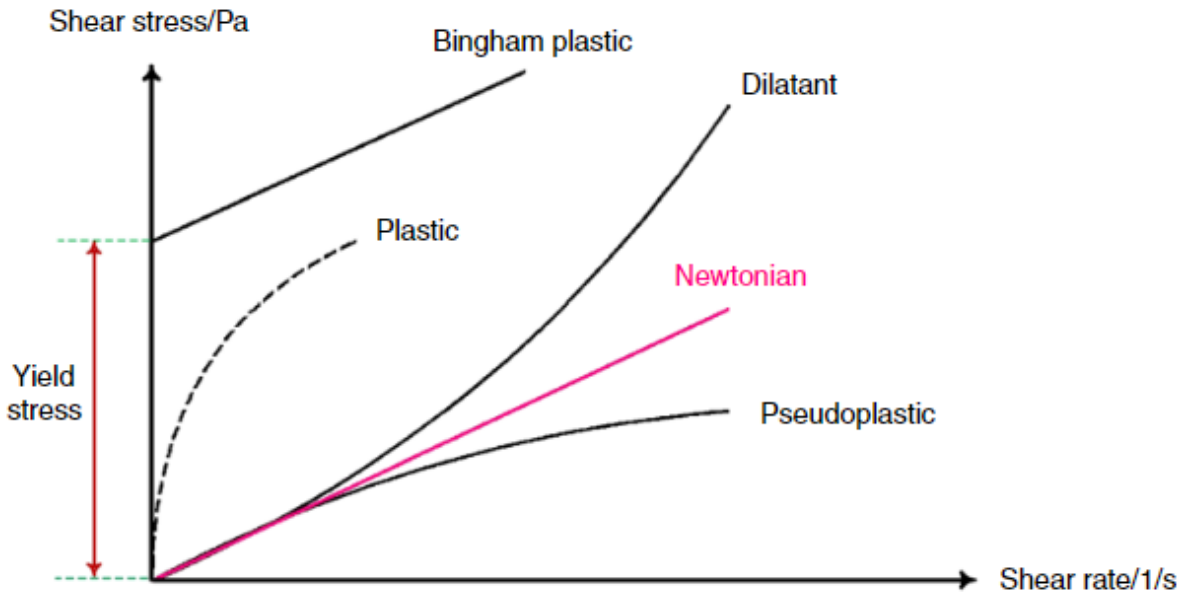

Figure 2.15: Shear stress and shear rate diagram for Newtonian and non-Newtonian fluids (Yang & Du, 2020)

Non-Newtonian fluids are divided in three classes (Chhabra & Richardson, 1999:5-21):

- **Time independent fluid behaviour**: where the shear rate at any point is determined entirely by the shear stress at that point at that time. They contain three subclasses of fluids namely, shear thinning or pseudoplastic, viscoplastic and shear thickening or dilatant.
- **Time dependent fluid behaviour**: where the viscosity depends on the shear rate but also on the time for which the fluid has been subjected to shearing. They contain two subclasses of fluids namely, thixotropic and rheopexic (or negative thixotropic)
- **Visco-elastic fluid behaviour**: contain fluids displaying the characteristics of both ideal fluids and elastic solids and showing partial elastic recovery after deformation.

Similarly, to conventional fluids the rheology of nanofluids is studied using a rheometer having a variety of geometries to measure viscosity versus a range of shear rates when the nanofluids are sheared. Both types of rheological behaviour have been observed in nanofluids (Bhanvase & Barai, 2021:128-131). As a result of adding nanoparticles to fluids, not only is their thermal conductivity increased, but also their viscosity (Colla et al., 2012; Esfe & Saedodin, 2014; Karimi-Nazarabad et al., 2015; Baratpour et al., 2016; Ansari et al., 2018; Kamila & Venugopal, 2019).

A summary of the experimental studies conducted on the viscosity of Co_3O_4 nanofluids is provided in Table 2.3 below. As indicated in the table, the Co_3O_4 particle size and shape, their concentration, the base fluid, the shear rate range and the temperature, which the experiments were conducted at, were considered. The effects of Co_3O_4 particle size, particle

shape, particle concentration and temperature on the viscosity of their nanofluids are discussed below:

- **Effect of temperature**

Mariano et al. (2015) studied the rheological behaviour of Co_3O_4-EG nanofluids using a MCR 101 rheometer with a cone-plate geometry from 10 to 50 °C (10 °C steps). They reported a decrease in shear viscosity with increasing temperature at shear rate range of 50 to 1000 s^{-1}. The Vogel–Fulcher–Tammann (VFT) three-coefficient expression was used to predict the viscosity-temperature dependence of Co_3O_4-EG nanofluids:

$$Ln(\eta) = A + \frac{B}{T - T_0} \quad \textbf{(2.9)}$$

Where A, B and T_0 are the fitting coefficients. The ratio B/T_0 is known as Angell strength coefficient

The equation was validated as accurate by obtaining the fitted values for the coefficients.

Sekhar et al. (2017) measured the viscosity of Co_3O_4-H_2O nanofluids using an Ostwald U-tube viscometer. They reported that when temperature increased from 30 to 60 °C (at 10 °C steps) this resulted in a 6% decrease in the relative viscosity (η_r) of Co_3O_4-H_2O nanofluids (at 0.3 & 0.4 vol%) and a 3% decrease in the relative viscosity of Co_3O_4-H_2O nanofluids (0.1 & 0.2 vol%). However, in another study Sekhar et al. (2018) reported a 3% decrease in the relative viscosity of Co_3O_4-H_2O nanofluids (for 0.4 vol%) as the temperature increased from 30 to 60 °C (at 10 °C steps). Gupta et al. (2021) measured the viscosity of Co_3O_4-EG nanofluids (0.2-1.0 wt%) using an Ostwald viscometer at 25, 30 and 35 °C. They reported that an increase in temperature resulted in a decrease in the relative viscosity of Co_3O_4-EG nanofluids. A raise in temperature weakened the intermolecular forces between the molecules in Co_3O_4-EG nanofluids resulting in the reduction of their relative viscosity (Gupta et al., 2021). Alsboul et al. (2022) measured the viscosity of Co_3O_4-DW, Co_3O_4-EG, Co_3O_4-60EG/40DW, Co_3O_4-40EG/60DW and Co_3O_4-20EG/80DW nanofluids at different volumetric concentrations (0.025-0.4 vol%) using a vibro viscometer in a temperature range of 20 to 60 °C (at 5 °C steps). In general, the viscosity of nanofluids decreased with increasing temperature. Co_3O_4-DW nanofluids exhibited the lowest viscosities (0.467 mPa.s) at 60 °C with 0.025 vol%. Co_3O_4-EG nanofluids had the highest viscosities (22 mPa.s) at 20 °C with 0.4 vol%. Rahman Salari et al. (2022) measured the viscosity of Co_3O_4-EG(75%)/DW(25%) nanofluids at various particle weight concentrations from 25 to 65 °C (at 20 °C steps). The viscosities of all nanofluids were found to decrease with increasing temperature. The explanation to the latter trend is that raising the temperature weakens the interparticle/intermolecular forces.

- **Effect of particle concentration**

Some studies have investigated the effect of particle concentration on the viscosity of Co_3O_4 nanofluids. Vickers et al. (2009) studied the rheological properties of Co_3O_4-PEG nanofluids. They used two mechanical rheometers (Paar Physica MCR and Rheometrics ARES) for two types of measurements namely controlled stress and controlled strain. The thickness of samples used along with the geometries for the measurements are as follows: 25mm diameter, 1° cone-and-plate, and 50mm diameter, 2° cone and plate fixtures. By using controlled-stress measurements, it was possible to characterize suspensions with high particle volume concentrations that exhibited yield stress. Controlled strain measurements were conducted on low particle volume concentrations at high shear rates. A temperature of 50 °C was chosen to maintain mechanical torques generated within the range of sensitivity of the rheometer. Considering the Newtonian nature of PEG and its low vapour pressure, it has been chosen as a base fluid. At low particle volumetric concentrations (≤ 0.1 vol%), the suspensions exhibited Newtonian behaviour with viscosities slightly above that of the suspending fluid (PEG). At moderately higher, yet still quite low particle concentrations (0.25 and 0.6 vol%), the suspensions exhibited shear thinning behaviour at low shear rates, but at higher rates, they displayed approximate Newtonian behaviour. Shear thinning behaviour has been attributed to the presence of low viscosity particle superstructures such as layers (Ackerson, 1991) and strings (Won & Kim, 2004) where thinning is caused by shear induced slippage of these layers, reducing the hydrodynamic resistance caused by nanoparticles. From 36 vol%, a transition from shear thinning to shear thickening was observed. At shear rates values greater than 1000 s^{-1}, a continuous shear thickening behaviour was explored. Moreover, a comparison between experimental data and theoretical predictions was reported. For low volumetric concentrations, the obtained results were extracted at a shear rate of ± 50 s^{-1}. For high volumetric concentrations, the results were extracted at a point where suspensions exhibited a minimum viscosity (the transition region from shear thinning to shear thickening). The first model used was from the Einstein expression for a suspension of hard spheres ($\emptyset$<0.01) with as illustrated in Equation 2.10:

$$\eta = \eta_s(1 + 2.5\emptyset) \quad \textbf{(2.10)}$$

Where η, η_s, $\emptyset$ are the suspension viscosity, , the solvent viscosity and the particle volume fraction, respectively.

The second model for hard-core particles of arbitrary shape was a modified Krieger–Dougherty formula presented in Equation 2.11 below:

$$\eta_r = \frac{\eta}{\eta_s} = \left(1 - \alpha \frac{\emptyset}{\emptyset_m}\right)^{-[\eta]\emptyset_m} \quad \textbf{(2.11)}$$

Where η, η_s, η_r, α, $\emptyset$, $\emptyset_m$ are respectively, the suspension viscosity, solvent viscosity, relative viscosity, particle-swelling ratio (1.00 and ~4.45), particle volume fraction and maximum packing factor.

They found that the Krieger-Dougherty equation along with particle swelling ratio (α) fitted well the experimental data for the Co_3O_4-PEG based nanofluids at low and high particle volume fractions.

Fazlali et al. (2012) studied the rheological properties of Co_3O_4-paraffin based nanofluids. They used a MCR300 rheometer from Anton Paar GmbH fitted with a special plate-plate spindle MRD 180. They reported the flow curves (shear stress vs shear rate) for Co_3O_4 nanofluids for a wide range of weight concentrations (5-40 wt%). For 5 wt%, Co_3O_4-paraffin nanofluids displayed almost Newtonian behaviour. For 10 wt%, the nanofluids exhibited Newtonian behaviour but as the shear rate increased, they exhibited shear thinning behaviour. Between 15 to 40 wt%, they noticed that the nanofluids displayed exhibited shear thinning behaviour, as their viscosities decreased with an increment in shear rate.

Table 2.3: Past experimental studies on the rheological behaviour of Co_3O_4 nanofluids

Author (s)	Co_3O_4 particle size & shape	Base fluid	Particle concentration (wt% or vol%)	Shear rate and temperature range	Viscosity-particle size relationship	Viscosity-particle concentration relationship	Viscosity-temperature relationship	Summarised results
Vickers et al. (2009)	D ≤ 65 nm Cubic	PEG (oligomeric)	0.1, 0.25, 0.60, 36, 39, 41 & 62 vol%.	0.1-1000 s^{-1} (low vol%) 1-4000 s^{-1} (high vol%) T= 50 °C	None	Einstein model (η=4.6) Modified Krieger–Dougherty model (α= 1 and α= 4.45)	None	-For suspensions ≤ 0.1 vol%: Newtonian behaviour -For suspensions from 0.25 to < 36 vol%: shear thinning and Newtonian behaviour -For suspensions ≥ 36 vol%: shear-thinning then shear-thickening behaviour -Experimental data were best fitted with Krieger-Dougherty model
Fazlali et al. (2012)	D < 50 nm (commercial)	Liquid paraffin	5, 10, 15, 20, 25, 30 & 40 wt%	0.1-1000 s^{-1}	None	Einstein model with b=5 and c=53. Chow model with A=4.67. Modified Krieger–Dougherty formula (η=2.5 and η= 2.925)	None	-Suspensions at 5 wt%, exhibited almost Newtonian behaviour -Suspensions at 10 wt%, exhibited Newtonian then shear thinning behaviour. -Between 15 and 40 wt%, suspensions exhibited shear thinning behaviour and yield stress -Experimental data did not correlate with the model results
Hosseini et al. (2012)	D ~21nm (commercial) Assumed spherical	Liquid paraffin	5, 10, 15, 20, 25, 30 & 40 wt%	0.1-1000 s^{-1}	None	-Modified Einstein model with k_H= 2.5. -Chow model with A=4.67. -Modified Krieger–Dougherty formula (η=2.5 and η= 2.925)	None	-Shear thinning behaviour has been observed for all particle concentrations. -Models failed to agree well with experimental results

Mariano et al. (2015)	D=17 nm (commercial)	EG	5, 10, 15, 20 and 25 wt%	50-1000 s^{-1} T= 10-50 °C	None	Einstein model (N=1 & C_1= 2.5) Chow model (N=1& C_1= 7.1) Modified Krieger–Dougherty formula (η=2.5)	Vogel–Tammann–Fulcher correlation equation	-Viscosity increment with increasing particle wt% but decreasing with increasing temperature -At 25 wt%, viscosity increase of 40% was obtained. -Results obtained from VTF equation were validated as accurate -Only the Krieger-Dougherty model fitted well with the experimental data
Sekhar et al. (2017)	D± 50 nm (commercial)	DIW	0.1, 0.2, 0.3 & 0.4 vol%	T= 30-60 °C	None	None	None	-Temperature increase resulted in viscosity ratio decreasing by 6% (at 0.4 vol% & 0.3 vol%) and by 3% (at 0.2 vol% & 0.1 vol %). -η_r increase with an increase in particle vol%.
Sekhar et al. (2018)	D± 50 nm (commercial)	DIW	0.1, 0.2, 0.3 & 0.4 vol%	T= 30-60 °C	None	None	None	-η_r decreased by 3% (at 0.4 vol%) when increasing the temperature. -A 15 % increase in η_r with an increase in particle vol%.
Gupta et al. (2021)	D= 25-50 nm Truncated octahedron	EG	0.2, 0.4, 0.6, 0.8 & 1.0 wt%		None	None	None	-η_r decreased with increasing temperature -η_r increased with increasing particle wt% up to 0.4 wt%. -Above 0.4 wt%, η_r decreased with increasing particle wt%.
Alsboul et al. (2022)	D= ≤ 50 nm	DW EG 20EG/80DW 40EG/60DW 60EG/40DW	0.025, 0.05, 0.10, 0.20 & 0.40 vol%	T= 20 to 60 °C (at 5 °C steps)	None	Einstein model Batchelor model Brinkman model	None	-η_r decreased with increasing temperature and increased with increasing particle vol% -η_r of Co_3O_4-40EG/60DW nanofluids was enhanced by 0.70% and 1.61% at 0.025 vol% and 0.4 vol% at 20 °C and 60 °C, respectively. -Einstein model fitted well with the experimental data.
Rahman Salari et al. (2022)	D= 50 nm Cubic	25DW/ 75EG	0.1, 0.3 and 0.5 wt%	T= 25 to 65 °C (at 20 °C steps)	None	None	None	η_r decreased with increasing temperature and increased with increasing particle wt%

They also displayed yield stress which was attributed to a rise in nanoparticle interaction resulting in a resistance against fluid motion.

Three models were used to compare the experimental flow curves and those obtained from theoretical models. The first model was that of Bingham using Equation 2.12 below:

$$\tau = \tau_y + \eta_0 \dot{\gamma} \quad \textbf{(2.12)}$$

Where τ, τ_y, η_0, γ are the shear stress, yield stress, viscosity at zero field and shear rate, respectively.

The Bingham model agreed well with the Co_3O_4-paraffin nanofluids at low particle concentrations whereas at high particle concentrations, the model was not satisfactory. Therefore, they proposed another model including yield point called Casson model (Mezger, 2012) as shown below:

$$\tau^{1/2} = \tau_y^{1/2} + \eta_0^{1/2} \dot{\gamma}^{1/2} \quad \textbf{(2.13)}$$

Casson model showed good agreement with the Co_3O_4-paraffin nanofluids at different particle concentrations. Another model by Hurschel-Bulkley (Hong et al., 2007) as shown in Eq. 2.14 was also used and it was found to be the best fit for Co_3O_4-paraffin nanofluids at different concentrations.

$$\tau = \tau_y + K\dot{\gamma}^n \quad \textbf{(2.14)}$$

Three models were used to determine the effect of particle concentration on the viscosity of nanofluids. The Einstein model which does not account for the particle size but is only valid for diluted suspensions, was represented in Equation 2.15 as follows (Einstein, 1906):

$$\eta_s = \eta_l(1 + k_H \emptyset) \quad \textbf{(2.15)}$$

Where η_s, η_l and k_H are the suspension viscosity, base fluid viscosity and shape factor equating 2.5 for spherical particles.

A modified version of Einstein model (Hunter, 2001) which is valid for concentrated colloidal suspensions was also used:

$$\eta_s = \eta_l(1 + 2.5\varphi_h + 6.2\varphi_h^2) \quad \textbf{(2.16)}$$

Where φ_h is the hydrodynamic volume fraction (particle concentration of ferrofluids)

The second model was that of Chow in which particle interactions were considered with A= 4.67 (Chow, 1993) as expressed in Equation 2.17:

$$\frac{\eta}{\eta_0} = exp\left(\frac{2.5\varphi_h}{1-\varphi_h}\right) + \frac{A\varphi_h^2}{1-A\varphi_h^2\varphi_m} \quad \textbf{(2.17)}$$

Where A, φ_m are the coupling coefficient and maximum hydrodynamic volume fraction, respectively.

The third model was that of Krieger–Dougherty (Hunter, 2001) with the values of η taken as 2.5 and 2.925 for spherical particles as shown below:

$$\eta = \eta_s\left(1 - \frac{\varphi_h}{\varphi_m}\right)^{-[\eta]\varphi_m} \quad \textbf{(2.18)}$$

Where η is the intrinsic viscosity.

They found that experimental results of Co_3O_4-paraffin nanofluids did not agree well with those obtained from theoretical model equations.

Hosseini et al. (2012) also studied the rheological properties of Co_3O_4-paraffin based nanofluids. They also used a MCR300 rheometer from Anton Paar GmbH fitted with a plate-plate spindle (PP25-MRD, diameter = 1.95 cm). They observed a shear thinning behaviour for all the concentrations due to a decrease in viscosity as the shear rate increased. This was due to the presence of weak bonds between particles. They used similar models (Einstein, Chow and Krieger-Dougherty) as those used in the study of Fazlali et al. (2012). They noticed that theoretical results failed to agree well with experimental results of Co_3O_4-paraffin nanofluids most especially at higher particle concentrations. In fact, since these models do not consider particle-to-particle interactions, these results are not surprising at higher particle concentrations. Mariano et al. (2015) investigated the rheological properties of Co_3O_4-EG nanofluids as a function of particle concentration. A Physica MCR 101 rheometer was used to analyse the rheological behaviour of nanofluids. A cone-plate geometry with a cone diameter (25 mm) and angle of 1°, respectively was used. The nanofluid samples were analysed with a constant gap quantity of 0.048 mm, and the temperature was controlled with a Peltier system. For all particle concentrations (5-25 wt%), a Newtonian behaviour was observed at 30 °C. Furthermore, the shear viscosity increased with an increment in particle weight concentration, as expected. For suspensions of 25 wt%, a viscosity increase (η_r) of 40% was observed.

Three classical approaches (Einstein, Chow and Krieger-Dougherty) were used to correlate the increment in viscosity with respect to particle volume fraction. The Chow model was represented in Equation 2.19 as follows:

$$\eta_r = \frac{\eta_{nf}}{\eta_0} = 1 + \sum_{i=1}^{N} C_i \emptyset^i \quad \textbf{(2.19)}$$

Where η_r, η_{nf}, η_0, N, C_i are the relative viscosity, nanofluid viscosity, base fluid viscosity, degree of polynomial and corresponding correlation coefficients, respectively. If N=1 and C_1=2.5, Equation 2.19 reduces to Einstein equation. The Einstein model significantly underestimated the viscosity increment with increasing concentration. They noted a 0.8% deviation for the Chow model. A modified version of the Krieger-Dougherty model for dispersions of equal sized hard spheres was used as presented in Equation 2.20 below:

$$\eta_r = \left[1 - \frac{\emptyset}{0.605}\left(\frac{a_a}{a}\right)^{1.2}\right]^{-1.5125} \quad \textbf{(2.20)}$$

Where a_a and a represent the estimated radius of aggregates and single particles.

Initially, the radius of aggregates was assumed to be function of particle concentration. Then, the a_a/a ratio was determined for each concentration, yielding results ranging from 1.9 to 2.3. The Krieger-Dougherty model represented well the experimental results of Co_3O_4-EG nanofluids viscosity. Sekhar et al. (2017) investigated the effect of different particle volumetric concentration on the viscosity of Co_3O_4-DIW based nanofluids. To measure the viscosity of Co_3O_4-DIW based nanofluids, they made use of an experimental arrangement consisting of an electric temperature bath, stirrer, and Ostwald U-tube. They reported an increment in the relative viscosity with an increment in particle concentration. In another study, Sekhar et al. (2018) found that an increase in particle volume concentration led to a 15% increase in the relative viscosity of Co_3O_4-DIW nanofluids. Gupta et al. (2021) measured the viscosity of Co_3O_4-EG nanofluids (0.2-1.0 wt%) using an Ostwald viscometer at 25, 30 and 35 °C. They noted a decrease in the relative viscosity of Co_3O_4-EG nanofluids when increasing the particle volumetric concentration up to 0.4 wt%. Above the latter concentration, an increase in the relative viscosity of Co_3O_4-EG nanofluids with an increase in particle volumetric concentration was noted. The initial reduction in relative viscosity of nanofluids was attributed to mild perturbation in hydrogen bonding network of EG due to interaction between nanoparticles and EG molecules after the addition of Co_3O_4 nanoparticles to EG (Suganthi et al., 2014). Alsboul et al. (2022) measured the viscosity of Co_3O_4-DW, Co_3O_4-EG, Co_3O_4-20EG/80DW, Co_3O_4-40EG/60DW and Co_3O_4-60EG/40DW nanofluids using a vibro viscometer in a temperature range of 20 to 60 °C (at 5 °C steps). Various volumetric concentrations ranging from 0.025 to 0.4 vol% were prepared to determine the effect of particle concentration on the relative viscosity of nanofluids. In general, the viscosity of nanofluids increased with increasing volumetric concentration. In the case of base fluids (DW and EG), the relative viscosity of Co_3O_4-DW nanofluids was enhanced by 0.06% and 0.96%, whereas that of Co_3O_4-EG nanofluids was improved by 0.01% and 0.92%, for 0.025 vol% and 0.4 vol% at 20 °C, respectively. In the case of EG-DW

mixture nanofluids, the relative viscosity of Co_3O_4-20EG/80DW nanofluids was enhanced by 1.16% and 2.07% for 0.025 vol% and 0.4 vol% at 20 °C, respectively, compared to 20EG/80DW mixture. The relative viscosity of Co_3O_4-40EG/60DW nanofluids was enhanced by 0.70% and 1.61% for 0.025 vol% and 0.4 vol% at 20 °C, respectively, compared to 40EG/60DW mixture. The relative viscosity of Co_3O_4-60EG/40DW nanofluids was enhanced by 7.45% and 6.54% for 0.025 vol% and 0.4 vol% at 20 °C, respectively, compared to 60EG/40DW. Three models namely Einstein (1906), Batchelor (1977) and Brinkman (2004) were used to correlate the viscosity ratio with respect to particle volumetric concentration of Co_3O_4-DW and Co_3O_4-EG nanofluids at 20 °C. The experimental data were found to be in good agreement with the theoretical data obtained from the Einstein model. Rahman Salari et al. (2022) measured the viscosity of Co_3O_4-75EG/25DW nanofluids at various particle weight concentrations from 25 to 65 °C (at 20 °C steps) using a falling ball viscometer. The viscosities of all nanofluids were found to increase with increasing weight concentrations. The latter trend can be attributed to an increase in internal viscous shear stress in nanofluids as particle weight concentration is increased.

- **Effect of particle size**

Previous studies have examined the effect of particle size on the viscosity of various nanofluids, but to our knowledge, no study has examined the effect of particle size on the viscosity of Co_3O_4 nanofluids, and thus, the studies of other metallic and metal oxide-based nanofluids are reviewed to understand the relationship between the particle size and viscosity of nanofluids. On one hand, Nguyen et al. (2007) investigated the Al_2O_3 particle size effect on the viscosity of Al_2O_3–H_2O nanofluids from 20 to 50 °C. They noticed that, at 4 vol%, 36 and 47 nm Al_2O_3–H_2O nanofluids exhibited almost the same viscosity. In another study by Nguyen et al. (2008), at higher particle volume concentrations (7 and 9 vol%), fluids containing bigger size nanoparticles (47 nm) showed higher viscosity than the smaller ones (36 nm). They proposed the following viscosity correlations namely Equations 2.21 and 2.22 for 47 nm and 36 nm water-based alumina nanofluids, respectively:

$$\frac{\mu_{nf}}{\mu_{bf}} = 0.904e^{0.148\varphi} \quad \textbf{(2.21)}$$

$$\frac{\mu_{nf}}{\mu_{bf}} = 1 + 0.025\varphi + 0.015\varphi^2 \quad \textbf{(2.22)}$$

Where φ and μ are, respectively, particle volume fraction and fluid viscosity. The subscripts *bf*, *nf* and *r* refer respectively to the base-fluid, nanofluid and nanofluid to base fluid ratio of viscosity.

He et al. (2007) investigated the viscosity of TiO_2–DW nanofluids at different particle sizes (95 and 145 nm). They reported a linear relationship between the viscosity of nanofluids and the particle size at 22 °C. Jarahnejad et al. (2015) measured the viscosity of Al_2O_3–H_2O nanofluids from 20 to 50 °C. They investigated the effect of particle size (200 nm, 250 nm, and 300 nm) on the viscosity of alumina nanofluids at constant particle concentration (9 wt%). Their results showed that the viscosity of 200 nm nanofluids is lower than the nanofluids with 250 and 300 nm particle sizes. However, the nanofluids with 250 nm particle size showed up to 7 % higher viscosity than that with 300 nm. This trend was attributed to the inhomogeneous morphology of the three types of alumina particles which affected the results.

On the other hand, other researchers reported an opposite trend regarding the effect of particle size on the viscosity of nanofluids. Namburu et al. (2007) reported an increase in viscosity of SiO_2 nanofluids with a decrease in particle size (20, 50 and 100 nm) for SiO_2 nanoparticles dispersed in 60% EG and 40% water by weight. Their study was conducted at constant volumetric concentration (8 vol%) from -35 to 50 °C. Namburu et al. (2009) confirmed the same trend using the same SiO_2 nanoparticles at 6 vol%. Chevalier et al. (2007) also found the same trend when studying the viscosity of SiO_2–ethanol nanofluids from 1.1 to 7 vol% at three different particle sizes (35, 94 and 190 nm). Timofeeva et al., (2010) reported an increment in the viscosity of SiC-H_2O nanofluids with a decrease in particle size from 90 to 16 nm at a temperature range from 15 to 45 °C. Esfe et al. (2014) measured the viscosity of Fe-EG nanofluids at three different particle sizes (40, 70 and 100 nm) and volumetric concentrations ranging from 0.125 to 3 vol%. From 26 to 55 °C, they noted an increment in the nanofluids viscosity with a decrease in particle size. In another study, Esfe et al. (2015) studied the viscosity of Fe-EG nanofluids at three different particle sizes (37, 71 and 98 nm) and volumetric concentrations ranging from 0.0313 to 1 vol%. Using curve fitting, they proposed the following equation with viscosity as function of particle size and volume fraction lower than 1 vol%:

$$\frac{\mu_{nf}}{\mu_{bf}} = 1 + \left(0.1008\varphi^{0.6974} d_p^{0.44708}\right) \quad \textbf{(2.23)}$$

Where d_p is the particle size.

Rudyak et al. (2016) measured the viscosity of SiO_2-EG nanofluids at three different particle sizes (18.1, 28.3 and 45.6 nm) at 25 °C. They reported an increase in viscosity of nanofluids with a decrease in particle size. Minakov et al. (2016) confirmed the same behaviour for SiO_2-water nanofluids at three different particle sizes (10, 16, 25 and 100 nm) at 25 °C. Nanofluids with smaller particles had an increased viscosity because of higher surface area. This resulted in higher interfacial resistance with the fluid layer (Timofeeva et al., 2010; Agarwal et al., 2015).

Another trend was reported by other researchers, Prasher et al. (2006b) reported that the viscosity of Al_2O_3-propylene glycol nanofluids was not affected by the particle size of Al_2O_3 nanoparticles (27, 40 and 50 nm). Such behaviour was attributed to the agglomeration of nanoparticles.

Effect of particle shape

There has been no study examining the effect of particle shape on Co_3O_4 nanofluid viscosity. Timofeeva et al. (2009) investigated the effect of different particle shapes (platelets, blades, cylinders, and bricks) on the viscosity of Al_2O_3-EG/water (50% EG, 50% water by vol.) nanofluids. Nanoplatelets based nanofluids displayed the highest viscosity, followed by nanofluids based on cylinders, bricks, and blades. They found that elongated particles (cylinders) and agglomerates (bricks) had higher viscosities at the same volume fraction because of structural limitations of rotational and transitional Brownian motions. However, for lower viscosities, spherical particles and low aspect ratio spheroids were preferred. Jeong et al. (2013) investigated the effect of two different particle shapes (nearly rectangular and spherical) on the viscosity of ZnO-water nanofluids. They reported that the viscosity of nearly rectangular shaped particles was higher than that of spherical particles. This is because sphere-shaped particles rotate easily compared to the near rectangular ones.

2.8.2 Thermal conductivity of Co_3O_4 nanofluids

Heat is transferred from a hot body to a cold one. Heat can be transferred in three ways: conduction, convection, and radiation (Bejan & Kraus, 2003:2-3). Conduction of heat in solids or fluids occurs due to vibrations of molecules propagating to adjacent molecules, resulting in heat being transferred from the hot molecules to the cold ones. Solid objects rely heavily on this mechanism for heat transfer. This mode of heat transfer requires direct contact between molecules (Geankoplis, 2003). Heat convection occurs due to the physical motion of particles in a fluid. Convection can be classified into two types. Natural convection occurs when there is a density difference between the hot and cold fluid; forced convection is the result of mechanical mixing of hot and cold fluids (Geankoplis, 2003). Radiation is the transfer of heat between physically separated objects via electromagnetic waves (Geankoplis, 2003). In STC systems, heat is generally transferred via a combination of two or three modes of heat transfer. The heated metallic tubes of a solar thermal collector transfer heat via conduction to the outermost layer of the working fluid that is immediately in contact with the metal surface (Abed et al., 2020). When the fluid at the boundary of the tube is heated up, the difference in density between the nearby fluid layers causes circulation between them (Kalogirou, 2004; Liang et al., 2011). Due to this circulation over time, heat is transferred via convection to the innermost layers of the flowing fluid. According to Yang and Han (2006), nanoparticles function as heat boats to facilitate the heat transport. Nanoparticles can generate microconvection currents and enhance the thermal conductivity of the base fluid. The

increase in collision frequency can be attributed to an increase in the motion of molecules, which results in more heat being transferred. According to Bhanvase and Barai (2021:102-103), some mechanisms may explain the higher thermal conductivity exhibited by nanofluids. This includes the Brownian motion in nanoparticles, nanoparticles clustering, formation of liquid nanolayer around the nanoparticles, ballistic transport and nonlocal effects, thermophoresis, and near-field radiation (Figure 2.16).

Brownian motion: is the random movement of particles due to their collision with each other and with molecules of the fluid in which they are dispersed (Mitchell & Kogure, 2006). Nanoparticles can transport heat via conduction with the aid of this motion. In addition, a micro-convection effect, which is due to the fluid mixing around nanoparticles, is also proposed to be responsible for enhancement in the thermal performance of the base fluid (Bhanvase & Barai, 2021:102-103).

Clustering of nanoparticles: occurs when nanoparticles dispersed in a conventional fluid form clusters enabling the formation of a direct bond between nanoparticles and facilitating heat conduction. In fact, more heat is likely to flow though the formed clusters, due to their orientation along the direction of heat flux (Wang et al., 1999).

Liquid nanolayer formation around nanoparticles: occurs when the liquid molecules close to nanoparticle surfaces form layered structures. These structures behave like a solid which thickness is of a magnitude of nanometres (Yu et al., 2000). Liquid nanolayers are assumed to facilitate more effective thermal transport across the solid-liquid interface, by acting as a thermal bridge between nanoparticles and the base fluid (Murshed et al., 2008; Khamlich et al., 2023; Huang et al., 2024). The liquid nanolayer is expected to have a larger effective thermal conductivity than the bulk liquid (Yu & Choi, 2004).

Ballistic phonon transport in nanoparticles: In solids, heat is conducted via the vibration of atoms jointly held together. Phonons are quantized forms of energy released or lost by vibrating atoms (Yasmin et al., 2023). Solid materials can exhibit diffusive heat transport if the mean-free path of phonons is smaller than the characteristic size of the particle (Özerinç et al., 2010). Ballistic heat transport can significantly affect the thermal conductivity of nanofluids if it provides efficient heat transport between nanoparticles. However, this can only be achieved if the nanoparticles are very close (a few nanometres apart) and it was found that this was the case for nanofluids with very small nanoparticles (Keblinski et al., 2002).

Thermophoresis: occurs when particles in motion are subjected to the force of a temperature gradient (Godson et al., 2010). It produces localized convectional currents, thereby facilitating further heat transfer.

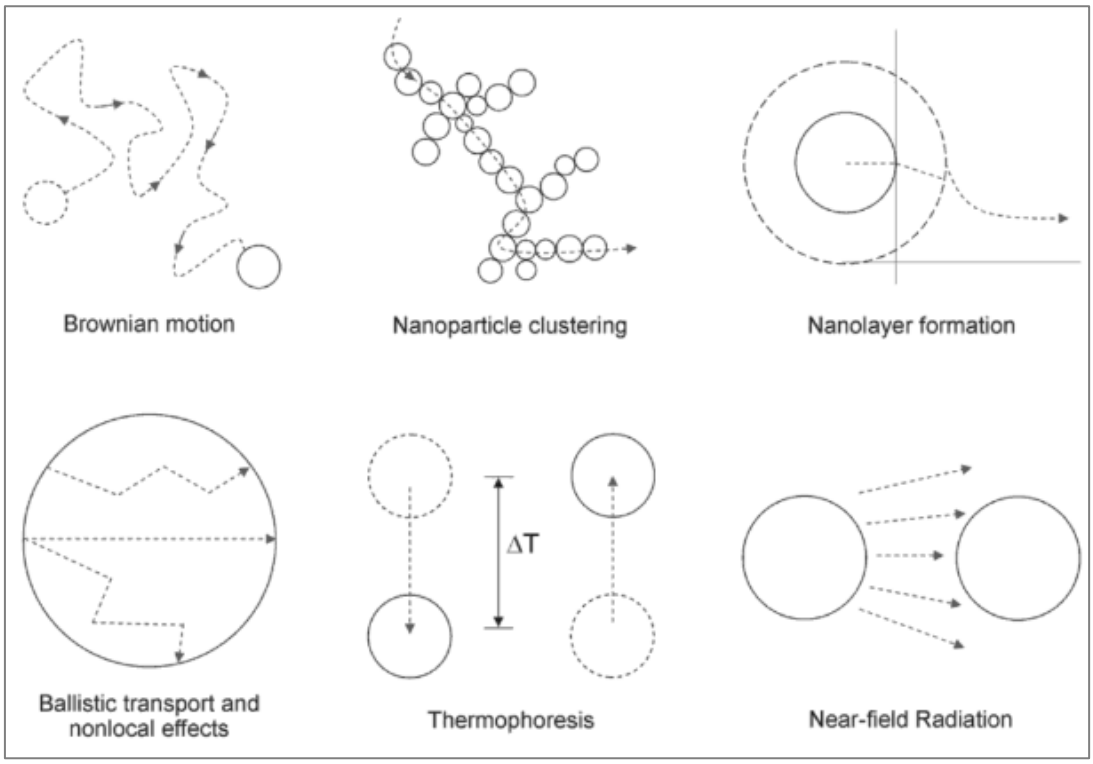

Figure 2.16: Mechanisms of heat conduction in nanofluids (Bhanvase & Barai, 2021:102-103)

As the temperature increases, the energy around particles increases, causing them to travel from the higher temperature location to the lower one and the heat transfer process increases with a decrease in the bulk density (Godson et al., 2010).

Near field radiation: may be responsible for increased thermal conductivity. According to Domingues et al. (2005), heat transfer rate between two bodies separated by a nanometric distance increases rapidly. The radiation effect, however, is always smaller than heat conduction through a medium (Wang et al., 2012). Although all of these mechanisms can model the enhancement of thermal conductivity, they may be irrelevant for some nanofluid systems, especially due to the wide range of nanomaterials that may behave distinctively with different base fluids (Wang et al., 2012). There are some parameters such as particle size, particle shape and particle concentration that affect the thermal conductivity of a nanofluid. Table 2.4 provides a summary of previous studies on the effect of dispersed Co_3O_4 nanoparticles (their particle size, shape, and concentration), as well as temperature, on the thermal conductivity of their resultant nanofluids.

- **Effect of temperature**

The thermal conductivity of nanofluids is affected by the temperature of both base fluid and the dispersed particles. Mariano et al. (2015) studied the thermal conductivity of Co_3O_4-EG nanofluids of different concentrations ranging from 0.94 to 5.67 vol% at 10, 30 and 50 °C. An increase in temperature caused the thermal conductivity of nanofluids to decrease slightly. Sekhar et al. (2017) studied the thermal conductivity of Co_3O_4-DIW nanofluids of different

volumetric concentrations from 30 to 60 °C (10 °C steps). They observed that an increase in temperature induced a 5% increase in thermal conductivity ratio, for the highest concentration (0.4 vol%). Sekhar et al. (2018) conducted a similar study from 40 to 70 °C. They reported that an increase temperature caused a 25% increase in thermal conductivity ratio. Gupta et al. (2021) measured the thermal conductivity of EG (k) and different Co_3O_4-EG nanofluids (k_{nf}) from 25-35 °C by using the Bridgman equation (2.24) and its modified form (2.25), respectively.

$$k = 3.0\left(\frac{\rho N_A}{M}\right)^{2/3} k_B U \quad \textbf{(2.24)}$$

$$k_{nf} = 3.0\left(\frac{\rho_{nf} N_A}{M_{nf}}\right)^{2/3} k_B U \quad \textbf{(2.25)}$$

Where ρ, ρ_{nf}, N_A, M, M_{nf}, k_B and U are the fluid density, nanofluid density, Avogadro number, fluid molar mass, nanofluid molar mass, Boltzmann constant and speed of sound, respectively.

They found that the thermal conductivity of Co_3O_4-EG nanofluids decreased with increasing temperature. This was attributed to the fact that the values of density and speed of sound decreased as temperature increased. According to the Bridgman equation, these values are directly related to thermal conductivity. Mitra et al. (2021) measured the thermal conductivity of rod like Co_3O_4-DIW nanofluids and flower like Co_3O_4-DIW nanofluids at 0.011 wt%. For rod like Co_3O_4-DIW nanofluids, they noted a thermal conductivity enhancement of 21% from 30 to 70 ˚C. In the case of flower like nanofluids, they reported a slight increase in thermal conductivity enhancement (3%) with increasing temperature. The higher increment in thermal conductivity enhancement of rod like Co_3O_4-DIW nanofluids was attributed to their higher aspect ratio structure (Gu et al., 2013) leading to increased contact area with the heat source hence, higher heat transfer rates (Ghosh et al., 2013). Alsboul et al. (2022) measured the thermal conductivity of Co_3O_4-DW, Co_3O_4-EG, Co_3O_4-20EG/80DW, Co_3O_4-40EG/60DW and Co_3O_4-60EG/40DW nanofluids from 20 to 60 °C (at 5 °C steps). The thermal conductivity of all nanofluids increased with increasing temperature. Manoram and Moorthy (2022) measured the thermal conductivity of two different Co_3O_4-DIW nanofluids from 30 to 70 °C. They noted a linear increase in thermal conductivity of nanofluids with temperature increase. For instance, the thermal conductivity of 0.4 vol% nanofluids were increased by 18.20% and 24.35% at 30 ˚C and 70 ˚C. Rahman Salari et al. (2022) measured the thermal conductivity of different Co_3O_4-75EG/25DW nanofluids from 25 to 65 °C (at 20 °C steps). The thermal conductivities of all nanofluids increased with increasing temperature in a nonlinear manner. This trend was due to the fact that an increment in temperature results in weakened inter-particle and inter-molecular adhesion forces, leading to an enhancement in Brownian motion. Hence, a rise in thermal conductivity of nanofluids at higher temperatures.

- **Effect of particle concentration**

According to Özerinç et al. (2010), there are numerous studies in the literature about the impact of particle concentration on the thermal conductivity of nanofluids. Mariano et al. (2015) studied the thermal conductivity of Co_3O_4-EG based nanofluids. They used a KD2 Pro thermal analyser whose principle is based on the transient hot-wire method where the thermal conductivity is obtained by plotting the temperature rise versus time. This method has been reported by other researchers (Guo et al., 2018; Xu et al., 2019) to be the most accurate method to determine the thermal conductivity of nanofluids. The thermal conductivity of Co_3O_4 nanofluids of five different concentrations ranging from 0.94 to 5.67 vol% were reported at 10, 30 and 50 °C. The thermal conductivity of Co_3O_4 nanofluids increased with increasing particle concentration. They noticed an average enhancement in thermal conductivity ratio (k_{nf}/k_0) of 27% for the highest concentration (5.67 vol%). At 30 °C, a comparison was established between experimental results of thermal conductivity with respect to particle volume concentrations and results obtained from three theoretical models. The first model is that of Maxwell (1881) who is known to be the first to have developed an equation (2.26) for estimating the thermal conductivity of colloids composed of solid spheres suspended in a fluid:

$$k_{nf} = \frac{k_p+2k_0+2(k_p-k_0)\emptyset}{k_p+2k_0-(k_p-k_0)\emptyset} k_0 \quad \textbf{(2.26)}$$

Where k_{nf}, k_p, k_0, $\emptyset$ represent the nanofluid thermal conductivity, solid particles thermal conductivity, base fluid thermal conductivity and volumetric concentration of particles.

The second model was that of Hamilton and Crosser (1962) accounting for the enhancement of thermal conductivity of dilute suspensions of particles of different shapes:

$$\frac{k_{nf}}{k_0} = \frac{k_p+(n-1)k_0+(n-1)(k_p-k_0)\emptyset}{k_p+(n-1)k_0-(k_p-k_0)\emptyset} \quad \textbf{(2.27)}$$

Where n is the empirical shape factor, which can be calculated as $n = 3/\Psi$, with Ψ representing the sphericity. This is calculated by taking the surface area of a hypothetical sphere that has the same volume as the particle, divided by its actual surface area. Turian et al. (1991) concluded that the Maxwell model accurately predicts enhancements in thermal conductivity when $k_p/k_0 \sim 1$, but its performance deteriorates as this ratio rises ($k_p/k_0 > 4$). Based on the results of their analysis, the authors concluded that a volume-averaged geometric mean of particle and base fluid thermal conductivities provides the most accurate estimates of effective thermal conductivity.

Table 2.4: Past experimental work on the thermal conductivity of Co_3O_4 nanofluids

Author (s)	Co_3O_4 particle size & shape	Base fluid	Particle concentration (wt% or vol%)	Testing method and temperature	Thermal conductivity-particle size relationship	Thermal conductivity-particle concentration relationship	Summarised results
Mariano et al. (2015)	D= 17 nm (commercial)	EG	0.94, 2.06, 3.07, 4.31 & 5.67 vol%	Transient hot wire method T= 10-50 °C	None	Maxwell model (k_{np}/k_0 ~ 1). Hamilton-Crosser model (n=3/Ψ). Turian model (k_{np}/k_0 > 4).	-k_{np}/k_0 increased by 27% with an increment in particle vol% -Increase in temperature induced a slight decrease in thermal conductivity of nanofluids -Average % deviation of experimental k_{np}/k_0 with Maxwell, Turian, and HC models deviated by 4.3%, 1.4%, and 1.4%, respectively
Sekhar et al. (2017)	D= 50 nm (commercial)	DIW	0.1, 0.2, 0.3 & 0.4 vol%	Steady state method T= 30-60 °C	None	None	k_{np}/k_0 values increased by 5% from 30 to 60 °C, for 0.4 vol%
Sekhar et al. (2018)		DIW	0.1, 0.2, 0.3 & 0.4 vol%	Steady state method T= 40-70 °C	None	None	k_{np}/k_0 values increased up to 25% from 40 to 70 °C, for 0.4 vol%
Gupta et al. (2021)	D= 25-50 nm Truncated octahedron	EG	0.2, 0.4, 0.6, 0.8 & 1.0 wt%	Bridgman equation T= 25-35 °C	None	None	-k_{nf} decreased with increasing temperature -k_{nf} increased with increasing particle wt% up to 0.4 wt%. Above 0.4 wt%, k_{nf} decreased with increasing particle wt%
Mitra et al. (2021)	Nanorods (27 nm) & nanoflowers (32 nm)	DIW	0.0005, 0.003, 0.005 & 0.011 wt%	Transient hot wire method T= 30-60 °C	None	None	-k_{np}/k_0 of rod-based nanofluids increased by 21% with an increase in temperature whereas that of flower-based nanofluids increased by 3%

Alsboul et al. (2022)	D ≤ 50 nm	DW EG 20EG/ 80DW 40EG/ 60DW 60EG/ 40DW	0.025, 0.05, 0.10, 0.20 & 0.40 vol%	Transient hot wire method T= 20-60 °C	None	Maxwell model Maxwell-Eucken model Yu and Choi model	-k_{nf}/k_0 increased with increasing temperature and particle vol% -Maxwell model fitted well with the experimental data of Co_3O_4-DW and Co_3O_4-EG nanofluids at 20 °C
Manoram and Moorthy (2022)	D = 50 nm (commercial) Spherical	DIW	0.2 & 0.4 vol%	Transient hot wire method T= 30-70 °C	None	None	-k_{np}/k_0 increased by 12.13% and 18.95% at 30 °C and 70 °C, respectively for 0.2 vol% -k_{np}/k_0 increased by 18.20% and 24.35% at 30 °C and 70 °C, respectively for 0.4 vol%
Rahman Salari et al. (2022)	D= 50 nm Cubic	25DW/75EG	0.1, 0.3 and 0.5 wt%	T= 25 to 65 °C (at 20 °C steps)	None	None	k_{nf}/k_0 increased with increasing temperature and particle wt% in a non-linear manner

They made use of the logarithmic mixing rule (Das et al., 2008:167-180) and they came up with the equation below:

$$k_{nf} = k_p^{\emptyset} k_0^{1-\emptyset} \quad \textbf{(2.28)}$$

The reference value for the thermal conductivity of Co_3O_4 nanoparticles (k_p = 16.8 W m^{-1} K^{-1}) at 300 K were obtained from the study by Sahoo et al. (2013). The Maxwell model under predicted the experimental values for the enhancement of thermal conductivity. Both Turian and Hamilton-Crosser (HC) models agreed well with experimental data, and the HC model resulted in the best estimation when Ψ= 0.61. The absolute average percent values of experimental data with Maxwell, Turian, and HC models deviated by 4.3%, 1.4%, and 1.4%, respectively.

Sekhar et al. (2017) and Sekhar et al. (2018) studied the thermal conductivity of Co_3O_4-DIW based nanofluids. They used a set up (Figure 2.17) consisting of concentric cylinders with an air gap. Concentric cylinders measure thermal conductivity based on the steady-state method. They are easier to set up, have simpler equations, and provide results that are more accurate. It has a disadvantage, however, in that it generally takes a while for equilibrium to be achieved (Yüksel, 2016). There was water (6 cm in depth) in the inner cylinder and nanofluid in the air gap. An electric heater was used to heat up the water and keep it at a constant temperature in the inner cylinder. To ensure that heat only travels downward, the concentric cylinders ends were insulated with thermal insulating material. The nanoparticles in the nanofluid transported heat rapidly from the inner to outer cylinder. Sekhar et al. (2017) reported the thermal conductivity (k_{nf}) of Co_3O_4-DIW nanofluids of four different volumetric concentrations at 30, 40, 50 and 60 °C whereas the results reported by Sekhar et al. (2018) were obtained at 40, 50, 60 and 70 °C.

Figure 2.17: Thermal conductivity set up for Co_3O_4-DI water nanofluids (Sekhar et al., 2017)

Based on the Fourier's law of heat conduction in cylindrical coordinates used by Holman (2010) to calculate the thermal conductivity (*k*), *k*-ratio values can be derived from the following equation:

$$Q = \frac{2\pi kL(\Delta T)}{\ln(r_2/r_1)} \quad \textbf{(2.29)}$$

Where Q, k, L, ΔT, r_2, r_1 represent the quantity of heat supplied (J), thermal conductivity of liquid (W/m°C), length of heat conduction (m), temperature difference (°C), radius of inner concentric wall of heater (m) and radius of outer concentric wall of heater (m), respectively. The thermal conductivity value for DIW was obtained from the study by Sengers and Watson (1986). In both studies, the addition of Co_3O_4 nanoparticles to DI water caused the thermal conductivity of the resulting nanofluids to increase. Gupta et al. (2021) calculated the thermal conductivity of EG (k) and different Co_3O_4-EG nanofluids (k_{nf}) by using the Bridgman equation (2.24) and its modified form (2.25), respectively. They noted an increase in the thermal conductivity of Co_3O_4-EG nanofluids when increasing the particle volumetric concentration up to 0.4 wt%. However, the nanofluids thermal conductivity decreased with a further increase in volumetric concentration. The initial increase in thermal conductivity was attributed to Brownian motion of nanoparticles. The trend observed beyond 0.4 wt% could be due to aggregation of Co_3O_4 nanoparticles, which reduced the augmenting effects of subsequent nanoparticle additions. Mitra et al. (2021) measured the thermal conductivity of rod like Co_3O_4-DIW nanofluids and flower like Co_3O_4-DIW nanofluids at constant weight concentration (0.011 wt%) using a KD2 Pro thermal property analyser. Both types of Co_3O_4-DIW nanofluids showed an increase in thermal conductivity with the rise in particle concentration. Alsboul et al. (2022) measured the thermal conductivity of Co_3O_4-DW, Co_3O_4-EG, Co_3O_4-20EG/80DW, Co_3O_4-40EG/60DW and Co_3O_4-60EG/40DW nanofluids using a KD2 Pro instrument in a temperature range of 20 to 60 °C (at 5 °C steps). Various volumetric concentrations ranging from 0.025 to 0.4 vol% were prepared to determine the effect of particle concentration on the effective thermal conductivity of the samples. In general, the thermal conductivity of all nanofluids increased with increasing volumetric concentration. Compared to the base fluids (DW and EG), the thermal conductivity of Co_3O_4-DW nanofluids was enhanced by 1.04% and 24.4%, whereas that of Co_3O_4-EG nanofluids was enhanced by 0.61% and 14.07%, for 0.025 vol% and 0.4 vol% at 20 °C, respectively. In the case of EG-DW mixture nanofluids, the thermal conductivity of Co_3O_4-20EG/80DW nanofluids was enhanced by 0.123% and 22.2% for 0.025 vol% and 0.4 vol% at 20 °C, respectively, compared to 20EG/80DW mixture. The thermal conductivity of Co_3O_4-40EG/60DW nanofluids was enhanced by 0.1327% and 22.3% for 0.025 vol% and 0.4 vol% at 20 °C, respectively, compared to 40EG/60DW mixture. The thermal conductivity of Co_3O_4-60EG/40DW nanofluids was enhanced by 0.017% and 20.69% for 0.025 vol% and 0.4 vol%

at 20 °C, respectively, compared to 60EG/40DW. Three models namely Maxwell (1881), Maxwell-Eucken (Levy, 1981) and Yu and Choi (2003) were used to correlate the effective thermal conductivity with respect to particle volumetric concentration of Co_3O_4-DW and Co_3O_4-EG nanofluids at 20 °C. The experimental data of Co_3O_4-DW and Co_3O_4-EG nanofluids have been found to be in good agreement with the theoretical data obtained from the Maxwell model. Manoram and Moorthy (2022) measured the thermal conductivity of Co_3O_4-DIW nanofluids of 0.2 and 0.4 vol% using a KD2 Pro thermal property analyser. At 0.2 vol%, they noted a thermal conductivity enhancement of 12.13% and 18.95% at 30 ˚C and 70˚C, respectively. The thermal conductivity values of 0.4 vol% nanofluids increased by 18.20% and 24.35% at 30 ˚C and 70 ˚C, respectively. They reported that the thermal conductivity increment was due to Brownian motion of particles. In addition, micro-convection between the nanoparticle and fluid particle also influenced the increment of thermal conductivity of nanofluids. Rahman Salari et al. (2022) measured the thermal conductivity of Co_3O_4-75EG/25DW nanofluids at various particle weight concentrations from 25 to 65 °C (at 20 °C steps) using a KD2 Pro thermal analyser. The thermal conductivities of all nanofluids were found to increase with increasing weight concentrations in a nonlinear manner. The latter trend can be attributed to a reduction in particle-particle distance when increasing particle concentration, resulting in an increase in heat transfer paths between added particles, which is known as lattice vibration frequency or percolation effect of heat transfer (Chatterjee et al., 2019).

- **Effect of particle size**

To our knowledge, no study has examined the effect of Co_3O_4 particle size on the thermal conductivity of Co_3O_4-based nanofluids, and thus, the studies of other metallic and metal oxide-based nanofluids are reviewed to understand the relationship between the particle size and the thermal conductivity of nanofluids. For instance, Chopkar et al. (2006) prepared $Al_{70}Cu_{30}$-EG nanofluids. For 0.5 vol% nanofluid, they used different particle sizes ranging from 9 to 83 nm at room temperature. They found that the thermal conductivity ratio (k_{np}/k_0) increased from 3 to 38% with a decrease in particle size. The reason for such relation between particle size and thermal conductivity of nanofluids is attributed to the increase in surface area of smaller $Al_{70}Cu_{30}$ particles hence, enhancing the heat transport inside the fluid. In another study, Chopkar et al. (2008) studied the effect of particle size on the thermal conductivity ratio of H_2O- and EG-based nanofluids with Al_2Cu and Ag_2Al nanoparticles. They varied the particle size between 30 and 120 nm. For all types of nanofluids, they noted an increase in thermal conductivity ratio with decreasing particle size. According to Özerinç et al. (2010), the increase in thermal conductivity is associated with a decrease in particle size due to Brownian motion of nanoparticles and liquid layering around nanoparticles. Moghadassi et al. (2010) measured the thermal conductivity of CuO particles dispersed in

two different fluids (paraffin or monoethylene glycol). A dispersant (oleic acid) was used to improve the stability of CuO-paraffin nanofluids while none was used for monoethylene glycol (MEG) based nanofluids. They investigated the effect of two different particle size (30 and 40 nm) on the thermal conductivity of CuO-paraffin/or MEG nanofluids. They noted an increase in the effective thermal conductivities with a decrease in particle size. This is because smaller particles exhibit higher Brownian motion hence, greater thermal conductivities. Teng et al. (2010) reported the effect of different particle sizes (20, 50 and 100 nm) on the thermal conductivity of alumina-water nanofluids at 10, 30 and 50 °C. They observed an increment in thermal conductivity ratio with a decrease in particle size. The reason for this is that smaller particles exhibit higher Brownian motion, causing them to collide more often hence resulting in a greater heat transfer.

Other researchers reported an opposing trend between particle size and thermal conductivity of nanofluids. Xie et al. (2002) investigated the effect of particle size (26 nm/spherical and 600 nm/cylindrical) on the thermal conductivity of SiC-DIW nanofluids at volume concentrations up to 4.2%. They reported an increment in thermal conductivity with increasing particle size. Chen et al. (2008a) measured the effect of different particle sizes (10-30 nm) on the thermal conductivity ratio for SiO_2/H_2O nanofluids. At the same particle volume concentration (16%), they noted the same trend. This was attributed to the smaller area of particle-liquid interface exhibited by larger particles resulting in an increase in thermal conductivity ratio (Huxtable et al., 2003; Chen et al., 2008a). Beck et al. (2009) conducted a systematic particle size dependency study for Al_2O_3/H_2O and Al_2O_3/EG nanofluids. They used a wide range of particle size between 8 and 282 nm. For the same particle volume fraction, Beck et al. (2009) noted that the enhancement in thermal conductivity ratio increased with increasing particle size, below about 50 nm. According to Beck et al. (2009), smaller particle sizes are more prone to phonon scattering which led to lower thermal conductivity. However, the study conducted by Mintsa et al. (2009) reported a completely different trend. They measured the thermal conductivity of Al_2O_3/H_2O nanofluids. They used two different sizes of Al_2O_3 nanoparticles (36 and 47 nm). They found that the thermal conductivity enhancements at room temperature were nearly identical for two different sizes of Al_2O_3 nanoparticles. This trend was due to temperature being kept constant, as increasing the temperature is generally expected to increase the effective thermal conductivity ratio with a reduction in particle size.

- **Effect of particle shape**

Mitra et al. (2021) investigated the effect of two different particle shapes (nanorods and nanoflowers) on the thermal conductivity ratio of Co_3O_4-H_2O based nanofluids. At 0.011 wt%, they reported a 21% enhancement in the thermal conductivity ratio of Co_3O_4 nanorods based nanofluids from 30 to 60 °C while nanoflower based nanofluids exhibited a 3% enhancement.

Rod-based nanofluids exhibited higher thermal conductivity due to the higher aspect ratio of nanorods (Gu et al., 2013), thereby increasing the contact area with the heat source, which resulted in higher heat transfer rates (Ghosh et al., 2013).

2.9 Conclusion

This chapter provided information on the application, structure and hydrothermal synthesis of $Co_2(OH)_3Cl$ nanoparticles. The dependence of the $Co_2(OH)_3Cl$ size and shape on their synthesis conditions, has been discussed. An in-depth discussion on the complex details related to different growth mechanisms of $Co_2(OH)_3Cl$ and Co_3O_4 has been reported. Prior literature utilized a binary triethanolamine/water solvent as template to direct the self-assembly of different $Co_2(OH)_3Cl$ nanostructures into microstructures. Further, it has been demonstrated that an increase in the propanol/water can significantly increase the size of rhombic Co_3O_4 nanoparticles. The use of a controlled propanol/water solvent to control the particle size and shape is a new approach in the synthesis of $Co_2(OH)_3Cl$ nanostructures. A comprehensive review of literature on nanofluid preparation and the influence of Co_3O_4 particle characteristics on the ensuing nanofluids has been provided. Mitra et al. (2021) reported that flower-shaped (32 nm) Co_3O_4 nanofluids were more stable than rod-shaped (27 nm) nanofluids. However, the authors did not provide an explanation for the impact of Co_3O_4 particle size and shape on the stability of their nanofluids. A reduction in particle concentration increases the particle separation distance resulting in Van der Waals attractive potential reducing hence, producing stable nanofluids. Furthermore, the addition of nanoparticles significantly enhances the properties of conventional fluids. According to the literature, the particle size, shape and concentration of Co_3O_4 affect the viscosity and thermal conductivity of the resultant nanofluids. A reduction in Co_3O_4 particle concentration causes a reduction in the internal viscous shear stress of nanofluids resulting in a decrease in the viscosity of nanofluids. However, an increase in Co_3O_4 particle concentration causes a reduction in particle-particle distance resulting in increased thermal conductivity of nanofluids. Raising the temperature weakens the interparticle/intermolecular forces between the molecules of Co_3O_4 and those of water resulting in a reduction of the viscosity of Co_3O_4-H_2O nanofluids. Increasing the temperature weakens interparticle/intermolecular adhesion forces, leading to an enhancement in Brownian motion which is responsible for the enhancement in thermal conductivity of resulting nanofluids. Conflicting trends on the effects of particle size and shape on the properties of various nanofluids have been reported in the literature. Concerning the effect of particle size on the viscosity of some nanofluids, three different trends have been reported. Some researchers reported higher viscosity for fluids containing bigger nanoparticles, while others reported higher viscosity for fluids made of smaller nanoparticles. The increased viscosity of nanofluids containing smaller particles was because of the higher surface area of smaller particles resulting in higher interfacial

resistance with the fluid layer. In contrast, other researchers found that the change in particle size did not affect the viscosity of nanofluids. About the effect of particle size on the thermal conductivity of nanofluids, the first category of researchers found that the thermal conductivity increased with decreasing particle size. Such trend is because smaller particles have an increasing surface area which increases the Brownian motion causing them to collide more often hence resulting in a greater heat transfer. In addition, the Brownian motion and liquid layering around smaller nanoparticles are the mechanisms responsible for enhanced thermal conductivity of nanofluids. The second category reported increasing thermal conductivity with increasing particle size. This trend was due to smaller particles being more prone to phonon scattering hence, leading to lower thermal conductivity. Co_3O_4 nanoparticles of higher aspect ratio were reported to have an increased contact area with the heat source, which favoured a higher thermal conductivity. Concerning the effect of particle shape on the viscosity of different nanofluids, it was found that elongated particles and agglomerates had higher viscosities because of structural limitations of rotational and translational Brownian motions. However, spherical particles and low aspect ratio spheroids displayed lower viscosities due to their ability to rotate easily. Due to lack of previous studies on the properties of $Co_2(OH)_3Cl$ nanofluids and conflicting reports on the impact of particle size and shape on the properties of various nanofluids, a systematic study of $Co_2(OH)_3Cl$ nanofluids is essential.

CHAPTER 3 RESEARCH METHODOLOGY

3.1 Introduction

A detailed description of the preparation of $Co_2(OH)_3Cl$ nanoparticles via the hydrothermal route at different synthesis conditions as well as that of their resulting nanofluids is provided. In addition, the equipment, and the characterisation techniques used in each part are presented and explained.

3.2 Research design

The experiments were divided into three sections: the hydrothermal precipitation of $Co_2(OH)_3Cl$ particles in various propanol concentrations, the time dependent hydrothermal precipitation of $Co_2(OH)_3Cl$ particles and the preparation of $Co_2(OH)_3Cl$-H_2O nanofluids. The first section involved the hydrothermal precipitation of $Co_2(OH)_3Cl$ particles, in pure water, pure propanol and various propanol to water mixtures to investigate their effect on the size and shape of particles, at constant synthesis temperature and time as illustrated in Figure 3.1. $CoCl_2.6H_2O$ was selected as the base salt for these experiments. Ammonium hydroxide (NH_4OH) was selected as the precipitating agent. Propanol was selected as alcohol and used at varying ratios (%v/v) ranging from 10 to 98%. The second section includes the hydrothermal precipitation of $Co_2(OH)_3Cl$ particles at different synthesis times to study their growth kinetics, at constant propanol concentration and synthesis temperature as presented in Figure 3.2. In the last section, the preparation of aqueous $Co_2(OH)_3Cl$ nanofluids was carried out by dispersing $Co_2(OH)_3Cl$ nanoparticles of different particle sizes and shapes in pure water at constant particle weight concentration as presented in Figure 3.1. Then, the properties (viscosity and thermal conductivity) of stable $Co_2(OH)_3Cl$-H_2O nanofluids were measured.

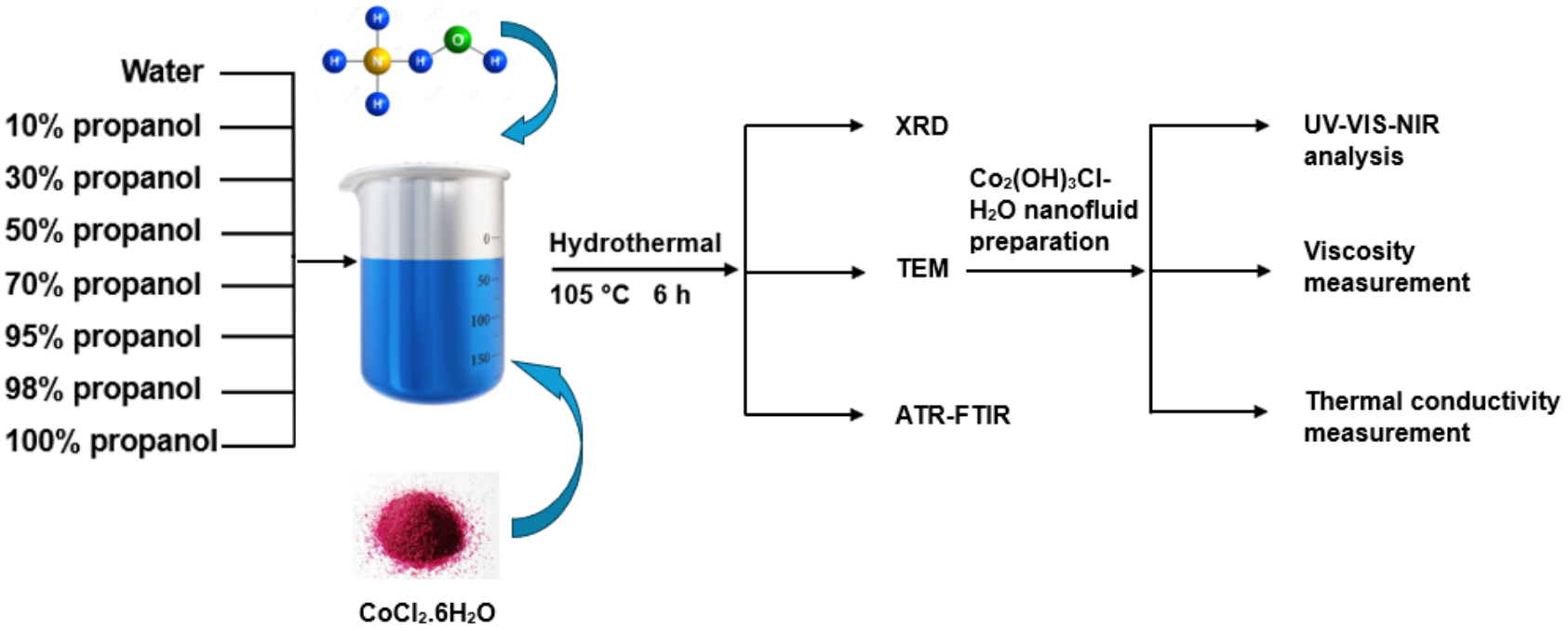

Figure 3.1: Overview of $Co_2(OH)_3Cl$ hydrothermal synthesis, preparation and characterisation of their aqueous nanofluids

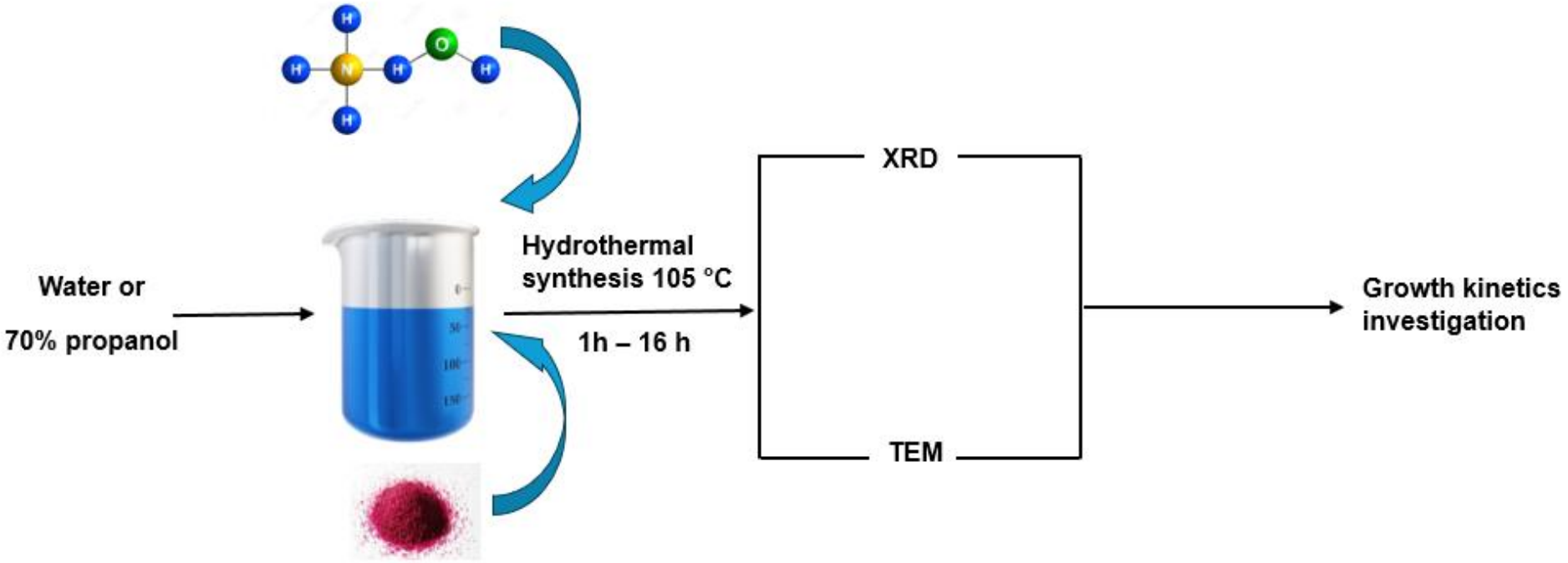

Figure 3.2: Overview of $Co_2(OH)_3Cl$ growth kinetics study in water and 70% propanol, respectively

3.3 Experimental methods

This section describes in detail the methods used for the synthesis of $Co_2(OH)_3Cl$ nanoparticles, the preparation of $Co_2(OH)_3Cl$-H_2O nanofluids as well as for the measurement of their properties. The experiments described in sections 3.3.1, 3.3.2 and 3.3.3 were completed in the Chemical Engineering laboratory Room 1.27 at the CPUT Bellville campus.

3.3.1 $Co_2(OH)_3Cl$ hydrothermal precipitation at different propanol concentrations

There was no further purification of the analytical grade chemicals used. For these experiments, a molarity of 0.23 M was maintained for $CoCl_2.6H_2O$ (Associated Chemical Enterprises). An amount of 32.8 g of $CoCl_2.6H_2O$ was dissolved in propanol-water mixtures at different ratios. Table 3.1 provides the propanol to water ratios used in the experiments. Once dissolved, the solution pH was adjusted to ±8.10 by adding NH_4OH solution dropwise. An amount of 600 mL of the resulting mixture was then poured into the 0.99 L Teflon-lined pressure reactor fitted with a thermocouple and a self-regulating heating jacket, as shown in Figure 3.3.

Table 3.1: Experiments at different propanol concentrations

Propanol to water ratio (%v/v)	Temperature (°C)	Time (h)
0	105	6
10		
30		
50		
70		
95		
98		
100		

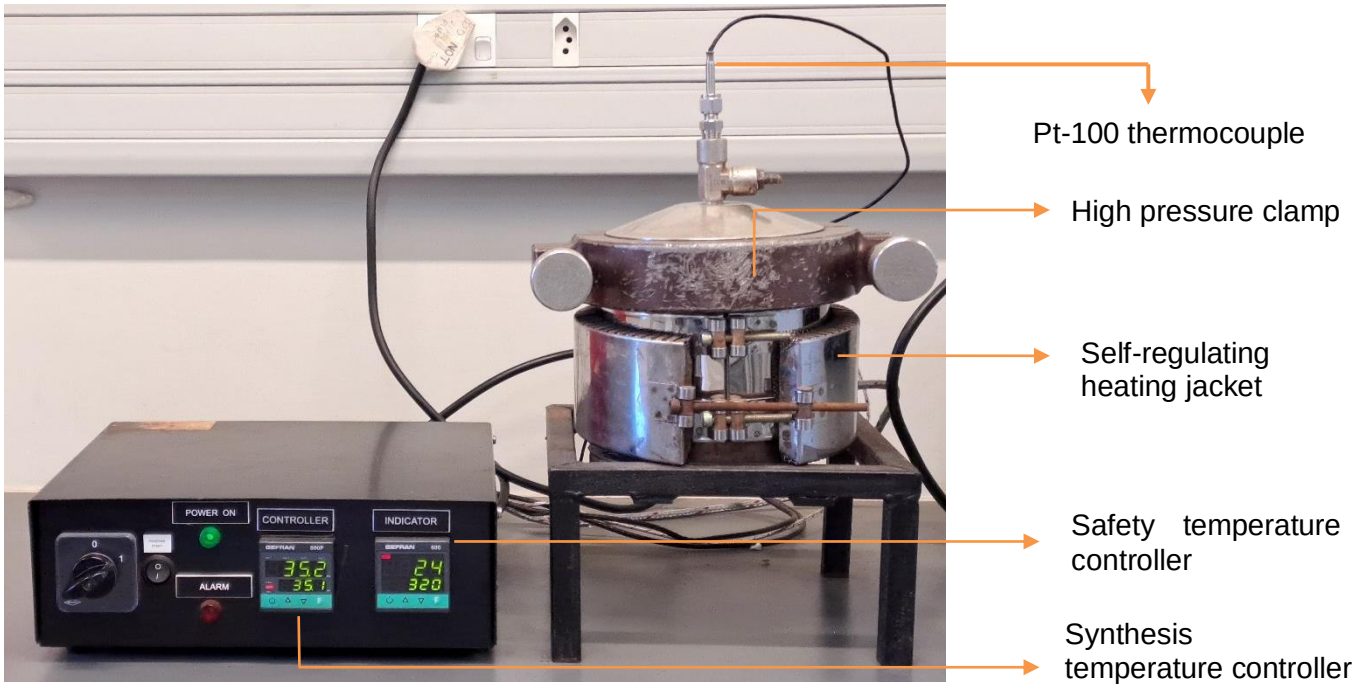

Figure 3.3: Hydrothermal pressure reactor with temperature controller

The synthesis was maintained at 105±5 °C for 6 h. After the reaction was completed, the reaction vessel was allowed to cool naturally, followed by the decantation of the supernatant liquid, centrifugation, multiple rinses of the sample with water, final rinse with ethanol to remove impurities, and drying in an oven overnight at 60 °C to remove the remaining moisture.

3.3.2 $Co_2(OH)_3Cl$ hydrothermal precipitation at different synthesis times

For these experiments, 0.23 M solutions of $CoCl_2.6H_2O$ dissolved in either pure water or 70% propanol concentration were prepared. The pH of each solution was also adjusted to ±8.10 through the addition of NH_4OH solution dropwise. As before, 600 mL of the resulting mixture was then poured into the pressure reactor (Figure 3.3). A synthesis temperature of 105±5 °C was maintained for 6 h however, other synthesis times were used to investigate their effect on the growth of particles. As soon as the reaction was complete, each sample was decanted, centrifuged, washed with water multiple times, followed by a final rinse with ethanol to remove impurities, and dried in an oven overnight at 60 °C to remove any remaining water. Table 3.2 summarizes the experimental design.

Table 3.2: Experiments at different reaction times

Solvent	Temperature (°C)	Time (min)
Water	105	60
		180
		360
		540
		720
		960
Propanol/water 70/30 (%v/v)	105	60
		180
		360
		540
		720
		960

3.3.3 Preparation of $Co_2(OH)_3Cl$ nanofluids

The $Co_2(OH)_3Cl$-H_2O nanofluids used in this work were derived from $Co_2(OH)_3Cl$ nanoparticles synthesised in various propanol concentrations ranging from 0 to 100%. Nanoparticle concentration of 0.03 wt% was selected to prepare $Co_2(OH)_3Cl$ nanofluid samples via a simple two step method as explained in Figure 3.4. Deionised water supplied from the Chemistry laboratory was used as base fluid. To prepare 250 mL of $Co_2(OH)_3Cl$-H_2O nanofluid at a particle weight concentration of 0.03 wt%, 0.075 g of $Co_2(OH)_3Cl$ nanopowder was weighed and dispersed in DIW. The weight concentration of $Co_2(OH)_3Cl$ nanofluids was calculated from the weight of $Co_2(OH)_3Cl$ nanopowder and the total weight of the suspension as reported by Li et al. (2015).

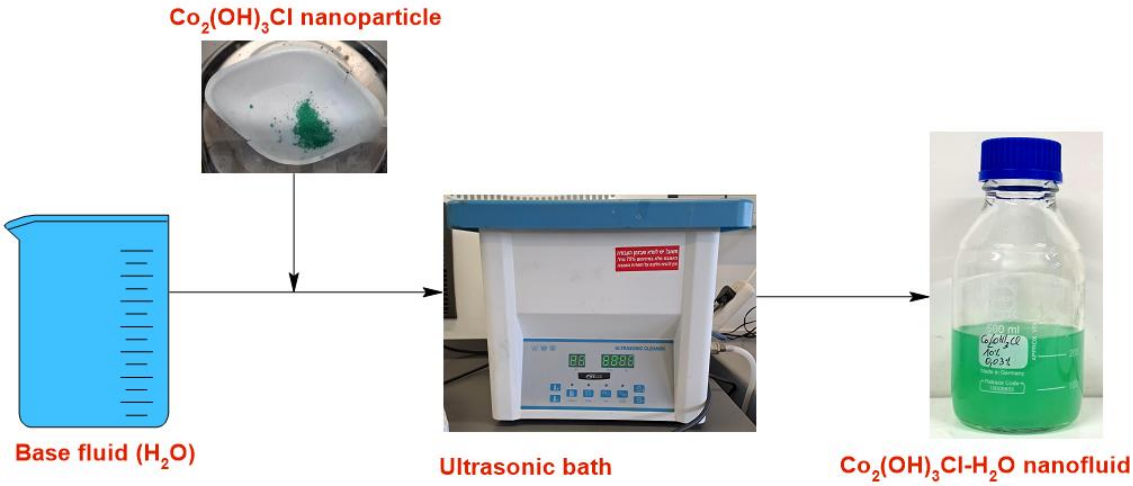

Figure 3.4: Illustration of $Co_2(OH)_3Cl$-H_2O nanofluid preparation

Then, the mixture was sonicated for 4 h in a 10 L ultrasonic bath (MRC, clean 02, power: 240 W) at a frequency of 40 kHz, which helped in homogenously distributing the nanopowder in the base fluid. No surfactant was used to prepare the nanofluids. After 4 hours of sonication, no sedimentation was observed in $Co_2(OH)_3Cl$-H_2O nanofluids as shown in Figure 3.5. In all cases, the nanofluids remained stable for a maximum of 24 h until some sediments were observed as shown in Figure 3.6.

Figure 3.5: $Co_2(OH)_3Cl$-H_2O nanofluids produced from different propanol concentrations at 0.03 wt% after 4 h of sonication

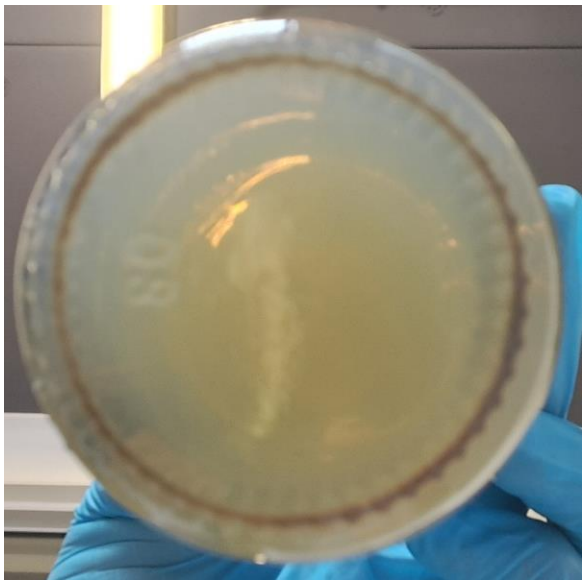

Figure 3.6: Sedimentation in $Co_2(OH)_3Cl$-H_2O nanofluid beyond 24 h of visual observation

3.4 Characterisation methods

This section presents the characterisation methods used to determine the phase, shape, particle size distribution (PSD) and size of synthesised $Co_2(OH)_3Cl$ nanopowders (see

sections 3.3.1 & 3.3.2). The nanoparticles were sampled for analysis after hydrothermal precipitation in different propanol concentrations and at different synthesis times. PSD, size and shape of nanoparticles were determined from transmission electron microscopy (TEM), which were performed at the Centre for Nanostructures and Advanced Materials (CSIR) and the Electron Microscopy Unit (EMU) located at the University of Cape Town (UCT). The composition, phase and degree of crystallinity were further determined using X-Ray Diffraction (XRD) analysis performed at CSIR and the XRD & Thermal Laboratory located at Stellenbosch University. Attenuated Total Reflectance-Fourier Transform Infrared (ATR-FTIR) spectroscopy and UV-VIS-NIR analysis were conducted on selected $Co_2(OH)_3Cl$ nanopowders to identify their functional groups and determine their ability in transmitting light. Both analyses were carried out at the CPUT Bellville campus. To investigate the thermophysical properties of the prepared $Co_2(OH)_3Cl$-H_2O nanofluids, viscosity measurements were performed at the flow process and rheology centre (FPRC), on the CPUT District six campus, while the thermal conductivity measurements were carried out at the department of Mechanical and Mechatronic Engineering, CPUT Bellville campus.

3.4.1 X-ray Diffraction

XRD is a reliable technique used for the identification of a crystalline material, by using a diffractometer. XRD is based on the interference of monochromatic X-rays with the randomly oriented planes of the powdered crystalline sample as shown in Figure 3.7. Diffracted waves, which satisfy Bragg's law (see Figure 3.7), form patterns and can be detected using a movable detector (West, 2022).

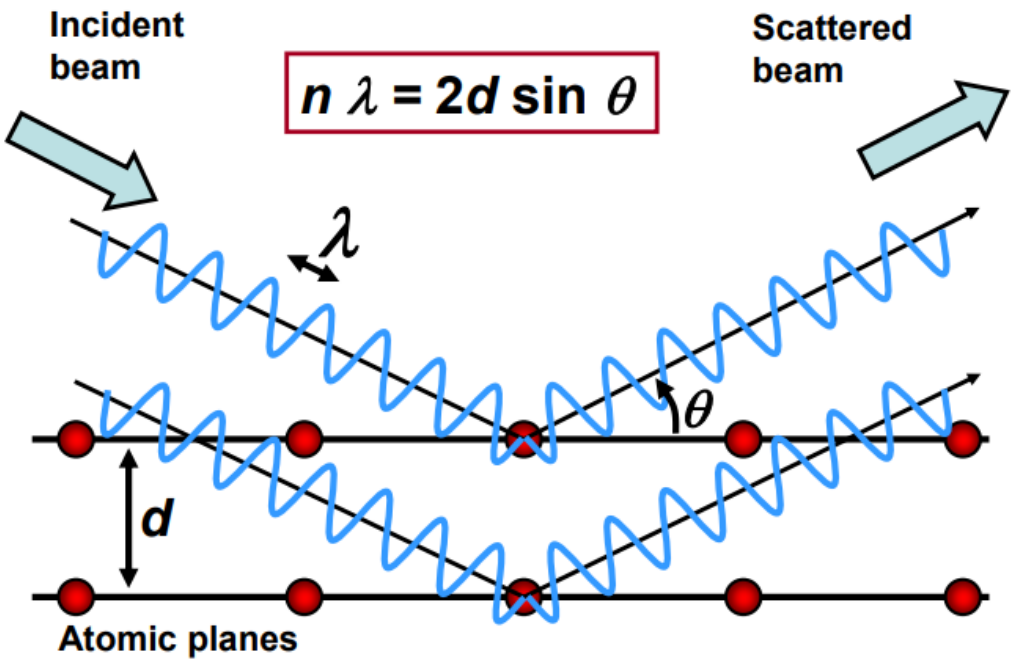

Figure 3.7: X-ray diffraction principle (West, 2022)

XRD is used to identify the phase structure, phase composition of an unknown material by comparing its diffraction pattern with the standard pattern provided from the International Centre for Diffraction Data (ICDD) database.

3.4.2 Transmission Electron Microscopy

TEM is a technique that provides information about the internal composition of a sample using an electron beam. TEM involves transmitting a high voltage electron beam from a tungsten filament through an extremely thin sample supported by a copper grid as illustrated in Figure 3.8. Scattered electrons are focused by a sequence of lens into an image on a fluorescent screen (Kumar et al., 2019).

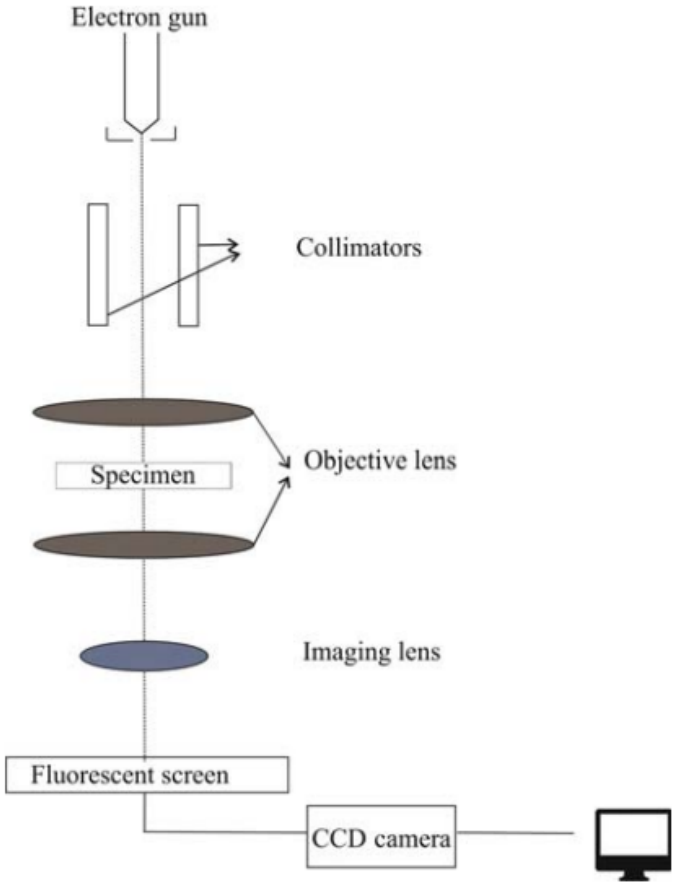

Figure 3.8: Working principle of TEM (Kumar et al., 2019)

The PSD and size of each sample were determined from the TEM images of samples by using ImageJ software for measuring 200 individual nanoparticles. The PSD were expressed using a log-normal function, characterized by the mean and the standard deviation (Pyrz & Buttrey, 2008).

3.4.3 Attenuated Total Reflectance-Fourier Transform Infrared spectroscopy

FTIR is a technique utilized for identifying the functional groups in materials (gases, liquids, and solids) by using the beam of infrared radiation. An infrared spectrometer measures the absorption of IR radiation made by each bond in the sample molecule and generates an infrared spectrum which is a plot of infrared light intensity (%transmittance or %absorbance) versus energy range expressed in wavenumber (cm^{-1}). For FTIR analysis, samples are prepared via KBr pellets and liquid cells methods. Due to the disadvantages associated with these methods, FTIR measurements are largely achieved in ATR mode because of its simplicity as compared to conventional methods. In ATR mode, as shown in Figure 3.9, an infrared beam is directed through an infrared transparent medium with a higher refractive index then towards a sample with a lower refractive index. When the ATR measurement is

completed, the absorption spectra is obtained (Liu & Kazarian, 2022). ATR-FTIR is quick and does not require major sample preparation.

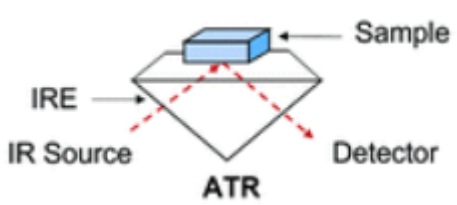

Figure 3.9: ATR-FTIR principle (Liu & Kazarian, 2022)

3.4.4 UV-VIS-NIR analysis

UV-VIS-NIR spectroscopy is an analytical technique which determines the optical properties (transmittance, reflectance and absorbance) of liquid and solid materials. The UV-VIS-NIR spectrophotometer uses ultraviolet, visible as well as near infrared radiations during the measurements. The interaction of these radiations with the material is recorded using a detector in the form of transmitted light (Figure 3.10).

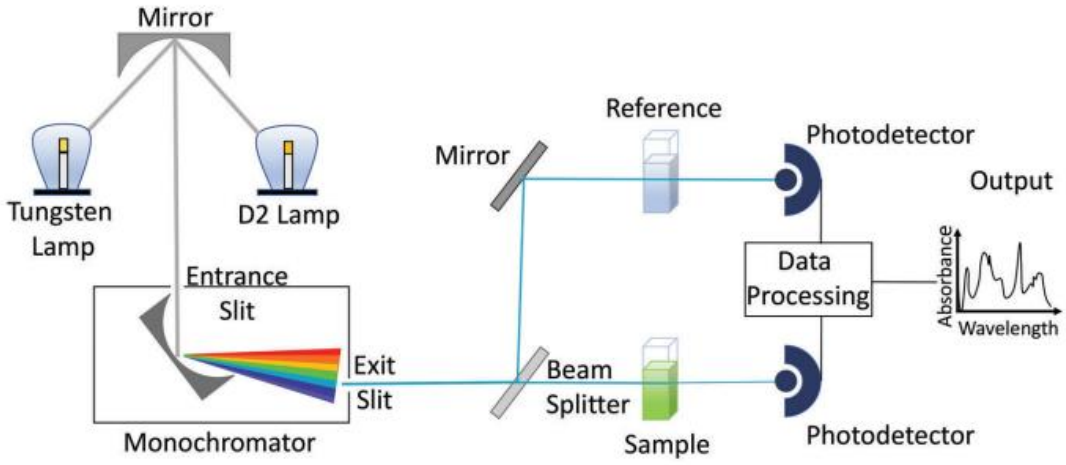

Figure 3.10: Schematic illustration of UV-VIS-NIR spectrophotometer (Rocha et al., 2018)

The optical analysis of the $Co_2(OH)_3Cl$-water nanofluids was studied using a GBC Cintra 2020 UV-VIS-NIR spectrometer.

3.4.5 Viscosity measurement

The viscosity of $Co_2(OH)_3Cl$ nanoparticles dispersed in pure water was measured using the stress controlled rotational rheometer MCR-301 (Anton Paar). A rotational rheometer is

composed of a cup containing the sample and a stationary bob located in the middle. It measures the torque produced by applying a specific angular velocity to a liquid sample of known volume over a specified time period (Malik et al., 2010). The cup is mounted on a lathe which is able to rotate, resulting in a shear rate between the cup and bob and the bob is subject to a shear stress. Figure 3.11 illustrates the set-up of a rotational rheometer with a concentric cylinder configuration.

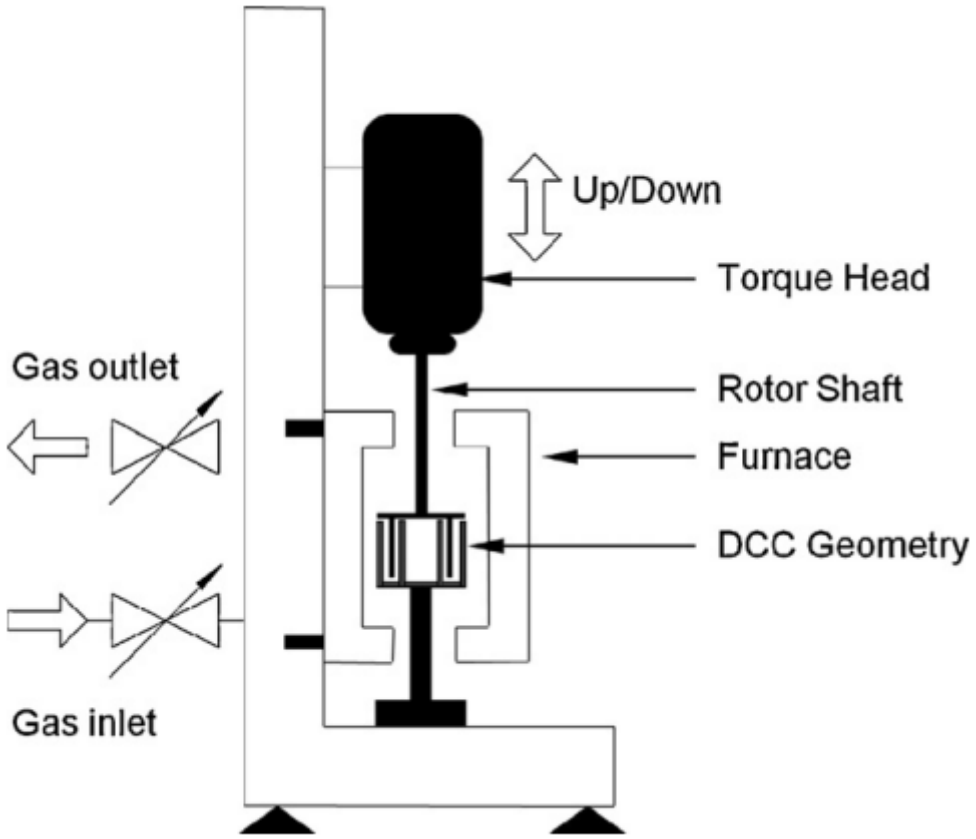

Figure 3.11: Schematic of a rotational rheometer with double concentric cylinder configuration (Malik et al., 2010)

Due to the strong tendency to flow of the samples, a cup and bob configuration (bob with conical tip in a coaxial cylinder) with a sandblasted bob surface was used in this study. The diameter of the bob and cup were 26.62 mm and 28.92 mm, and the temperature was controlled by a Peltier temperature control device. A volume of ~20 mL of the suspension was poured in the sample holder. The effect of $Co_2(OH)_3Cl$ particle size on the nanofluid viscosity was investigated by measuring the viscosity of 0.03 wt% $Co_2(OH)_3Cl$-H_2O nanofluids prepared by dispersing $Co_2(OH)_3Cl$ nanopowders obtained from different propanol concentrations in water. The dependence of viscosity on the shear rate have been studied

under the shear rate controlled measurements for low values of shear rate (60–100 s^{-1}). The viscosity was measured at temperatures ranging from 298 to 308 K.

3.4.6 Thermal conductivity measurement

The thermal conductivity of $Co_2(OH)_3Cl$-water nanofluids was measured using a homemade cylindrical cell based on the steady-state method (Kurt & Kayfeci, 2009). Figure 3.12 shows the schematic diagram of the experimental equipment. During the experiment, heat flows radially from the inner hot cylinder to the external cold cylinder through the annular space filled with the testing sample ($Co_2(OH)_3Cl$ nanofluid). The inner cylinder was heated and maintained at the desired temperature (T_h) using an electrical heater. In order to change the hot temperature, the electric power applied to the heater was varied using a DC power source, the heater resistance was powered with a current that was adjusted with 0.1% stability. The ambient temperature surrounding the cold cylinder (T_c) was varied by an external flow of heating/cooling water originating from a water bath. Heat loss during the measurement was prevented by insulating the cylindrical cell sides. Calibrated K-type (Copper/Constantan) thermocouples were positioned at the outer surfaces of the internal and external cylinders to measure the hot (T_h) and cold (T_c) temperatures, respectively. The temperature sensors have an accuracy of ±0.5 °C or ± 0.4%. The instruments were connected to a Keithley 3706 data acquisition system. The thermal conductivity of nanofluid (k_{nf}) was obtained from the one-dimensional Fourier's equation of heat conduction (Kurt & Kayfeci, 2009):

$$k_{nf} = \frac{Q\ d}{A\ (T_h - T_c)} \quad \textbf{(3.1)}$$

Where Q is the heat flux rate (W) which is equal to the electric power calculated from the measurement of the current (I) and voltage (V) injected in the hot cylinder, A is the lateral area (m^2) of the hot cylinder, T_h is the inner cylinder temperature, T_c is the outer cylinder temperature and d is the nanofluid thickness (m) between the two cylinders.

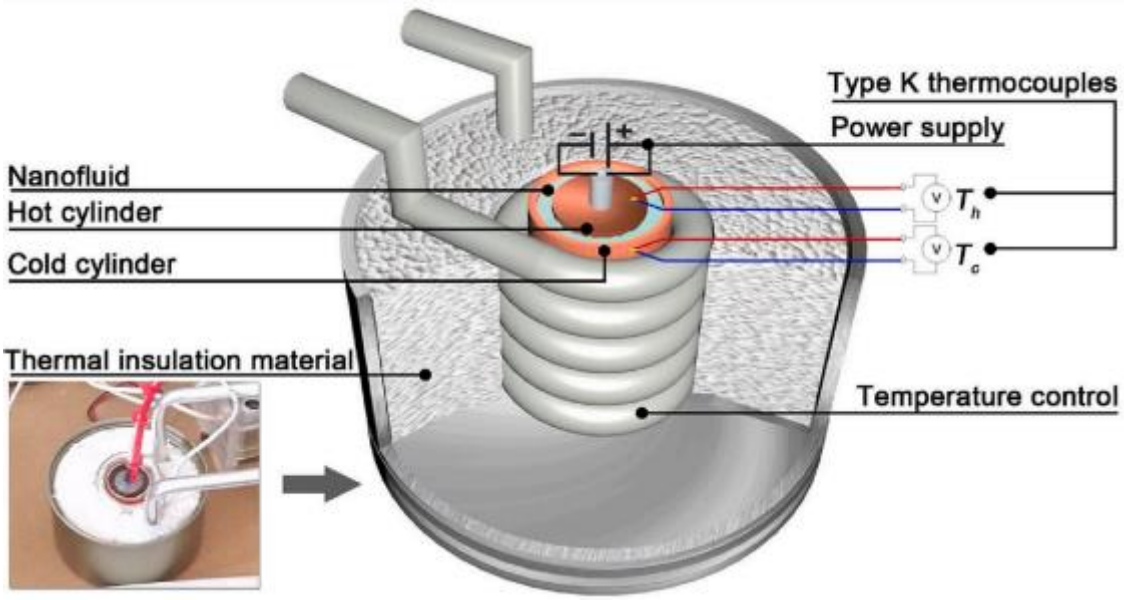

Figure 3.12: Thermal conductivity measuring system for $Co_2(OH)_3Cl$ nanofluids (Khamlich et al., 2023)

The experimental apparatus was calibrated by measuring the thermal conductivity of deionised water and the maximum deviation from the reference values was around 2.7%. To investigate the effect of $Co_2(OH)_3Cl$ particle size on the nanofluid thermal conductivity, the thermal conductivity of 0.03 wt% $Co_2(OH)_3Cl$-H_2O nanofluids prepared from $Co_2(OH)_3Cl$ nanopowders synthesised at different propanol concentrations was measured at temperatures ranging from 298 to 308 K.

CHAPTER 4 EFFECTS OF PROPANOL ON THE CHARACTERISTICS AND GROWTH KINETICS OF $Co_2(OH)_3Cl$ NANOPARTICLES

4.1 Introduction

This chapter explores the impact that different concentrations of propanol, ranging from 0 to 100%, have on the phase, morphology, and growth kinetics of $Co_2(OH)_3Cl$ nanoparticles.

4.2 Effect of propanol concentration on $Co_2(OH)_3Cl$ nanopowders characteristics

A change in the propanol-to-water ratio can significantly affect the phase and purity of cobalt hydroxy chloride particles. Figure 4.1 shows the XRD profiles of all samples at varying propanol concentrations. The XRD patterns of all the samples obtained from different propanol concentrations (Figure 4.1), revealed some diffraction peaks which matched well with the standard data of the rhombohedral $Co_2(OH)_3Cl$ (JCPDS card no. 73-2134). The Bragg's reflections were observed at about 2θ values of 16.2°, 32.4°, 39.6°, 49.8°, 53.5° and 59.8°, which are assigned to the crystal planes of (101), (113), (024), (033), (220) and (208), respectively which were similar to the findings of various researchers (Mansournia & Rakhshan, 2017; Ranganatha et al., 2017; Ma et al., 2021). No other peaks were detected for the $Co_2(OH)_3Cl$ nanopowders obtained at 70% and 100% propanol concentrations indicating their purity. Ma et al. (2021) reported the preparation of $Co_2(OH)_3Cl$ from the precipitation of $CoCl_2.6H_2O$ by propylene oxide in ethanol-water mixture. It was observed that dissolved $CoCl_2.6H_2O$ exists as the aqueous complex $[Co(H_2O)_6]^{2+}$, a proton-supply acid, while propylene oxide acts as a proton-consuming base (Cui et al., 2009; Ma et al., 2021). Due to its low acidity, the complex $[Co(H_2O)_6]^{2+}$ hardly hydrolyses, leading to Cl^- coordination in the lattice of crystallized species to form $Co_2(OH)_3Cl$ (Cui et al., 2009; Ma et al., 2021). It is believed that $Co_2(OH)_3Cl$ produced in this study resulted from a mechanism similar to that described above, though another type of solvent and precipitating agent were used during synthesis.

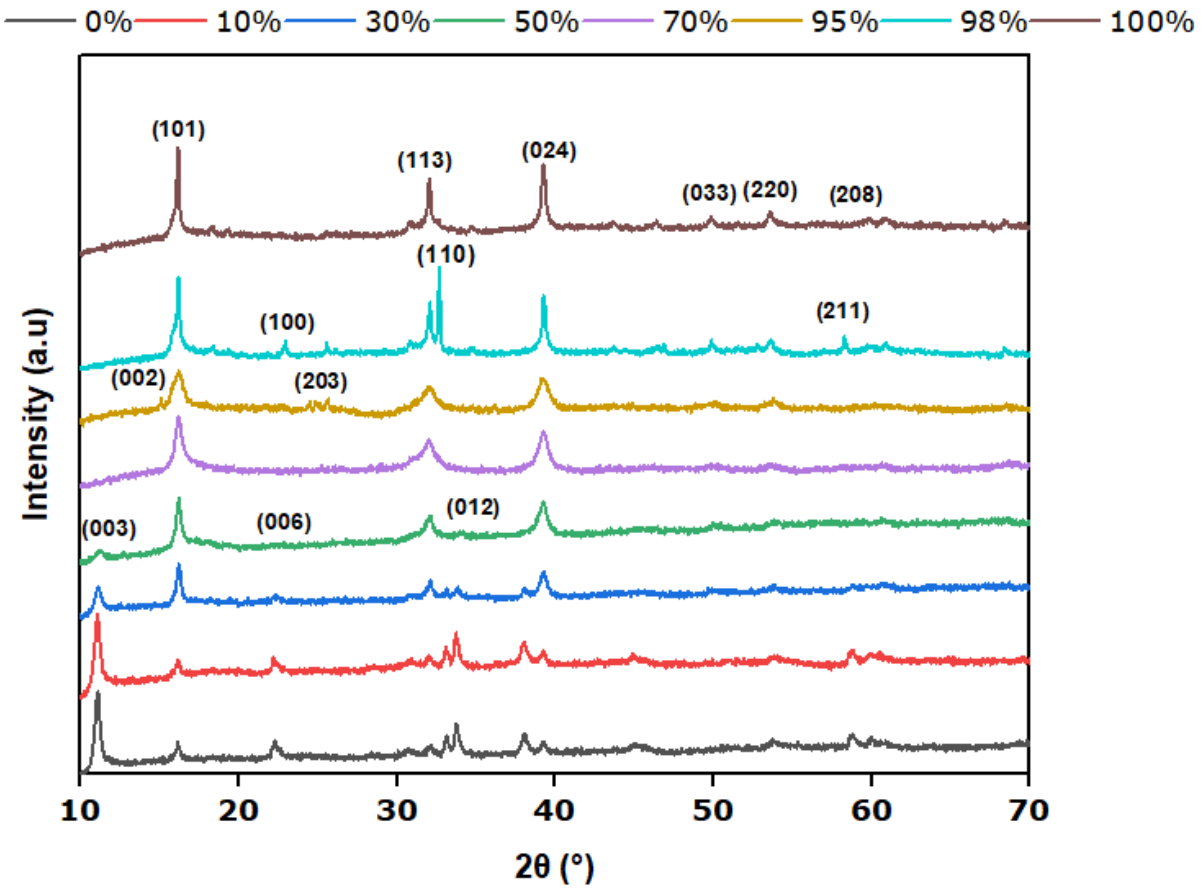

Figure 4.1: XRD patterns of all samples at different propanol concentrations

Other peaks were detected for the nanopowders prepared from 0 to 50% propanol concentrations which were assigned to the data of $Co_{1.176}(OH)_2Cl_{0.348}(H_2O)_{0.456}$ as reported by Ma et al. (2006). They exhibited peaks at about 2θ values of 11.1°, 22.3° and 33.8°, which were assigned to the crystal planes of (003), (006) and (012), respectively. The presence of $Co_{1.176}(O\ H)_2Cl_{0.348}(H_2O)_{0.456}$ can be attributed to the excess of water molecules.

The 95% and 98% propanol concentrations revealed minor peaks which were assigned to the data of cobalt ammine chloride (JCPDS card no. 70-0787) and salammoniac (JCPDS card no. 07-0007), respectively as reported in previous works (Zhao et al., 2007; Zhang et al., 2014). These peaks could be attributed to the presence of residues of the precipitating agent (NH_4OH) in the samples after synthesis. In the case of nanopowders from 95% propanol concentration, the observed peaks at about 15.1° and 25.5° correspond to the crystal planes of (002) and (203), respectively. The products from 98% propanol concentration exhibited peaks at about 22.9°, 32.7° and 58.3° that were assigned to the crystal planes of (100), (110) and (211), respectively. It can be observed from Figure 4.1 that the characteristic peaks of $Co_{1.176}(OH)_2Cl_{0.348}(H_2O)_{0.456}$ phase peaks decreased with

increasing propanol concentration from 0 to 50% and eventually disappeared. This indicates that propanol concentration influences $Co_2(OH)_3Cl$ nanoparticle purity.

The $Co_2(OH)_3Cl$ nanoparticles produced were tested for purity using ATR-FTIR analysis. ATR-FTIR spectra of $Co_2(OH)_3Cl$ nanoparticles were collected in the range 4000–400 cm^{-1}. In Figure 4.2, the ATR-FTIR spectra of as-prepared $Co_2(OH)_3Cl$ nanopowders show a narrow peak located at about 3552 cm^{-1}, which is attributed to the stretching vibration of O-H as observed in previous experimental works (Mansournia & Rakhshan, 2017; Ma et al., 2021). The presence of O-H stretching vibration results from the chemical structure of $Co_2(OH)_3Cl$ where three separate OH^- group donors are connected with one proton acceptor Cl^- via trimeric or threefold hydrogen bonds (Liu et al., 2011; Ma et al., 2021). Additionally, the Co-O stretching vibrations appeared at about 837 and 727 cm^{-1} as reported previously (Mansournia & Rakhshan, 2017). The presence of Co-O stretching vibration is due to the crystal structure of $Co_2(OH)_3Cl$ where every OH group join with three Co^{2+} ions, but has two kinds of Co–O distances: d (Co^K –O) = 2.078 Å and d (Co^T –O) = 2.106 Å and this indicates that all oxygen ions are strongly bonded to their nearest-neighbour cobalt ions (Zenmyo & Tokita, 2009; Liu et al., 2011; Ma et al., 2021).

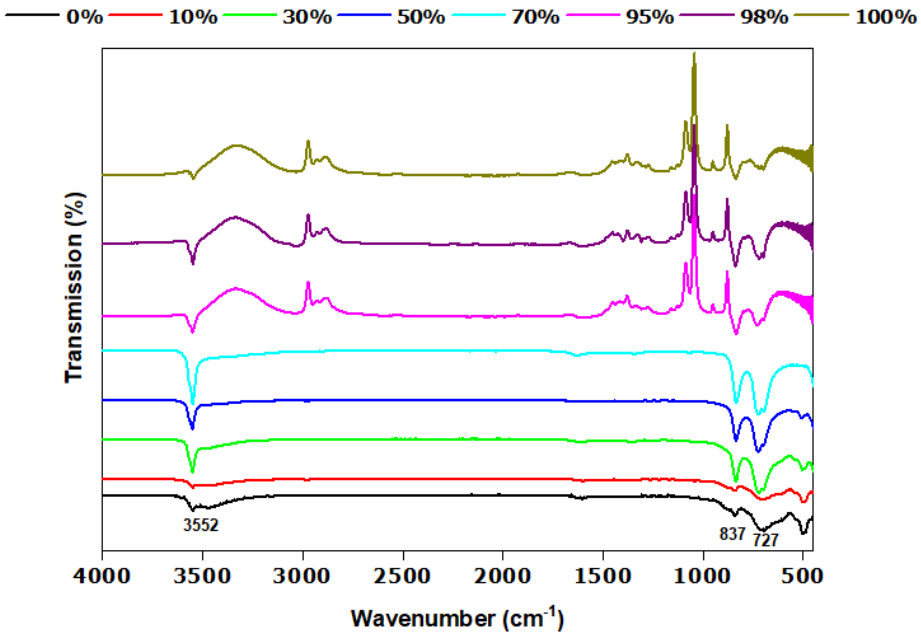

Figure 4.2: ATR-FTIR spectra of $Co_2(OH)_3Cl$ nanoparticles prepared at different propanol concentrations

The evolution of nanoparticles shape with respect to variation in propanol concentration is shown in Figure 4.3. In the absence of propanol, hexagonal $Co_2(OH)_3Cl$ nanoplates (Figure 4.3a) were formed. The same shape (Figure 4.3b) was also obtained in the case of 10%

propanol concentration. Aggregated nanoplates (Figures 4.3c & d) were obtained, however, in the case of 30% and 50% propanol concentrations. At 70% propanol concentration, the nanoplates lost their hexagonal shape which resulted in sphere like particles as well as irregular aggregated particles as shown in Figure 4.3e. Further aggregation of spherical β-$Co_2(OH)_3Cl$ particles was observed in 95% propanol concentration (Figure 4.3f). In addition to irregular aggregated particles, smaller spherical particles grew in 98 and 100% propanol concentrations (Figures 4.3g & 4.3h). Monodispersed particles were obtained at 98 and 100% propanol, compared to spherical particles at 95%. It is evident that $Co_2(OH)_3Cl$ hexagonal nanoplates were produced only at 0%, 10%, 30% and 50% propanol concentrations.

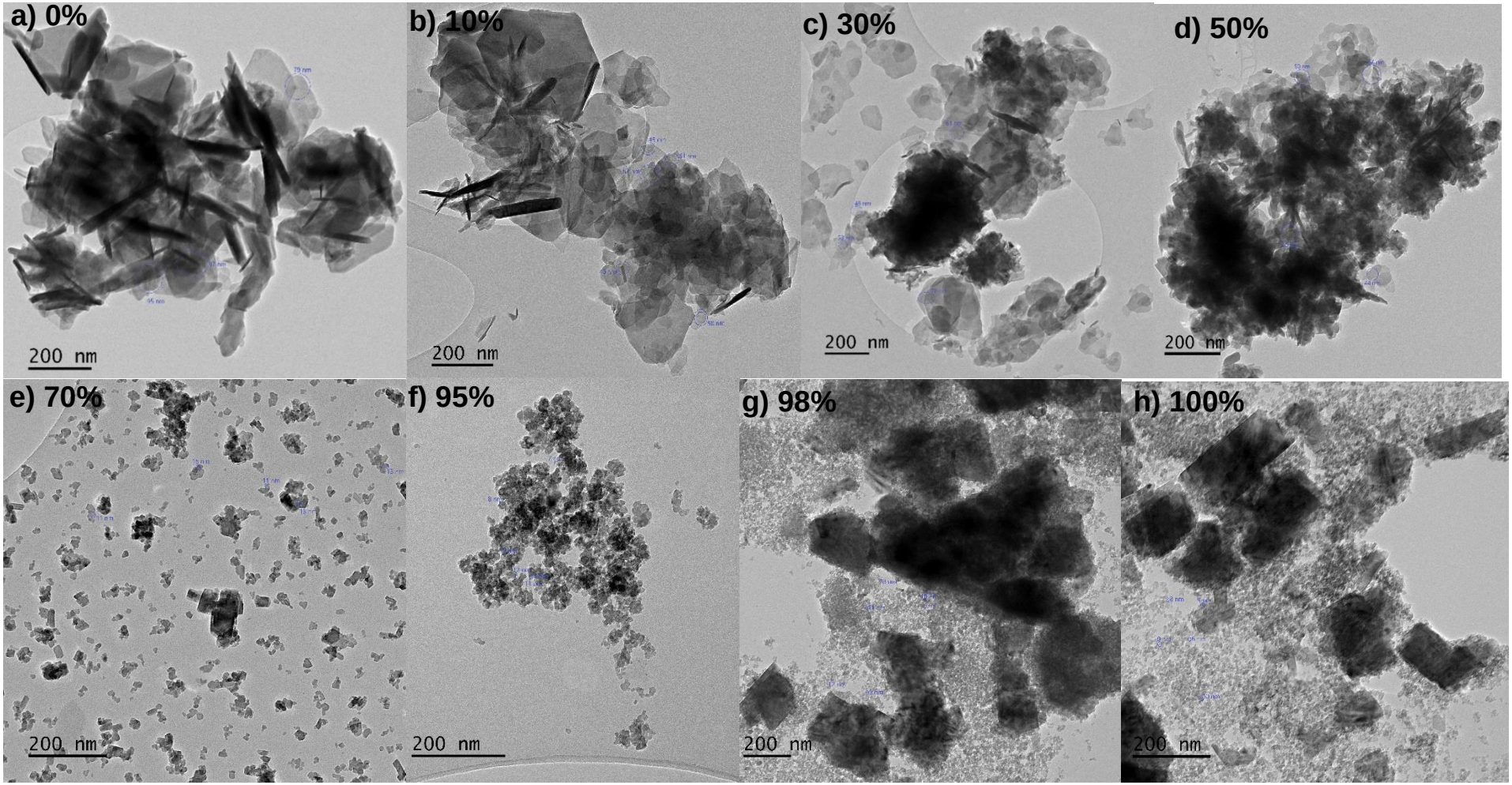

Figure 4.3: TEM images of $Co_2(OH)_3Cl$ nanoparticles synthesised from different propanol concentrations

Previous studies reported similar shapes of $Co_2(OH)_3Cl$ from the dissolution of $CoCl_2$ or $CoCl_2.6H_2O$ in aqueous or ethanol-water in the presence of NaOH or propylene oxide, respectively (Meng & Deng, 2017; Ma et al., 2021). According to Zhao et al. (2007), $Co_2(OH)_3Cl$ is a solid solution of $Co(OH)_2$ and $CoCl_2$. It has been reported that hexagonal plate-like particles often form from layered structured $Co(OH)_2$ (Aghazadeh et al., 2014). Accordingly, the $Co(OH)_2$ layered structure should have contributed to the formation of $Co_2(OH)_3Cl$ hexagonal nanoplates reported in this study. The formation of spherical $Co_2(OH)_3Cl$ particles was observed from 70% propanol concentration. This shows that an increment in propanol concentration favoured the production of spherical $Co_2(OH)_3Cl$ particles. It should be noted that water facilitates the nucleation and growth of $Co_2(OH)_3Cl$ hexagonal nanoplates whereas in the presence of pure propanol only spherical $Co_2(OH)_3Cl$ particles are visible, as shown in the TEM images. A particle size analysis was performed on each sample by counting 200 particles using the Feret diameter tool of the ImageJ software. Due to the type of images obtained, only 35 particles could be counted for nanopowders obtained from 0%, 10%, 30%, and 50% propanol concentrations. Since the norm is to count at least 200 particles for particle size distribution, it was imperative to assess the validity of using only 35 particles for particle size distribution. For the evaluation, 35 particles were selected at random for the $Co_2(OH)_3Cl$ particles from 70%, 95%, 98% and 100% propanol concentration. The average and standard deviation of 35 particles samples were determined and compared with those obtained from the 200 particles initially measured. Based on the averages obtained from counting 35 particles, and 200 particles for the same samples, respectively, the differences were 13% for 70% $Co_2(OH)_3Cl$, 16% for 95% $Co_2(OH)_3Cl$, 2% for 98% $Co_2(OH)_3Cl$, and 2% for 100% $Co_2(OH)_3Cl$. Considering these slight variations, the results for the 35 particles from 0%, 10%, 30% and 50% propanol concentration are presented as representative under the circumstances. Therefore, 35 particles have been counted from each sample to determine the average diameter of $Co_2(OH)_3Cl$ nanoparticles. The size distribution of both hexagonal plate and sphere like $Co_2(OH)_3Cl$ particles were determined by specifically measuring the Feret particle diameter using the ImageJ program for each batch of images. Figure 4.4 shows the size distribution curves of $Co_2(OH)_3Cl$ nanoparticles with respect to propanol concentration. The produced $Co_2(OH)_3Cl$ nanoparticles at propanol concentration ranging from 0 to 50% showed larger sizes ranging from 83.7 nm to 56.1 nm (Figure 4.4a to Figure 4.4d) compared to $Co_2(OH)_3Cl$ nanoparticles obtained at propanol concentration ranging from 70 to 100% which displayed smaller sizes ranging from 22.6 nm to 9.6 nm (Figure 4.4e to Figure 4.4h). These results confirm that both the average size and size distribution of $Co_2(OH)_3Cl$ nanoparticles are dependent on the propanol concentration. It was shown that the addition of propanol confines the growth of $Co_2(OH)_3Cl$ nanoplates.

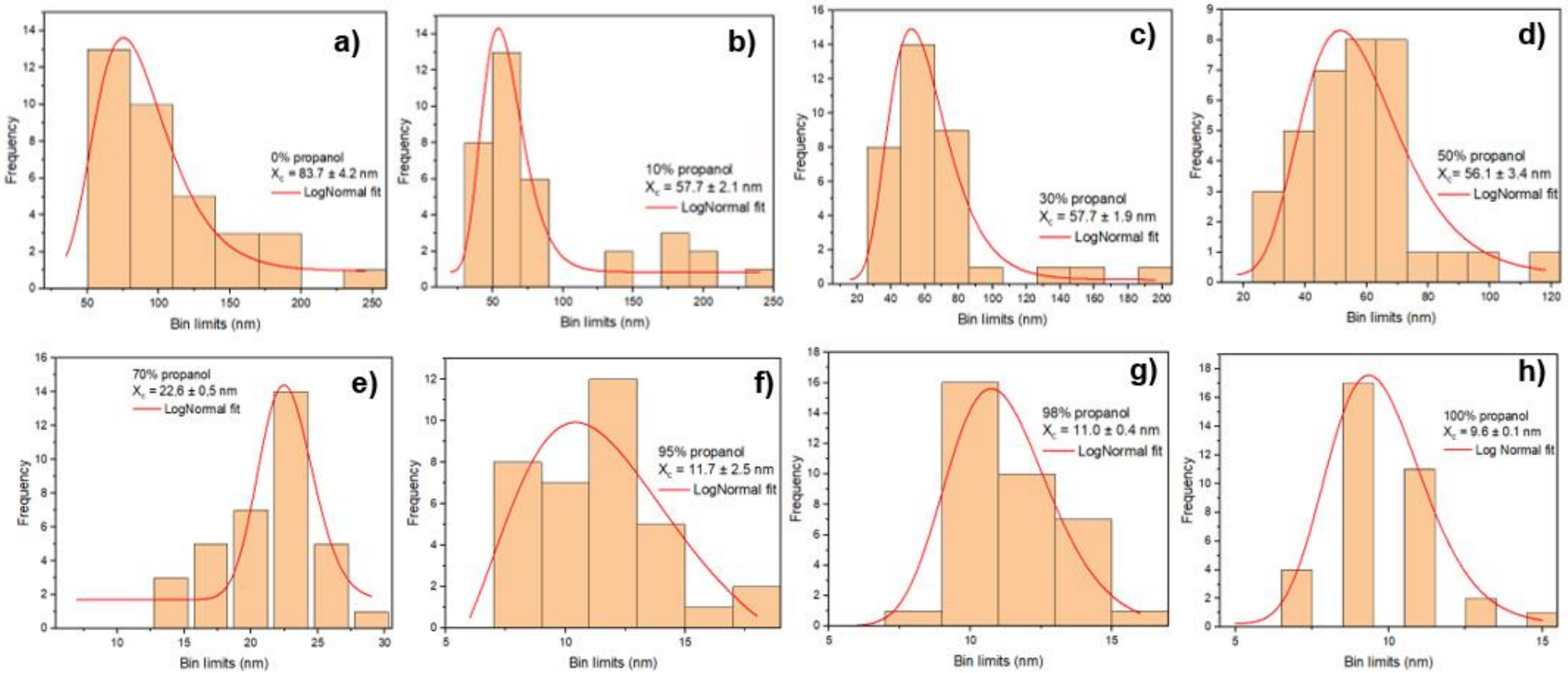

Figure 4.4: PSD curves of $Co_2(OH)_3Cl$ nanoparticles at different propanol concentrations

For example, at 50% propanol concentration, the diameter of the $Co_2(OH)_3Cl$ particles was reduced by 33% compared to when no propanol was used. Figure 4.5 presents the % reduction in particle diameter in presence of propanol relative to that without propanol.

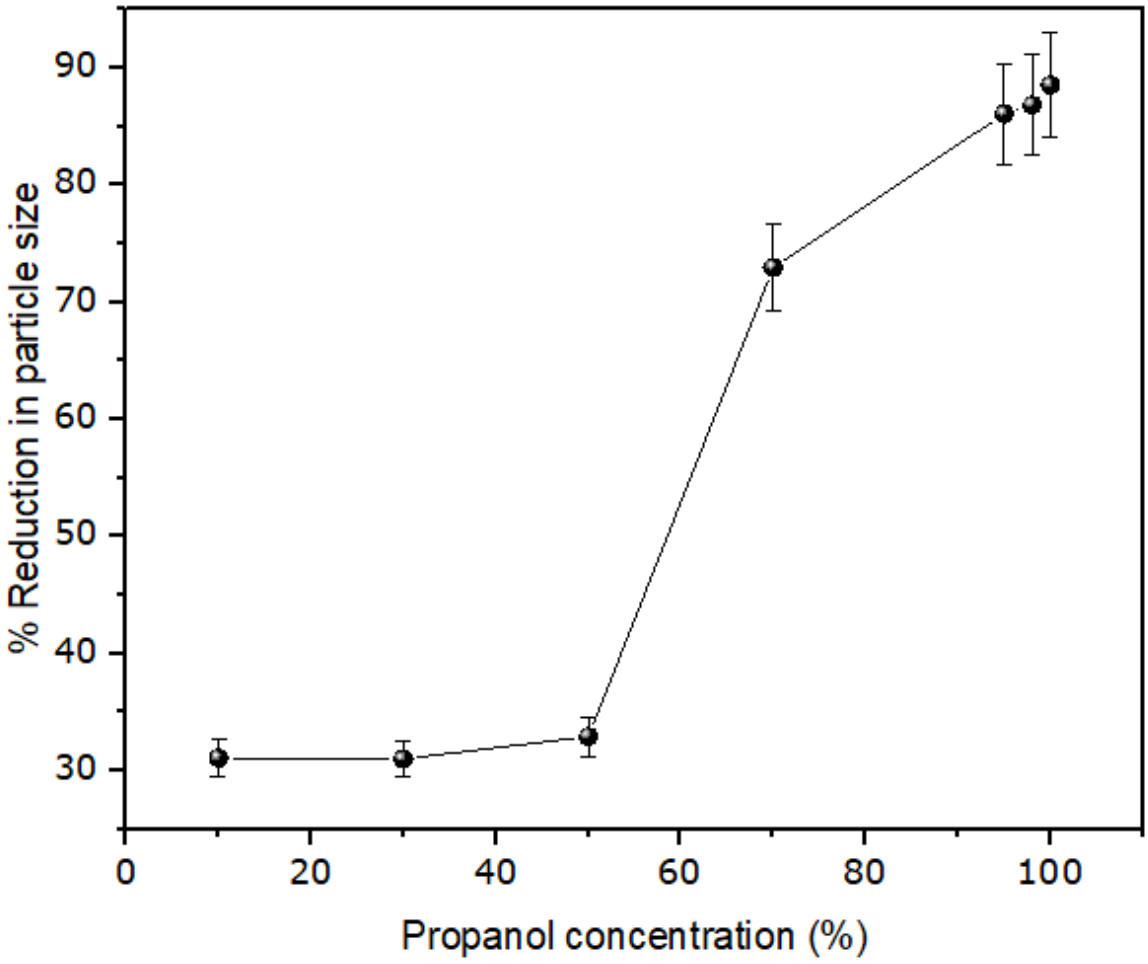

Figure 4.5: % Reduction in size of $Co_2(OH)_3Cl$ particles in propanol compared to no propanol

To the best of our knowledge, there is no study in the literature that reported the impact of propanol on the synthesis of $Co_2(OH)_3Cl$ particles. It was therefore impossible to directly compare the nucleation and growth of $Co_2(OH)_3Cl$ particles in propanol. The trend reported in this study differs from that reported by Heuvel et al. (2021), who found that the size of Co_3O_4 nanoparticles increased from 34 nm to 66 nm with propanol concentration increasing from 50% to 100%. However, it is similar to the findings of Chowdhury et al. (2014), that the addition of propanol inhibited the growth of akaganeite (β-FeOOH) nanorods transversally and longitudinally.

A variation in propanol concentration affects the structural arrangement of $Co_2(OH)_3Cl$ nanoparticles as well as their size and shape which is then reflected in the change in colour as shown in Figure 4.6.

Figure 4.6: $Co_2(OH)_3Cl$ nanopowders at propanol concentrations ranging from 0 to 100% (left to right)

At 0, 10, 30 and 50% propanol concentrations, different shades of green nanopowders were obtained, similar to that obtained by Feitknecht and Fischer (1935). Lavender nanopowders were produced in 70% and 100% propanol concentration, indicating that the polymorph in question was the β-$Co_2(OH)_3Cl$ (Feitknecht, 1935; de Wolff, 1953; Oswald & Feitknecht, 1964). Various shades of pink nanopowders were observed at 95 and 98% propanol concentrations indicating that the polymorph formed was the β-$Co_2(OH)_3Cl$ (García-Martínez et al., 1988). A summary of $Co_2(OH)_3Cl$ particle characteristics at different propanol concentration is provided in Table 4.1.

Table 4.1: Effect of propanol concentration on $Co_2(OH)_3Cl$ particle characteristics

Propanol concentration (%)	Phase	Morphology	Average size (nm)
0	$Co_2(OH)_3Cl$ + $Co_{1.176}(OH)_2Cl_{0.348}(H_2O)_{0.456}$	Hexagonal plates	83.7 ± 4.2
10	$Co_2(OH)_3Cl$ + $Co_{1.176}(OH)_2Cl_{0.348}(H_2O)_{0.456}$	Hexagonal plates	57.7 ± 2.1
30	$Co_2(OH)_3Cl$ + $Co_{1.176}(OH)_2Cl_{0.348}(H_2O)_{0.456}$	Hexagonal plates	57.7 ± 1.9
50	$Co_2(OH)_3Cl$ + $Co_{1.176}(OH)_2Cl_{0.348}(H_2O)_{0.456}$	Hexagonal plates	56.1 ± 3.4
70	$Co_2(OH)_3Cl$	Spheres	22.6 ± 0.5
95	$Co_2(OH)_3Cl$ + $CoN_5H_{15}Cl_3$	Spheres	11.7 ± 2.5
98	$Co_2(OH)_3Cl$ + NH_4Cl	Spheres	11.0 ± 0.4
100	$Co_2(OH)_3Cl$	Spheres	9.6 ± 0.1

4.2.1 Growth investigation of $Co_2(OH)_3Cl$ in water

Figure 4.7 illustrates the effect of water on $Co_2(OH)_3Cl$ nanoparticle morphology evolution over time. In Figure 4.7a, regular and irregular hexagonal plate like nanoparticles were formed after 60 min of synthesis. After 180 min of synthesis, hexagonal nanoplates continued to grow and some of them randomly attached, eventually producing aggregated particles (as shown in Figure 4.7b). Hexagonal nanoplates grew further and more aggregated particles resulting from stacked hexagonal nanoplates were formed after 360 min (Figure 4.7c). From the TEM images below (Figure 4.7a, b & c), it is suggested that the growth of hexagonal nanoplates can be explained via the OR mechanism while the aggregated particles were constructed from the assembly of hexagonal nanoplates. At 540 min of synthesis, spherical like particles grew significantly while hexagonal nanoplates completely disappeared (as shown in Figure 4.7d). Firmly aggregated nanospheres were also observed (Figure 4.7d). In Figure 4.6e, a mixture of polydisperse nanospheres and aggregate of nanospheres were produced. In Figure 4.7f, the self-assembly of spherical particles was observed and this can be attributed to OA mechanism. Additional TEM images are provided in Appendix B.1. A change in synthesis time affected the particle phase over a synthesis time range of 60 – 960 min in water. A mixture of phase ($Co_2(OH)_3Cl$ + $Co_{1.176}(OH)_2Cl_{0.348}(H_2O)_{0.456}$) was formed at 60, 180 and 360 min in water as shown by the XRD patterns in Figure 4.7g. However, pure $Co_2(OH)_3Cl$ particles was produced at 540, 720 and 960 min in water.

Particle size analysis was determined by counting 200 particles of each sample. For the 540 minutes sample, however, only 62 particles could be counted due to the type of images obtained. Since the norm is to count at least 200 particles for particle size distribution, it was important to assess the validity of using only 62 particles for particle size distribution. For the evaluation, 62 particles were randomly selected for the 60, 180, 360, 720 and 960 min samples. The average and standard deviation were determined and compared with those obtained from the 200 particles initially measured. The difference between the average obtained from 62 particles and 200 particles of the same samples was 18% for 60 min, 5% for 180 min, 6% for 360 min, 7% for 720 min and 8% for 960 min sample. Based on these slight variations, the results from the 62 particles for the 540 minutes sample are presented as representative under the circumstances. Therefore, a total of 62 particles have been counted from each sample to determine the average length and average diameter of $Co_2(OH)_3Cl$ nanoparticles (Table 4.2) in water. The $Co_2(OH)_3Cl$ particle sizes presented in Table 4.2 indicate that hexagonal nanoplates grew faster than nanospheres.

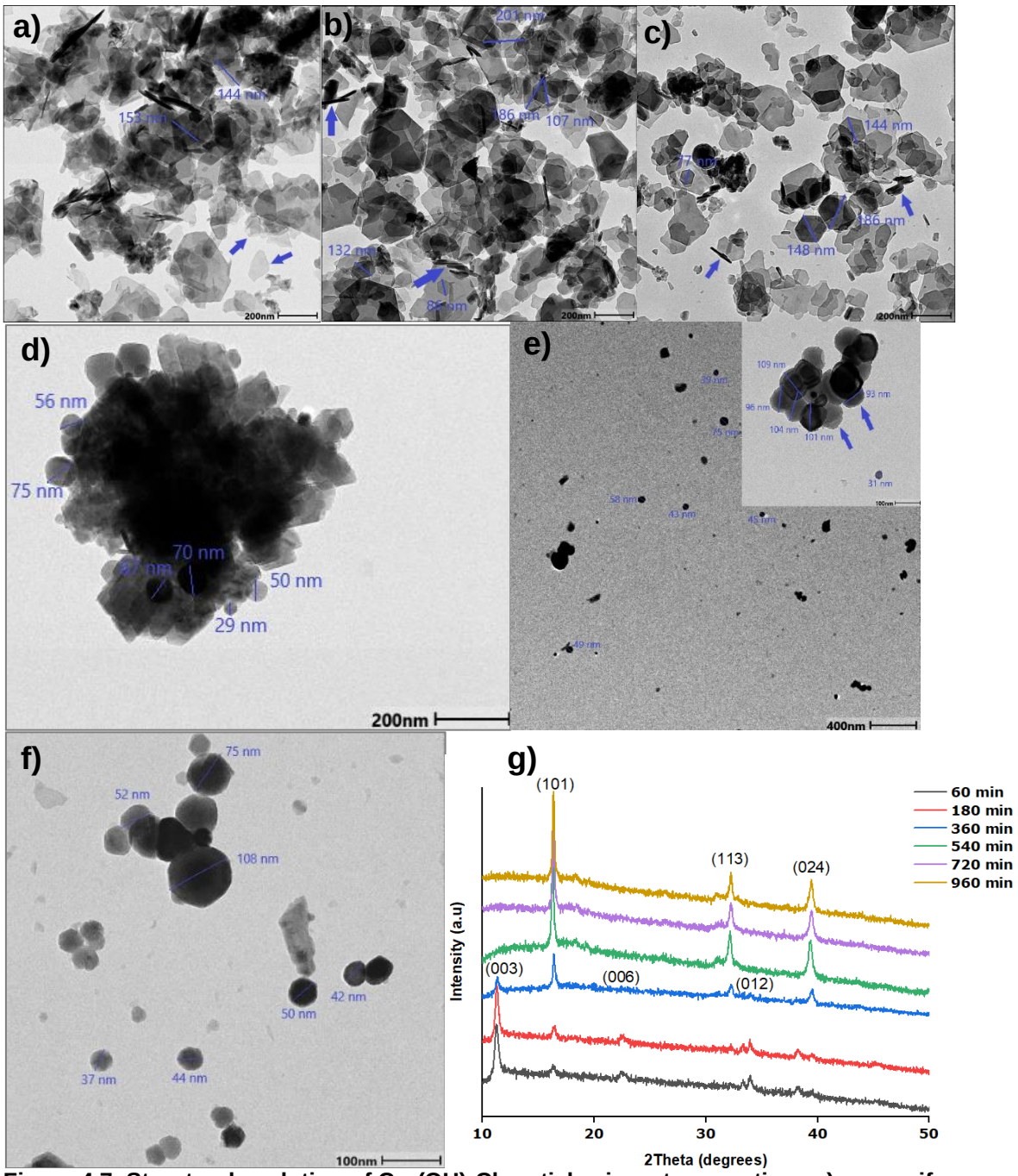

Figure 4.7: Structural evolution of $Co_2(OH)_3Cl$ particles in water over time, a) non-uniform hexagonal nanoplates after 60 min, b) regular hexagonal nanoplates after 180 min, c) mixture of hexagonal nanoplates and spherical particles after 360 min, d) aggregation of spherical particles after 540 min, e & f) attachment of nanospheres at 720 min and 960 min and g) XRD patterns of synthesised particles in water over time. Inset in (e) illustrates self-assembly of particles after 720 min

Table 4.2: Effect of time on $Co_2(OH)_3Cl$ particle characteristics in water

Time (min)	Phase	Morphology	Average diameter (nm)	Average length (nm)
60	$Co_2(OH)_3Cl$ + $Co_{1.176}(OH)_2Cl_{0.348}(H_2O)_{0.456}$	Hexagonal plates	N/A	108.1 ± 42.9
180	$Co_2(OH)_3Cl$ + $Co_{1.176}(OH)_2Cl_{0.348}(H_2O)_{0.456}$	Hexagonal plates	N/A	116.5 ± 59.0
360	$Co_2(OH)_3Cl$ + $Co_{1.176}(OH)_2Cl_{0.348}(H_2O)_{0.456}$	Hexagonal plates	N/A	137.6 ± 62.8
540	$Co_2(OH)_3Cl$	Spheres	64.6 ± 24.8	N/A
720	$Co_2(OH)_3Cl$	Spheres	65.7 ± 37.0	N/A
960	$Co_2(OH)_3Cl$	Spheres	66.8 ± 23.3	N/A

Figure 4.8 and 4.9 highlights the asymmetrical distribution curves of $Co_2(OH)_3Cl$ hexagonal nanoplates and nanospheres, respectively over time. It can be seen from Figure 4.8 that the PSD curves at 60 and 180 min represent right skewed curves with skewness = 1.0 and 1.3, respectively. The skewness, for the particle size distribution curve at 360 min was found to be 0.7, implying that unequal distribution occurs over time, confirming the presence of OA growth. Moreover, the distribution curves of $Co_2(OH)_3Cl$ hexagonal nanoplates become wider as the time progresses. According to Chowdhury et al. (2014), particle growth via OA mechanism results in wider and asymmetrical size distribution curve which suggests that $Co_2(OH)_3Cl$ hexagonal nanoplates growth in water occurred via OA mechanism. However, further research is needed on this because the TEM images clearly showed a structural transition from hexagonal nanoplates to spherical nanoparticles, potentially impacting the PSD analysis. Growth through OR or OA has been observed in various studies, resulting in either asymmetrical or symmetrical size distributions. Notably, the aging time has shown a greater impact on the final nanostructures, as it might indicate simultaneous operation of various growth mechanisms.

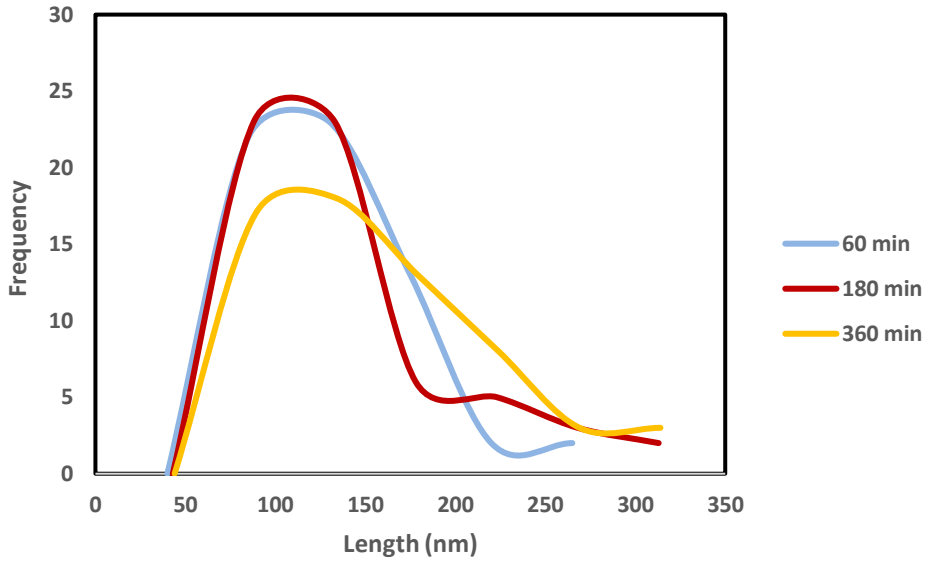

Figure 4.8: Particle size distribution of $Co_2(OH)_3Cl$ hexagonal nanoplates in water

Figure 4.9 show the asymmetrical distribution curves of nanospheres which also become broader as time progresses. A particle growth via OA mechanism would normally result in asymmetrical distribution curve, postulating that $Co_2(OH)_3Cl$ nanospheres growth in water is controlled by OA mechanism. However, further research is needed to confirm whether a simultaneous operation of various growth mechanisms is occurring.

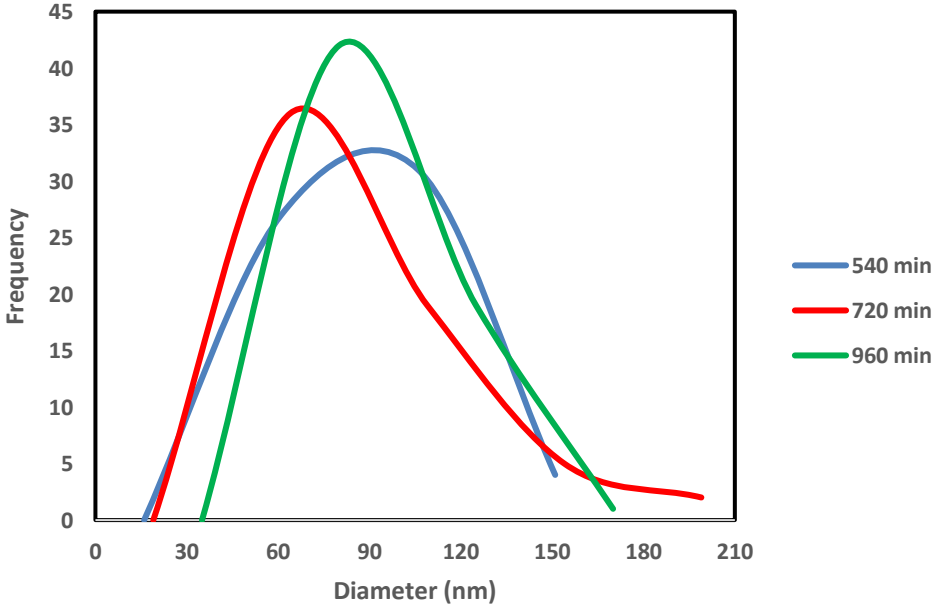

Figure 4.9: Particle size distribution of $Co_2(OH)_3Cl$ nanospheres in water

The growth investigation of $Co_2(OH)_3Cl$ nanopowders in 70% propanol is presented in the following section. At 70% propanol, $Co_2(OH)_3Cl$ nanoplates lost their hexagonal shape,

resulting in sphere like particles as well as irregular aggregated particles. A colour change from green to lavender was observed for $Co_2(OH)_3Cl$ nanopowders at 70% propanol. Due to the low stability of green $Co_2(OH)_3Cl$ compared to lavender $Co_2(OH)_3Cl$ as reported by García-Martínez et al. (1988), it was necessary to investigate the growth kinetics of $Co_2(OH)_3Cl$ nanopowders in 70% propanol. At 70%propanol, a threshold where a change in structure was observed.

4.2.2 Growth investigation of $Co_2(OH)_3Cl$ in 70% propanol

The effect of 70% propanol on the morphological evolution of $Co_2(OH)_3Cl$ nanoparticles over time is presented in Figure 4.10. The products obtained after 60 min of reaction, which contains a mixture of small sphere like nanoparticles as well as irregular shape aggregates, can be seen in Figure 4.10a. When the reaction time was extended to 180 min, nanospheres grew from the small spherical particles (as shown in Figure 4.10b). After 360 min of reaction, the same phenomenon was observed (Figure 4.10c). It is believed that OR mechanism should be the main driving force for such growth. After extending the reaction to 540, 720 and 960 min, it was noticed that nanospheres aggregated to form larger nanospheres to decrease the surface energy (Figure 4.10d). TEM images of $Co_2(OH)_3Cl$ spherical like nanoparticles obtained after 540 and 720 min are provided in Appendix C.1. In general, the growth of $Co_2(OH)_3Cl$ particles in 70% propanol did not result in a change in particle shape compared to $Co_2(OH)_3Cl$ particle growth in water. A total of 200 particles have been counted from each of the synthesised products to conduct the particle size analysis and the average diameter of $Co_2(OH)_3Cl$ nanoparticles was determined.

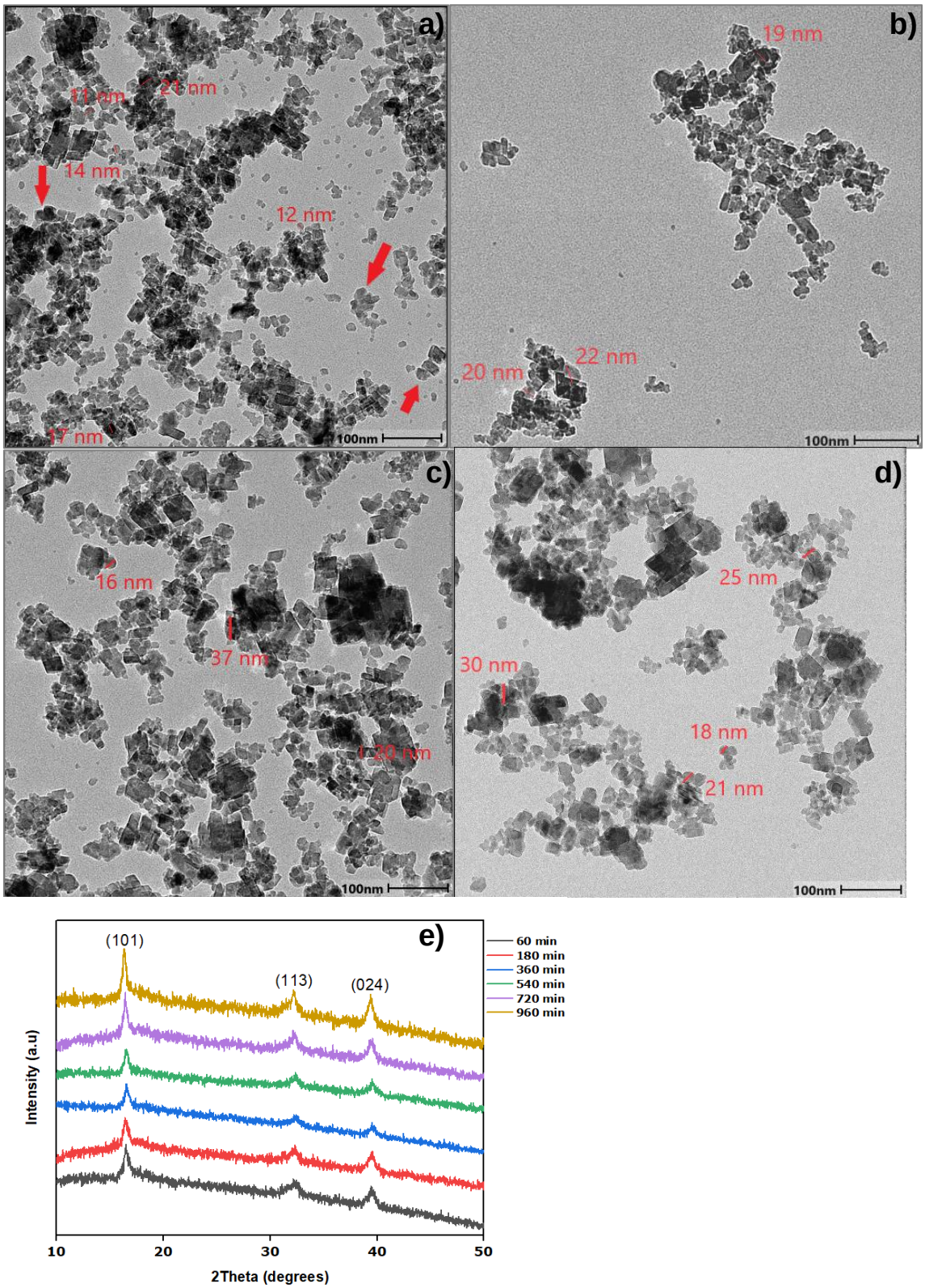

Figure 4.10: Morphological evolution of $Co_2(OH)_3Cl$ particles in 70% propanol over time, a) a mixture of nanosized spheres and aggregated particles after 60 min, b & c) nanospheres growth via OR mechanism at 180 and 360 min, d) nanospheres growth via OA mechanism at 960 min and e) XRD patterns of synthesised particles in 70% propanol over time

It appears that propanol inhibited the growth of $Co_2(OH)_3Cl$ nanospheres compared to water, which resulted in a minor increase in their average diameter as shown in Table 4.3.

Table 4.3: Effect of time on $Co_2(OH)_3Cl$ particle characteristics in 70% propanol

Time (min)	Average diameter (nm)	Phase	Morphology
60	14.3 ± 3.6	$Co_2(OH)_3Cl$	Spheres
180	15.6 ± 4.5	$Co_2(OH)_3Cl$	Spheres
360	17.5 ± 6.1	$Co_2(OH)_3Cl$	Spheres
540	19.4 ± 7.3	$Co_2(OH)_3Cl$	Spheres
720	20.3 ± 7.8	$Co_2(OH)_3Cl$	Spheres
960	23.2 ± 6.6	$Co_2(OH)_3Cl$	Spheres

Figure 4.11 highlights the time dependent distribution curves of $Co_2(OH)_3Cl$ nanospheres. It can be seen from Figure 4.11 that the particle size distribution curve at 60 min represents a nearly symmetrical curve (skewness = 0.5). From 180 min to 960 min, right skewed distribution curves were obtained. Furthermore, it can be noticed that the $Co_2(OH)_3Cl$ nanospheres distribution curves become wider as the processing time increases. Normally, a particle growth via OA mechanism would result in asymmetrical distribution curve, postulating that $Co_2(OH)_3Cl$ nanospheres growth in 70% is controlled by OA mechanism as time increases.

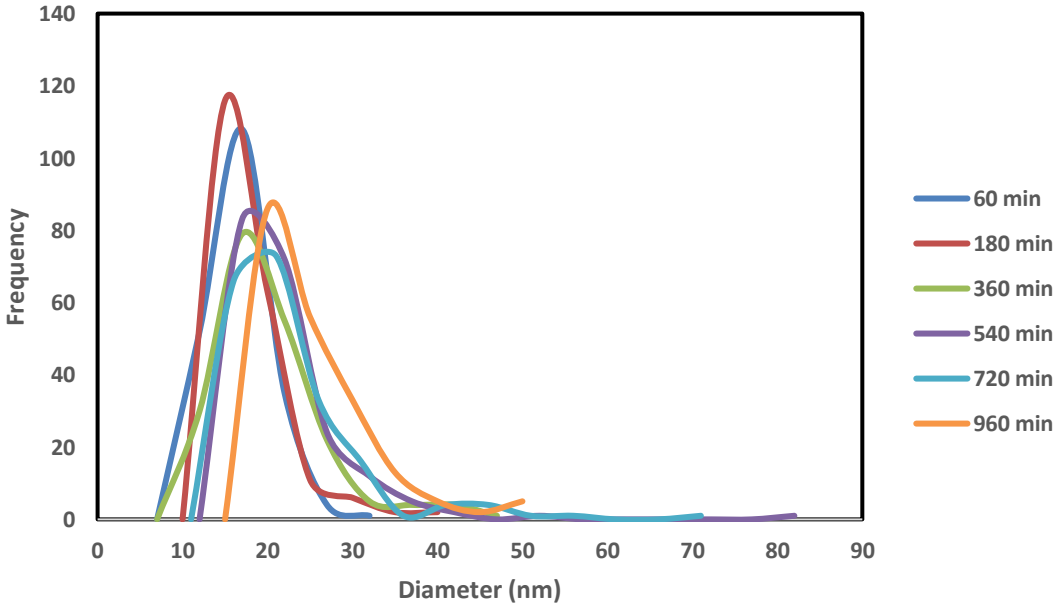

Figure 4.11: Particle size distribution of $Co_2(OH)_3Cl$ nanospheres in 70% propanol

4.2.3 Effect of water on the growth kinetics of $Co_2(OH)_3Cl$ nanoparticles

Figure 4.12 presents the two-stage hydrothermal growth of $Co_2(OH)_3Cl$ nanoparticles in water. The first stage is that of $Co_2(OH)_3Cl$ hexagonal nanoplates while the second one is that of nanospheres. Both OR kinetics and OA kinetics were evaluated in attempt to identify the controlling growth mechanism. It can be seen from Figure 4.13 that both OR and OA mechanism models can be fitted to the data.

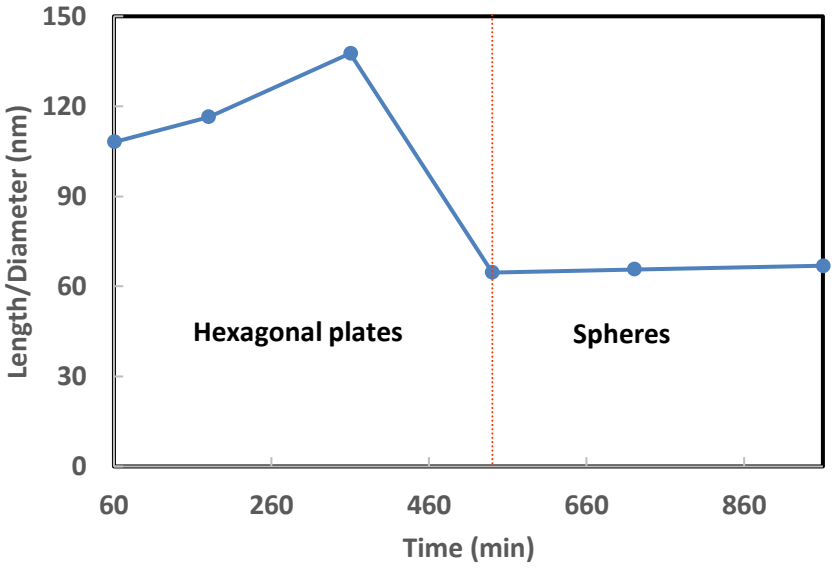

Figure 4.12: $Co_2(OH)_3Cl$ nanoparticles growth in water

In the first stage, OR kinetics fit the data well at 180 min, while OA kinetics fit it well at 360 min. It is likely that OR kinetics was dominant over OA kinetics because the PSD curve at 180 min was asymmetrical. In the second stage (nanospheres growth), the goodness of fit, R^2 was found to be >0.99, for both growth kinetics, postulating that OR and OA kinetics occur simultaneously. In a recent study, Wang et al. (2022) proposed a mixed growth pathway for the hydrothermal synthesis of $Co_2(OH)_3Cl$ microspheres in a triethanolamine/water system at 200 °C for 24 h. The microspheres were constructed from the growth of octahedron subunits via OR kinetics then those subunits self-assembled. Kinetic evaluation confirms the existence of OA growth kinetics, further validating the relationship between growth mechanism and particle size distribution curve as discussed above. The rate constant, K, for both OR and OA kinetics as well as the exponent, n, for OR kinetics were obtained using multivariable regression and summarised in Table 4.4. Chowdhury et al. (2014) used a similar method to determine the variables of OR and OA kinetics models and they concluded that this method provides accurate analysis. The exponent, n for OR kinetics of hexagonal nanoplates was found to be ~2 indicating an interface controlled growth. This means that hexagonal nanoplates grew by diffusion along the matrix-particle boundary. On the other

hand, the exponent, n for OR kinetics of nanospheres was found to be ~3 which corresponds with a diffusion-controlled OR growth.

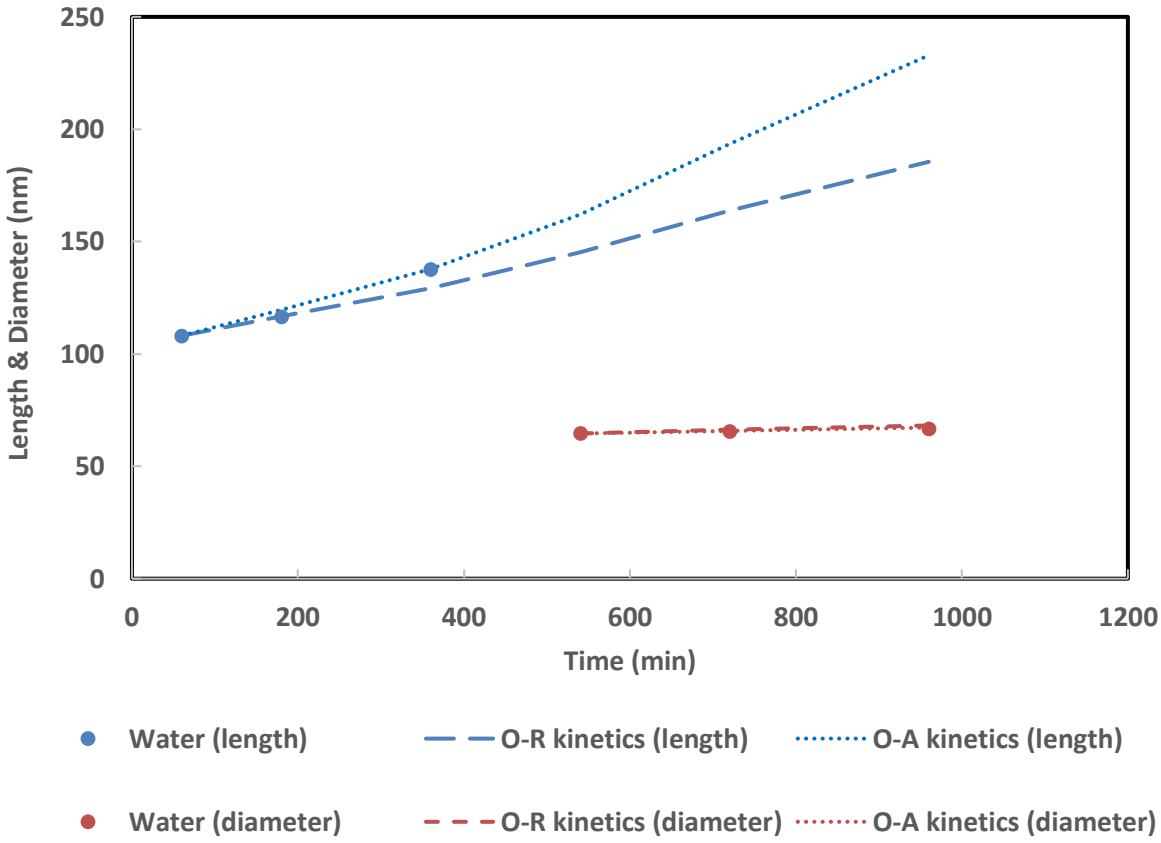

Figure 4.13: $Co_2(OH)_3Cl$ growth kinetics in water

It was found that the rate constants for hexagonal nanoplates growth are significantly higher than those for nanospheres growth as shown in Table 4.4.

Table 4.4: $Co_2(OH)_3Cl$ rate constants for both growth mechanisms in water

Solvent	K_{OR} (min^{-1})	K_{OR} (min^{-1})	K_{OA} (min^{-1})	K_{OA} (min^{-1})
Water	Hexagonal plates	Spheres	Hexagonal plates	Spheres
	0.48	0.19	0.0039	0.00010

4.2.4 Effect of 70% propanol on the growth kinetics of $Co_2(OH)_3Cl$ nanoparticles

Figure 4.14 presents the hydrothermal growth of $Co_2(OH)_3Cl$ nanospheres in 70% propanol which is nearly linear.

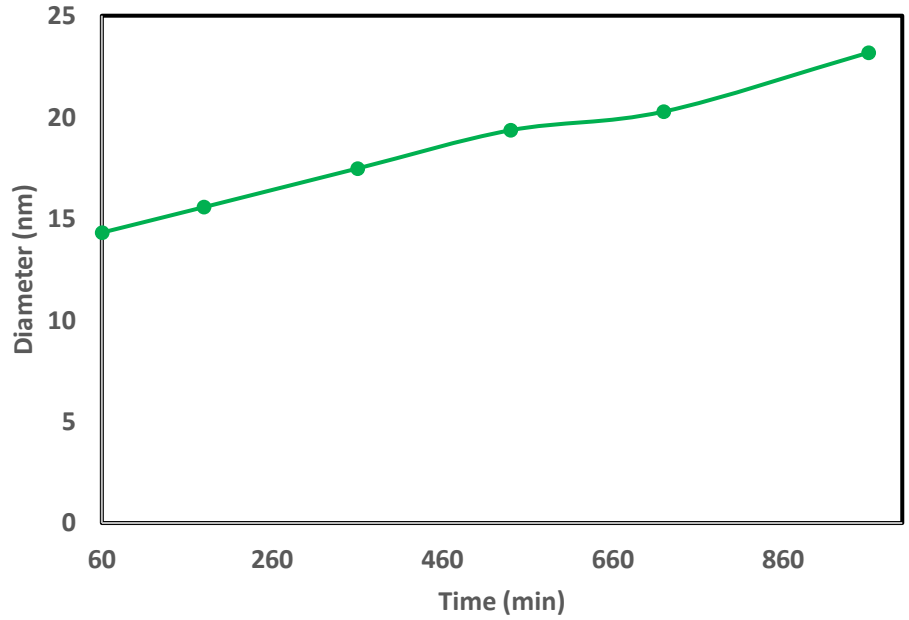

Figure 4.14: $Co_2(OH)_3Cl$ nanoparticles growth in 70% propanol

Both OR kinetics and OA kinetics were evaluated to identify the controlling growth mechanism. It can be seen from Figure 4.15 that both OR and OA mechanism models can be fitted to the experimental data. The OR kinetics, however, was dominant up to 540 min and then the OA kinetics prevailed for the remainder of nanosphere growth.

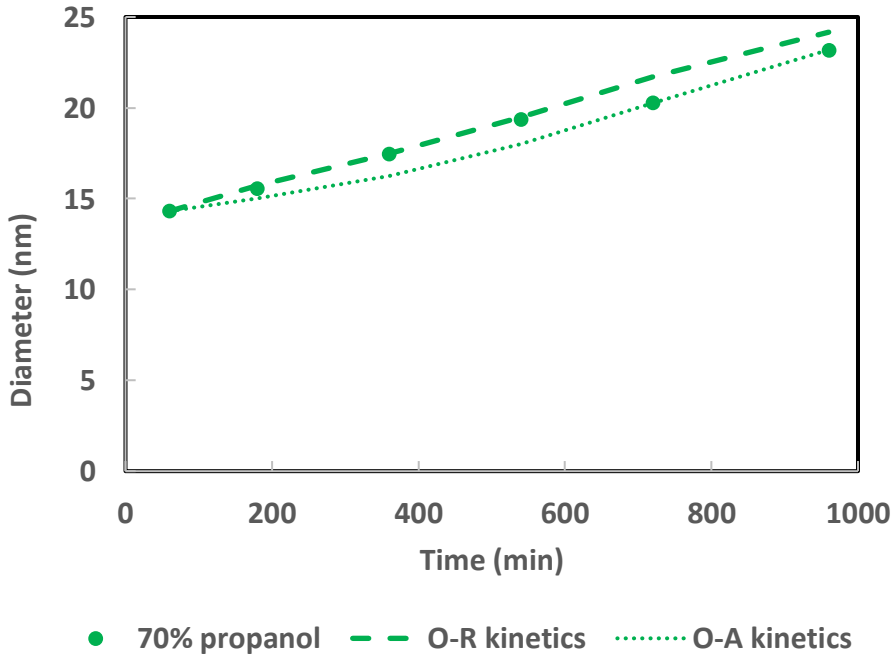

Figure 4.15: $Co_2(OH)_3Cl$ growth kinetic in 70% propanol

From 180 min to 540 min, the PSD curves of nanospheres are asymmetrical, which suggests an OR growth kinetics, but the kinetic evaluation (Figure 4.15) indicates an OA growth kinetics. A further study is necessary to clarify why the OA growth kinetics underestimated the growth of nanospheres over 180 min to 540 min.

The rate constants, K, for both mechanisms are presented in Table 4.5. The exponent, n, for OR kinetics was found to be ~3 which corresponds with a diffusion-based growth controlled by diffusion in the matrix.

Table 4.5: $Co_2(OH)_3Cl$ rate constants for both growth mechanisms in 70% propanol

Solvent	K_{OR} (min^{-1})	K_{OA} (min^{-1})
70% propanol	0.25	0.0013

4.3 Conclusion

The impact of varying propanol concentration on $Co_2(OH)_3Cl$ nanoparticles characteristics was reported. A mixture of $Co_{1.176}(OH)_2Cl_{0.348}(H_2O)_{0.456}$ and $Co_2(OH)_3Cl$ green nanopowders was obtained from 0 to 50% propanol concentration. However, β-phased $Co_2(OH)_3Cl$ was obtained in the presence of propanol concentrations ranging from 70 to 100%. Propanol concentrations at 95 and 98% resulted in pink $Co_2(OH)_3Cl$ nanopowders whereas lavender β-phased $Co_2(OH)_3Cl$ nanopowders were obtained at 70 and 100%. $Co_2(OH)_3Cl$ nanospheres with a high purity level were produced in the presence of solvents with higher propanol content. Additionally, increasing the propanol concentration from 0 to 70% resulted in a transition from $Co_2(OH)_3Cl$ hexagonal nanoplates to spherical nanoparticles. In this study, an increment in propanol concentration reduced the $Co_2(OH)_3Cl$ particle size which differs from the one reported for the synthesis of rhombic Co_3O_4 nanoparticles in which an increase in propanol concentration resulted in larger Co_3O_4 nanoparticles without affecting their shape. Time dependent experiments have been conducted to understand $Co_2(OH)_3Cl$ nanoparticle growth in pure water and 70% propanol, respectively. In water, $Co_2(OH)_3Cl$ hexagonal nanoplates were produced from 60 to 360 min of synthesis whereas nanospheres were formed from 540 to 960 min. In contrast, only spherical nanoparticles formed in 70% propanol from 60 to 960 min. From 960 minutes of synthesis, pure water produced spherical particles of 67 nm diameter, whereas propanol produced smaller nanospheres (23 nm). The average reduction in size for the lowest synthesis time and the longest synthesis time confirmed that the reduction in particle size is around 70%. It has been demonstrated that during the propanol-based growth of $Co_2(OH)_3Cl$, prolonged reaction times are not necessary to produce smaller nanospheres. Consequently, using propanol as solvent can result in a reduction in energy consumption during the hydro/solvothermal process. Kinetic evaluation in water revealed that hexagonal nanoplates grew first via OR kinetics then OA kinetics while OR and OA growth kinetics occurred simultaneously for nanospheres. The growth of

$Co_2(OH)_3Cl$ nanospheres in 70% propanol was controlled first by OR kinetics, then by OA kinetics. These results indicate that changing the solvent medium while retaining the same processing time can significantly modify the morphology of $Co_2(OH)_3Cl$ nanoparticles. However, $Co_2(OH)_3Cl$ particle morphology was not altered despite the change in solvent medium from 540 minutes to 960 minutes of synthesis.

CHAPTER 5 IMPACTS OF PARTICLE SIZE/SHAPE AND TEMPERATURE ON THE PROPERTIES OF $Co_2(OH)_3Cl$ NANOFLUIDS

5.1 Introduction

This study explores the influence of $Co_2(OH)_3Cl$ particle size and shape on the properties of the resulting nanofluids. Additionally, it presents the correlation between the properties of $Co_2(OH)_3Cl$ nanofluids and temperature.

5.2 Nanofluid characterization

Figure 5.1 shows the transmittance spectrum of both water and the water-based suspensions of $Co_2(OH)_3Cl$ at 0.03 wt%. Results revealed that both $Co_2(OH)_3Cl$ nanofluids and water exhibit absorption peaks (1149 nm and 972 nm) in the near infrared region. At 1149 nm, it can be seen that the transmittance of $Co_2(OH)_3Cl$ nanoparticles reduced from ~43% to 27% with an increase in propanol concentration. $Co_2(OH)_3Cl$ nanoparticle transmittance at 972 nm declined from ~64% to 34% with increasing propanol content. In the visible region (400-700 nm), water was highly transparent (~88% transmittance) while $Co_2(OH)_3Cl$ particles showed a significant reduction in transmittance, indicating their capabilities to absorb visible light. Furthermore, the $Co_2(OH)_3Cl$ particles transmittance decreased with a rise in propanol concentration from 0 to 100%.

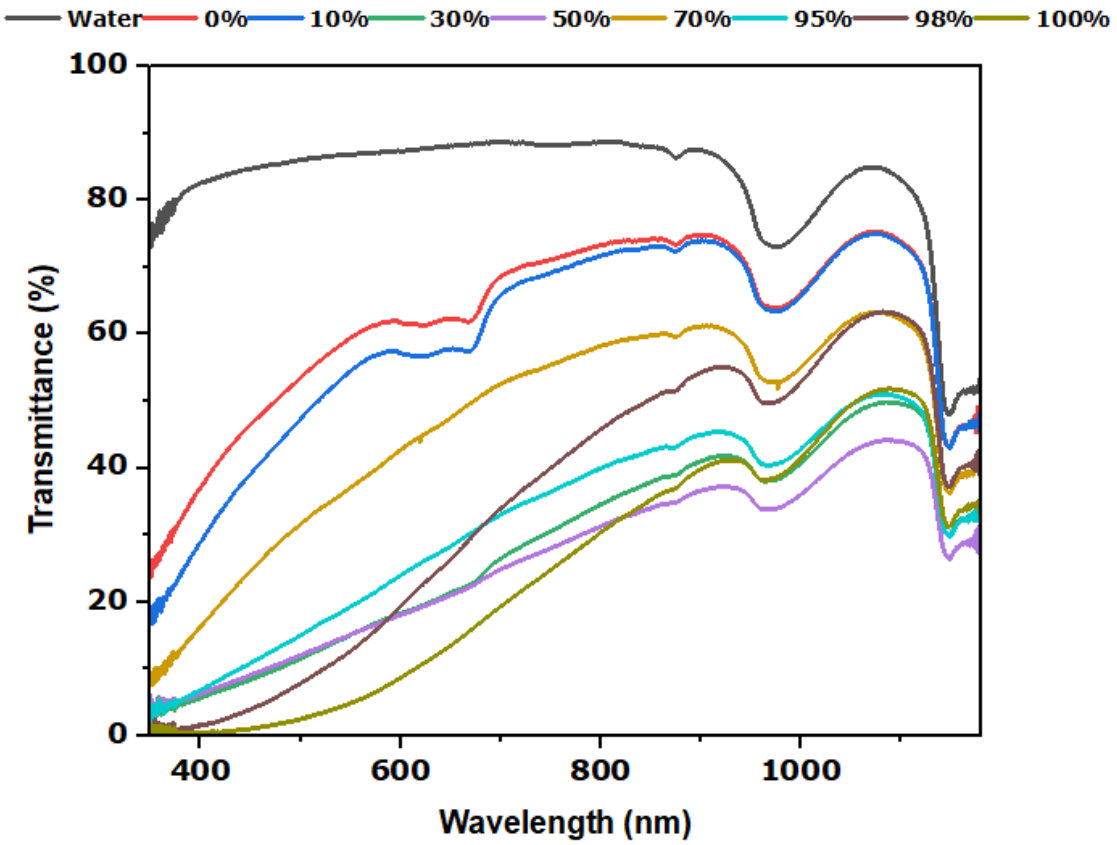

Figure 5.1: UV-VIS-NIR spectrum of $Co_2(OH)_3Cl$-H_2O nanofluids prepared at different propanol concentrations

5.2.1 Viscosity of $Co_2(OH)_3Cl$-H_2O nanofluid

Viscosity describes the resistance shown by a fluid when being deformed, which affects many other phenomena within the fluid, such as mass and heat transfer (Hemmati-Sarapardeh et al., 2018). For industrial applications, the viscosity of nanofluids can significantly influence the pumping power, pressure drop, and the convective heat transfer coefficient (Kole & Dey, 2010). Consequently, the study of $Co_2(OH)_3Cl$-H_2O nanofluid viscosity fabricated via the two step method is critical prior to its application in a given heat transfer engineering system. It can be observed that the viscosity is independent of shear rate indicating a Newtonian flow behaviour for water at all temperatures up to ~85 s^{-1}, as shown in Figure 5.2. It was also clear that water viscosity decreased with increasing temperature. Additionally, Figure 5.2 indicates that $Co_2(OH)_3Cl$ nanoparticle addition slightly affected water as Newtonian behaviour was mostly retained across the shear rate range examined. Figure 5.3 illustrates the viscosity of water based nanofluids containing $Co_2(OH)_3Cl$ synthesised at different particle sizes as a function of temperature and constant shear rate (60.7 s^{-1}). As temperature increases, $Co_2(OH)_3Cl$ nanoparticles move more quickly.

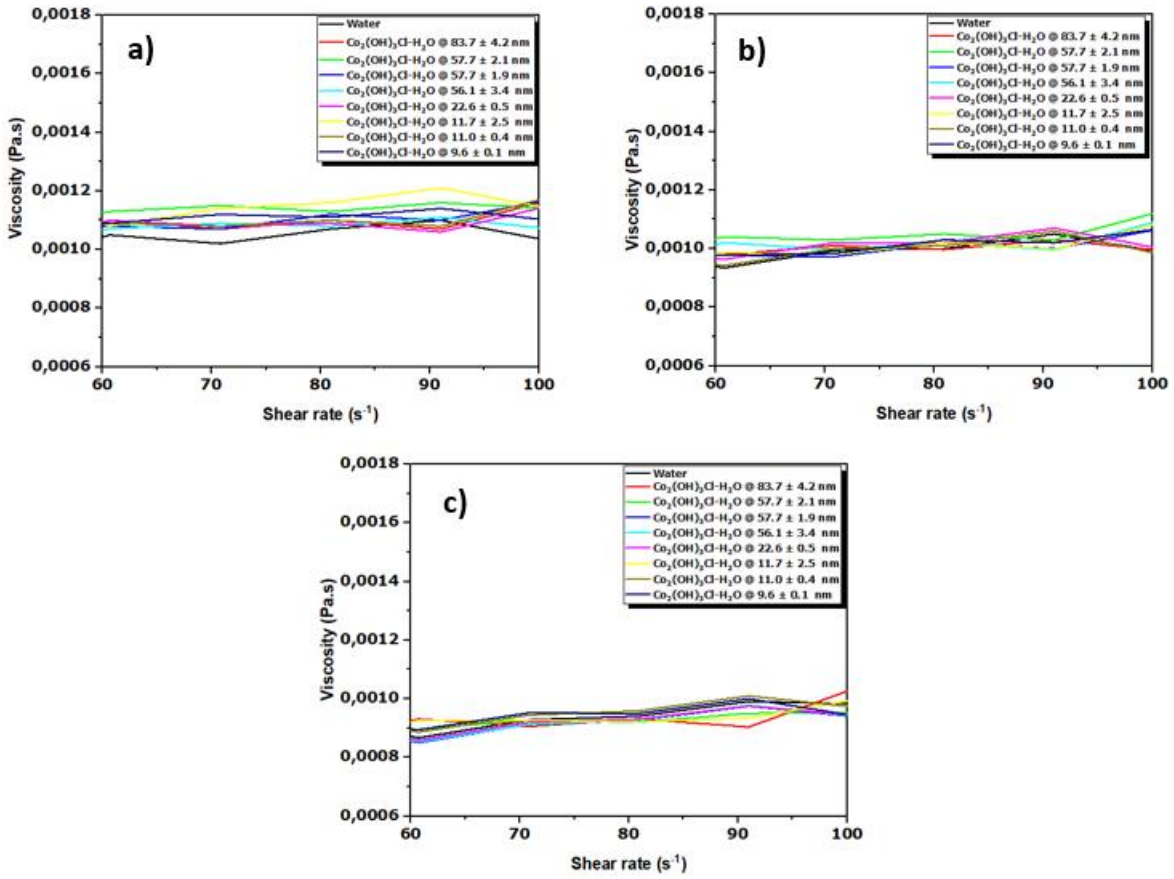

Figure 5.2: Viscosity of water and $Co_2(OH)_3Cl$ nanofluids in accordance with shear rate at 298 K (a), 303 K(b) and 308 K (c)

The intensified movement of $Co_2(OH)_3Cl$ nanoparticles results in a reduction in both inter and intra molecular interactions between nanoparticles and fluid molecules hence, reducing internal friction or stress and therefore decreasing viscosity (Sekhar et al., 2018; Alsboul et al., 2022; Rahman Salari et al., 2022). The majority of $Co_2(OH)_3Cl$-H_2O nanofluids exhibited higher viscosities than those of water at all temperatures except for those containing $Co_2(OH)_3Cl$ nanoparticles at 57.7 ± 1.9 nm, 56.1 nm and 22.6 nm which have lower viscosities than water at 308 K. Similar findings were reported for the water based carbon nanotubes nanofluids at 0.2 vol% from 278 to 338 K and this was attributed to the lubricative effect of carbon nanotubes nanoparticles (Chen et al., 2008c; Chen et al., 2011). Beyond 0.2 vol%, they observed that the viscosity of carbon nanotubes based nanofluids were higher than that of water (Chen et al., 2008c; Chen et al., 2011). Further studies should be carried out to verify whether the trend exhibited by some $Co_2(OH)_3Cl$-H_2O nanofluids at 0.03 wt% will be reproduced or not at higher particle weight concentrations. At 303 K, the nanofluid made of $Co_2(OH)_3Cl$ nanoparticles at 57.7 ± 2.1 nm displayed the highest augmentation in viscosity of ~11%. Unexpectedly, at 308 K, however, the nanofluid made of $Co_2(OH)_3Cl$ particles at 57.7 ± 2.1 nm displayed an increase in viscosity of ~3%. The viscosity increase of

$Co_2(OH)_3Cl$-H_2O nanofluids at 303 K at particle sizes ranging from 83.7 to 9.6 nm is presented in Figure 5.3. In comparison to the nanofluid made of $Co_2(OH)_3Cl$ nanoparticles at 83.7 nm, the nanofluid made of $Co_2(OH)_3Cl$ nanoparticles at 57.7 ± 2.1 nm exhibited the highest increase in viscosity. This is probably due to the smaller size of $Co_2(OH)_3Cl$ nanoparticles used to prepare the nanofluid which provide them more surface area per unit volume resulting in an increase in friction and resistance to flow hence, the observed higher viscosity. Previous experimental and numerical studies have reported similar results regarding the impact of particle size on the viscosity of aqueous nanofluids of CuO and Al_2O_3, respectively (Lu & Fan, 2008; Pastoriza-Gallego et al., 2011; Kwek et al., 2010). Despite their almost identical sizes, the viscosity increases obtained for the nanofluid made of $Co_2(OH)_3Cl$ nanoparticles at 57.7 ± 1.9 nm and 56.1 nm, respectively were lower than that of the nanofluid made of $Co_2(OH)_3Cl$ nanoparticles at 57.7 ± 2.1 nm. The latter observation requires further investigation since there was no sedimentation of nanoparticles observed after the viscosity analysis.

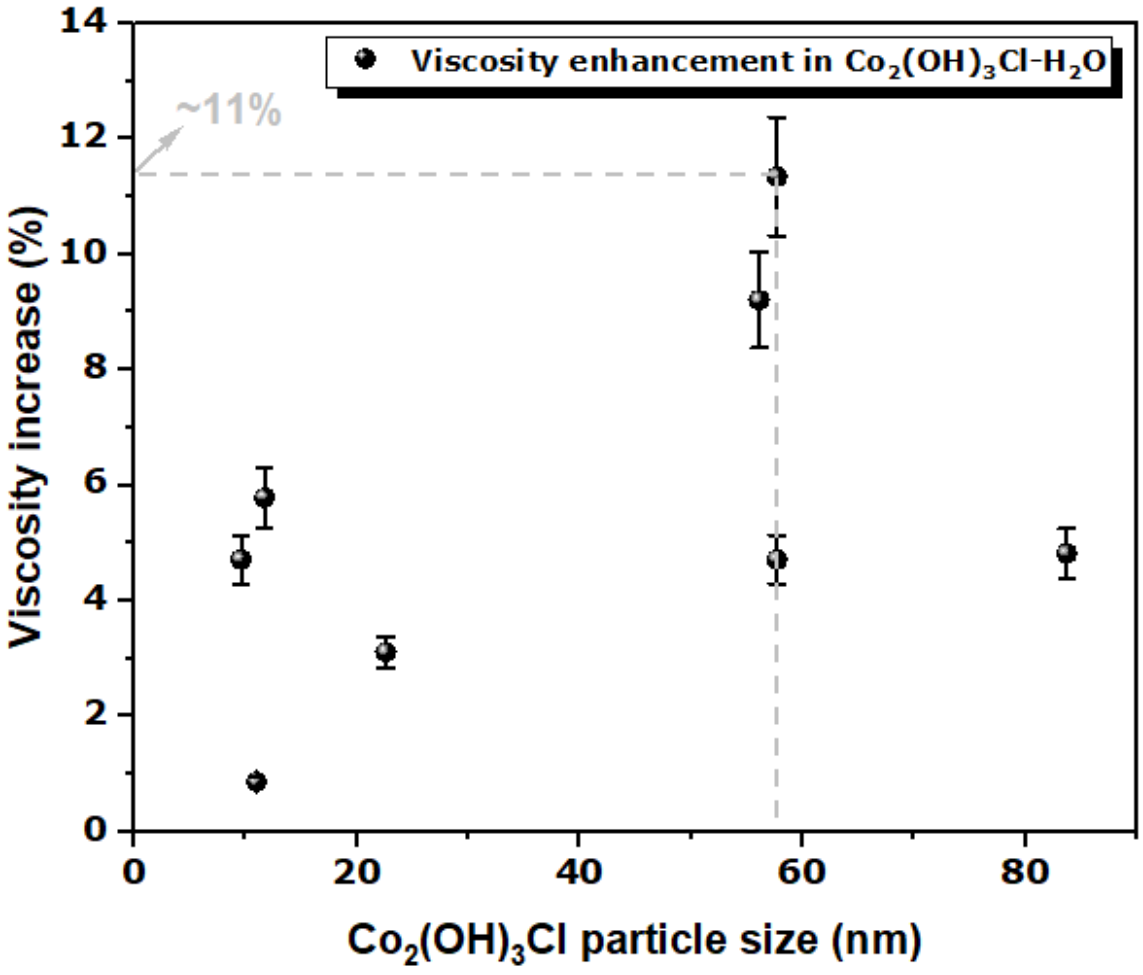

Figure 5.3: Viscosity increase of $Co_2(OH)_3Cl$ nanofluids at different particle sizes

The nanofluid made of $Co_2(OH)_3Cl$ nanoplates at 57.7 ± 2.1 nm exhibited the highest viscosity increase when compared to the nanofluids made of spherical $Co_2(OH)_3Cl$ nanoparticles at particle sizes ranging from 22.6 to 9.6 nm. This was possibly due to the hexagonal plate like shape of $Co_2(OH)_3Cl$ nanoparticles at 57.7 ± 2.1 nm which limited their rotational and translational Brownian motions. Similar findings were reported by Jeong et al. (2013) where the viscosity of aqueous nanofluids made of nearly rectangular ZnO shaped particles was higher than that of spherical particles based nanofluids. A comparison was established between the study of He et al. (2007) and that of (Chen et al., 2008b) which demonstrated that the viscosity of spherical TiO_2 nanoparticles based nanofluids is significantly lower than that of TiO_2 nanotubes based nanofluids. From the results depicted in Figure 5.3, a general trend between the $Co_2(OH)_3Cl$ nanofluid viscosity increment and the propanol concentration ranging from 83.7 to 9.6 nm cannot be extracted. However, it was observed that the $Co_2(OH)_3Cl$ nanofluid viscosity increases with increasing particle size. Therefore, a modified version of the impact of particle size on viscosity increase of $Co_2(OH)_3Cl$-H_2O nanofluids at 303 K is provided in Figure 5.4.

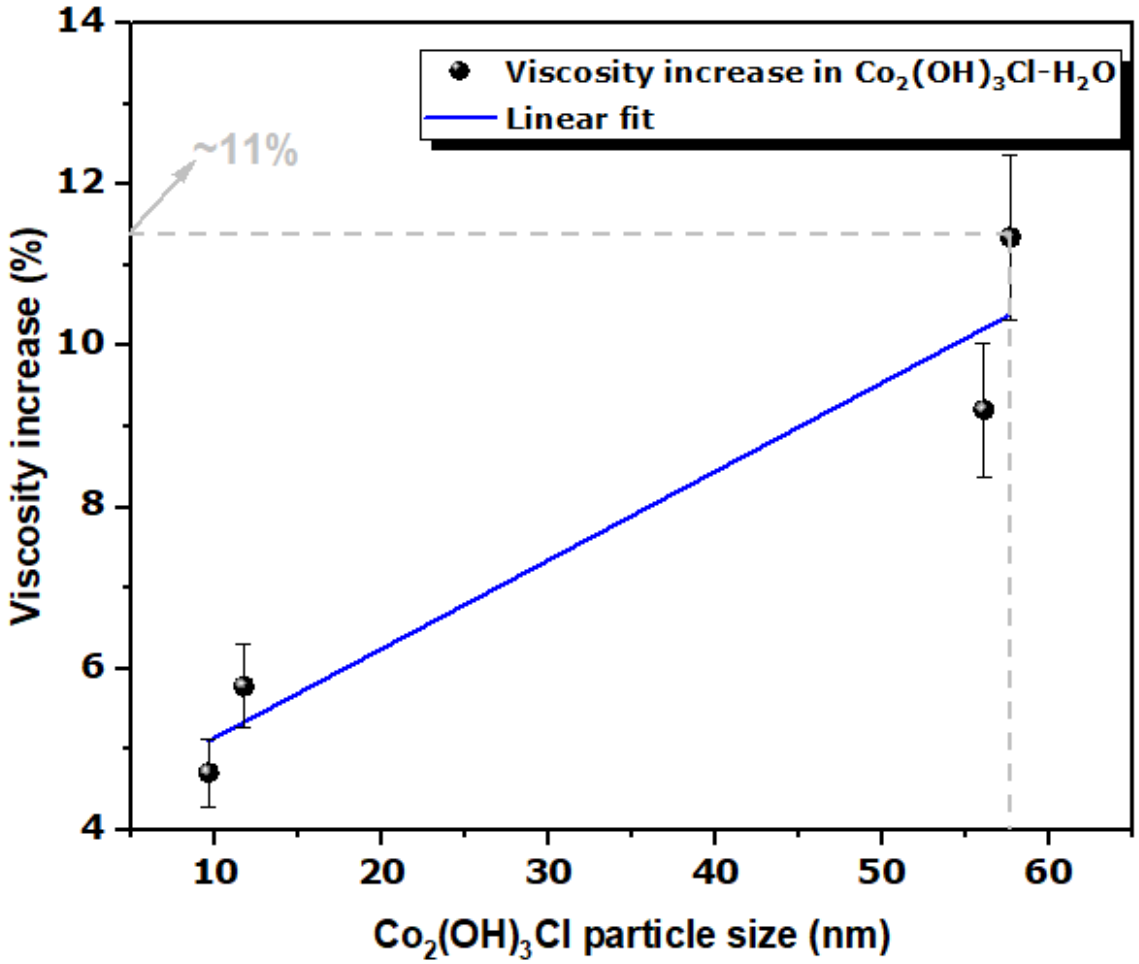

Figure 5.4: Modified version of viscosity increase of $Co_2(OH)_3Cl$ nanofluids at different particle sizes

$Co_2(OH)_3Cl$ nanoparticles at higher particle sizes and lower propanol concentrations (57.7 nm and 56.1 nm) have a hexagonal plate shape, whereas those at lower particle sizes and higher propanol concentrations (11.7 nm and 9.6 nm) are spherical. From Figure 5.4, it is clearly evident that the shape of $Co_2(OH)_3Cl$ nanoparticles dispersed in water has an impact on the increase in nanofluid viscosity. Nanofluids containing $Co_2(OH)_3Cl$ nanoparticles at higher particle sizes (57.7 nm and 56.1 nm) exhibited higher viscosities than those containing $Co_2(OH)_3Cl$ nanoparticles at lower particle sizes (11.7 nm and 9.6 nm). However, the influence of $Co_2(OH)_3Cl$ particle size on the increase in viscosity of their nanofluids is unclear. A decrease in the size of both $Co_2(OH)_3Cl$ hexagonal nanoplates and $Co_2(OH)_3Cl$ nanospheres appears to result in decreasing nanofluid viscosity increase. The latter trend is contrary to that observed between the viscosity increase of nanofluid made of $Co_2(OH)_3Cl$ at 83.7 nm and that of nanofluid made of $Co_2(OH)_3Cl$ at 57.7 nm. A possible reason for the unexpected result may be the distribution of $Co_2(OH)_3Cl$ nanoparticles in the base fluid.

According to Goharshadi et al. (2013), nanofluids with a wide particle distribution have better packing ability than those with of a narrow particle distribution at a constant volume fraction. The wider the distribution of nanoparticles, the freer space they have to move around, and eventually the suspension becomes less viscous. It is likely that, at constant weight concentration, the nanofluid made of $Co_2(OH)_3Cl$ nanoparticles at 57.7 nm exhibited a higher viscosity than that containing $Co_2(OH)_3Cl$ nanoparticles at 56.1 nm due to the narrow size distribution of $Co_2(OH)_3Cl$ nanoparticles at 57.7 nm in water. Similarly, the nanofluid containing $Co_2(OH)_3Cl$ nanoparticles at 11.7 nm displayed a higher viscosity in comparison to that made of $Co_2(OH)_3Cl$ nanoparticles at 9.6 nm due to the narrow size distribution of $Co_2(OH)_3Cl$ nanoparticles at 9.6 nm in water. Clearly, the proposed influence of particle distribution on the nanofluid viscosity is a hypothesis; further experimental verification is needed before a firm conclusion can be reached.

5.2.2 Thermal conductivity of $Co_2(OH)_3Cl$-H_2O nanofluid

In this section, the measured thermal conductivity of different $Co_2(OH)_3Cl$-H_2O nanofluids as a function of temperature is depicted in Figure 5.5. It is shown that the thermal conductivities of $Co_2(OH)_3Cl$-H_2O nanofluids have increased over those of pure water. The impact of $Co_2(OH)_3Cl$ particle size on the thermal conductivity enhancement of $Co_2(OH)_3Cl$-H_2O nanofluids at 308 K is shown in Figure 5.6. The thermal conductivity of nanofluids increases with increasing temperature and decreasing particle size. The highest enhancement in thermal conductivity corresponds to the temperature of 308 K for all $Co_2(OH)_3Cl$ nanofluids. The addition of $Co_2(OH)_3Cl$ nanoparticles at 9.6 nm to water resulted in raising the thermal conductivity of $Co_2(OH)_3Cl$-H_2O nanofluid from ~10% to 14% by increasing the temperature from 298 K to 308 K compared to pure water. The proposed mechanisms explaining the thermal conductivity enhancement of nanofluids include the clustering of nanoparticles, the formation of liquid nanolayer over the nanoparticles and the Brownian motion of nanoparticles (Ganesan et al., 2018; Gupta et al., 2021; Rahman Salari et al., 2022; Manoram and Moorthy, 2022; Khamlich et al., 2023; Lin et al., 2023). Nanoparticles tend to aggregate when the Van der Waals attraction force is greater than the repulsive force. The aggregation of nanoparticles results in clusters formation within the base fluid. Clustered nanoparticles provide paths facilitating heat transport via conduction which may contribute to the enhancement of nanofluid thermal conductivity (Wang et al., 1999).

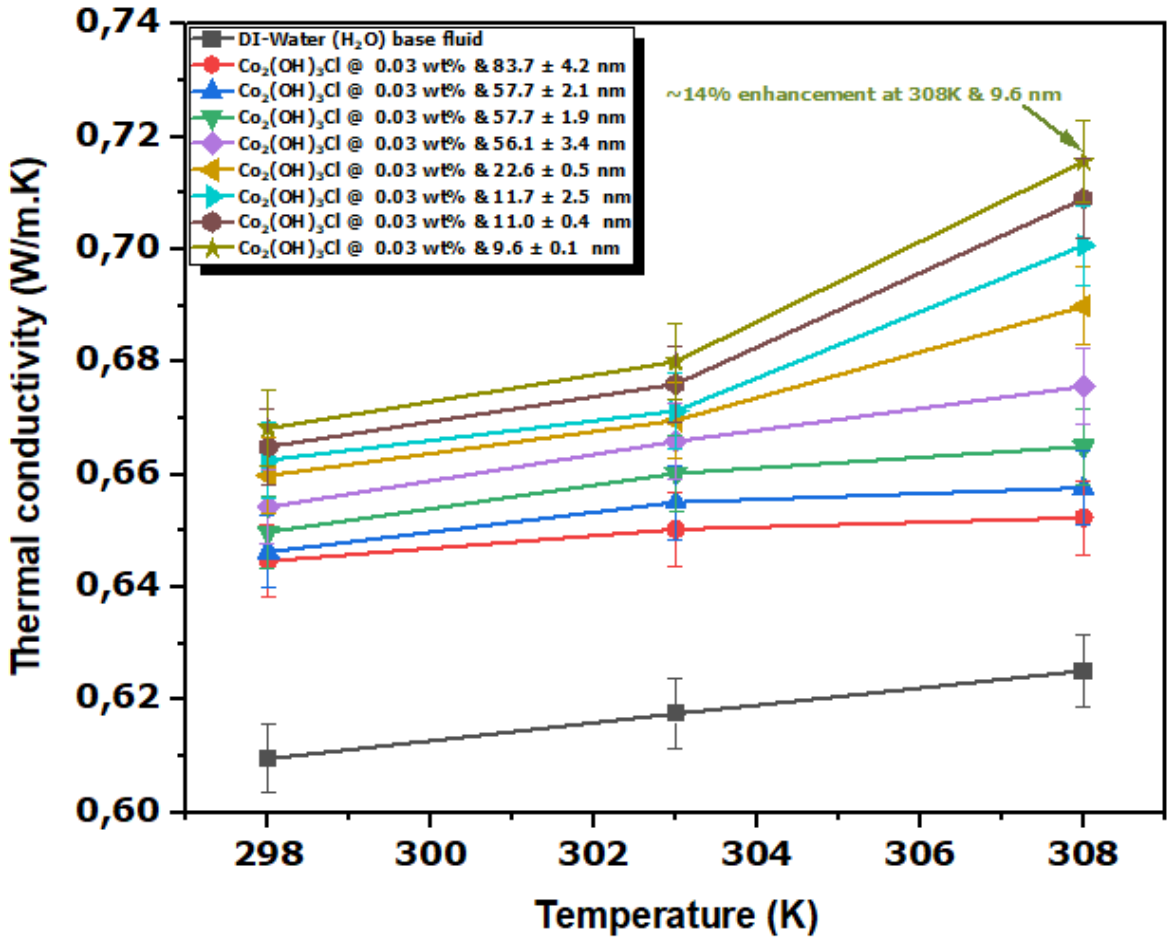

Figure 5.5: Variations of $Co_2(OH)_3Cl$ nanofluids thermal conductivity at different temperatures

Liquid molecules layering at the surface of nanoparticles is also beneficial for enhancing the thermal conductivity enhancement of nanofluids. The layering of liquid molecules creates a thermal bridge between the nanoparticles and the dispersing fluid, resulting in more efficient thermal transport (Murshed et al., 2008). Brownian motion of dispersed nanoparticles is considered an important factor in explaining both particle size and temperature dependence of nanofluid thermal conductivity (Moghadassi et al., 2010; Rahman Salari et al., 2022). Brownian motion occurs when nanoparticles collide with one another and with the base fluid molecules. Through collisions between nanoparticles, the transport of energy between nanoparticles is facilitated. Additionally, the interaction between nanoparticles and liquid molecules also leads to convection of the surrounding base fluid at the nanoscale (Riahi et al., 2020; Lenin et al., 2021). This results in an effective mixing of fluid molecules at high and low temperatures, thereby enhancing thermal energy transfer. The enhanced thermal conductivity of nanofluids may be explained by Brownian motion-induced convection (Bhanvase & Barai, 2021:102-103). In this study, an increment in thermal conductivity enhancement occurred at higher temperature and lower particle size. As temperature rises, the movement of $Co_2(OH)_3Cl$ nanoparticles increases as they gain kinetic energy.

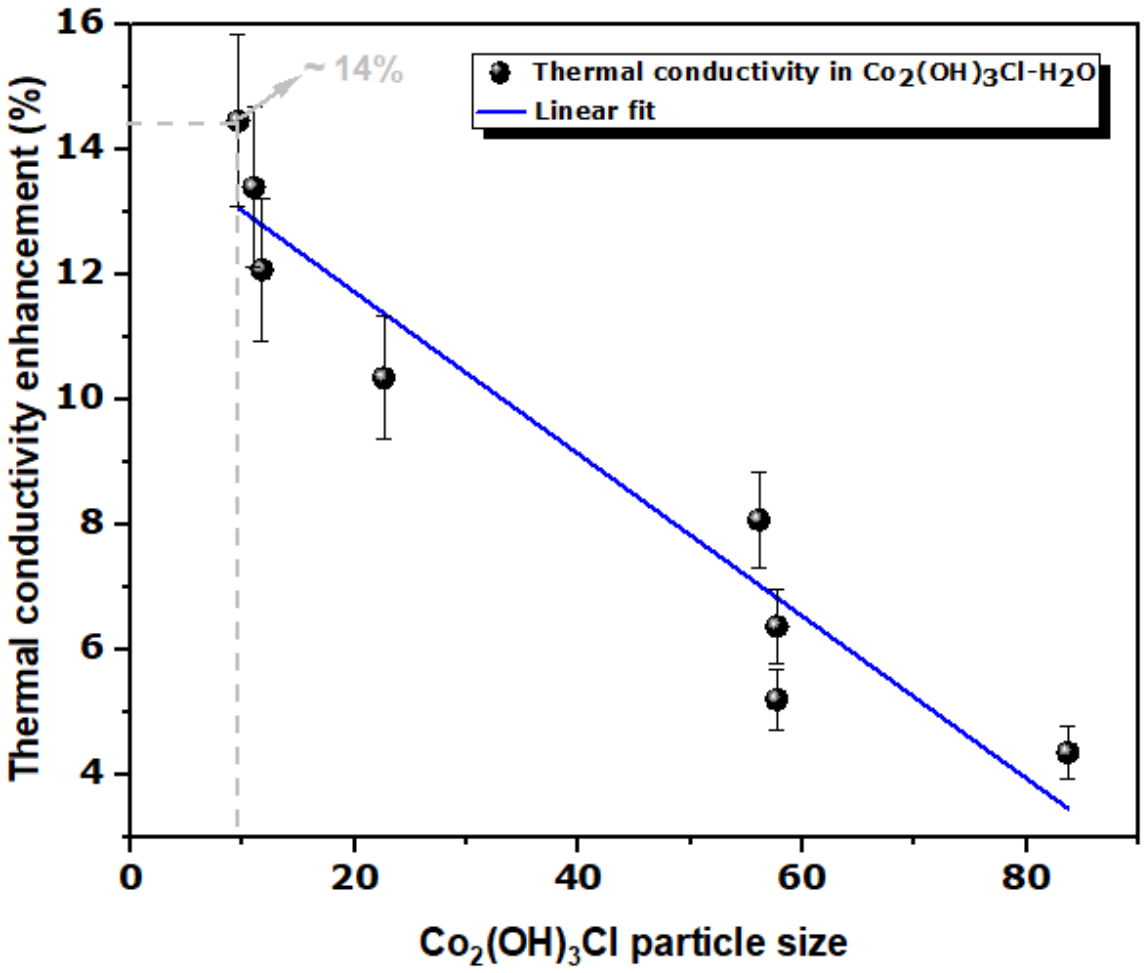

Figure 5.6: Thermal conductivity enhancement of $Co_2(OH)_3Cl$ nanofluids at different particle sizes

As $Co_2(OH)_3Cl$ nanoparticles are more intensely motioned, the contribution of Brownian motion-induced convection to heat transport increases, thereby enhancing thermal conductivity of their nanofluids as reported in previous studies (Murshed et al., 2008; Riahi et al., 2020). At 100% propanol concentration, the smallest size (9.6 nm) of $Co_2(OH)_3Cl$ nanoparticles was produced. Based on the Brownian theory, the smaller the sizes of the colloid particles, the faster the particles move, resulting in increased heat transport inside the fluid (Xuan et al., 2003; Mohammadfam & Zeinali Heris, 2023). Consequently, the incidence of collisions between smaller $Co_2(OH)_3Cl$ nanoparticles and water molecules is expected to increase more significantly, which lead to further thermal conductivity enhancement. Several studies have reported a similar trend regarding the impact of particle size on increasing thermal conductivity of water-based nanofluids. Alloy nanofluids and alumina nanofluids have shown enhanced thermal conductivity with decreasing particle size at 283 K and 303 K (Chopkar et al., 2008; Teng et al., 2010).

5.3 Conclusion

In this study, a variety of propanol concentrations were used to synthesize $Co_2(OH)_3Cl$ nanoparticles of different sizes and shapes, which were then dispersed in pure water at 0.03 wt%. The optical analysis of the nanofluids was presented. A study of the effects of $Co_2(OH)_3Cl$ nanoparticle size and shape on the viscosity and thermal conductivity of their nanofluids was conducted. The viscosity and thermal conductivity of $Co_2(OH)_3Cl$ nanofluids were also studied in relation to temperature. All $Co_2(OH)_3Cl$ nanofluids exhibited a drastic reduction in transmittance compared to water in the visible range, demonstrating their ability to absorb visible light. In addition, the viscosity of water and all nanofluids were measured. The results indicated that the base fluid and nanofluids showed Newtonian behaviour. A rise in temperature resulted in a reduction in the viscosities of $Co_2(OH)_3Cl$ nanofluids whereas their thermal conductivity increased. Most of the viscosities of $Co_2(OH)_3Cl$-H_2O nanofluids have increased over those of pure water at all temperatures. At 303 K, the nanofluid made of $Co_2(OH)_3Cl$ at 57.7 nm displayed the highest increase in viscosity (~11%). In contrast to $Co_2(OH)_3Cl$ nanoparticle size, the shape of $Co_2(OH)_3Cl$ nanoparticles dispersed in water significantly affected their ability to enhance the viscosity of nanofluids. The thermal conductivity of the nanofluid made of $Co_2(OH)_3Cl$ nanoparticles at 9.6 nm exhibited the highest augmentation in thermal conductivity at all temperatures with ~14% at 308 K. The enhanced thermal conductivity of $Co_2(OH)_3Cl$-H_2O nanofluids was attributed to the Brownian motion-induced convection mechanism. Interestingly, the results obtained showed that while the thermal conductivity of the aqueous nanofluids was affected by the $Co_2(OH)_3Cl$ particle size, their viscosity was rather influenced by the $Co_2(OH)_3Cl$ particle shape. Consequently, the use of smaller, spherical $Co_2(OH)_3Cl$ nanofluids has the potential of improving the heat transfer performance of water and minimizing the required pumping power in real situations. Therefore, the nanofluids prepared could serve as a promising alternative to the conventional heat transfer fluid used. The work also showed that the solvent concentration can be used successfully as a simple strategy for controlling particle morphology for scale up production.

CHAPTER 6 CONCLUSIONS AND RECOMMENDATIONS

6.1 Introduction

Nanofluids, consisting of nanoparticle dispersions in conventional heat transfer fluids, have been documented to enhance the thermophysical properties of these fluids. Previous studies have shown that the particle size and shape of Co_3O_4 affect the thermal conductivity and viscosity of the resulting Co_3O_4 based nanofluids. Moreover, it has been demonstrated that the synthesis of Co_3O_4 nanoparticles in the presence of different propanol concentrations can significantly alter their size, thus improving the properties of the resulting nanofluids. Therefore, this study investigated the impact of propanol concentration on the size and shape of $Co_2(OH)_3Cl$ nanoparticles. Additionally, time evolution experiments were conducted in the presence of different solvents concentrations to understand the growth of $Co_2(OH)_3Cl$ nanoparticles. Lastly, the relationship between the $Co_2(OH)_3Cl$ particle size and shape, and the viscosity and thermal conductivity of their nanofluids was investigated.

6.2 Conclusions

The effect of propanol-to-water ratio on particle size, shape and phase was investigated. For solvent concentrations ranging between 0 to 50% propanol, green nanopowder mixtures consisting of $Co_{1.176}(OH)_2Cl_{0.348}(H_2O)_{0.456}$ and $Co_2(OH)_3Cl$ were obtained. For 70 to 100% propanol, β-$Co_2(OH)_3Cl$ was obtained. At 95 and 98% propanol, $Co_2(OH)_3Cl$ nanopowders were pink while at 70 and 100%, lavender coloured $Co_2(OH)_3Cl$ nanopowders were prepared. $Co_2(OH)_3Cl$ nanospheres with a high purity level were produced in the presence of solvents at 70% to 100% propanol concentrations. Additionally, increasing the propanol concentration from 0 to 70% resulted in the production of spherical nanoparticles in lieu of $Co_2(OH)_3Cl$ hexagonal nanoplates. Interestingly, this study found that increasing propanol concentration from 50% to 100% reduced the particle size of $Co_2(OH)_3Cl$ nanospheres unlike the trend reported for the synthesis of rhombic Co_3O_4 particles at 50% and 100% propanol concentrations. The impact of 70% propanol and water on the growth kinetics of the $Co_2(OH)_3Cl$ nanoparticles of varied shapes was also discussed. In water, the $Co_2(OH)_3Cl$ hexagonal nanoplates were converted into nanospheres after 360 min of synthesis, whereas in 70% propanol, only spherical nanoparticles were generated from 60 to 960 min. A propanol-based growth of $Co_2(OH)_3Cl$ nanospheres at reduced reaction times is preferred for producing smaller nanospheres which, in turn can reduce the energy consumption during the synthesis process. The shape of the particle size distribution was linked with the growth mechanism of the $Co_2(OH)_3Cl$ nanoparticles obtained. The water based growth of $Co_2(OH)_3Cl$ nanoplates via the OR then OA mechanisms is presented. A simultaneous OR and OA growth mechanism for $Co_2(OH)_3Cl$ nanospheres in the presence of water was also presented. In contrast, an initial OR growth of $Co_2(OH)_3Cl$ nanospheres then OA from 70% propanol was obtained.

In Chapter 5, the dependence of the $Co_2(OH)_3Cl$-H_2O nanofluid properties on temperature and $Co_2(OH)_3Cl$ particle size and shape were investigated. An augmentation in temperature caused a reduction in the viscosity of $Co_2(OH)_3Cl$-H_2O nanofluids while their thermal conductivity increased. A Brownian motion-induced convection is responsible for the enhanced thermal conductivity of $Co_2(OH)_3Cl$-H_2O nanofluids. The addition of smaller $Co_2(OH)_3Cl$ nanospheres to water favoured the enhancement in nanofluid thermal conductivity. In contrast, adding $Co_2(OH)_3Cl$ nanoplates rather than $Co_2(OH)_3Cl$ nanospheres to water resulted in increasing the nanofluid viscosity.

6.3 Research contributions

This study reported the role of propanol-to-water ratio on the formation and growth mechanism of $Co_2(OH)_3Cl$. It revealed that:

- Particle phase is dependent on the propanol concentration.
- Variations in propanol concentration affect $Co_2(OH)_3Cl$ nanoparticle structural arrangement, size and shape, resulting in colour changes.
- Particle morphology is strongly dependent on the propanol concentration.
- Variation in propanol concentration can give control over $Co_2(OH)_3Cl$ particle sizes.
- The growth kinetics of the $Co_2(OH)_3Cl$ nanospheres is solvent concentration dependent.
- Selective choice of solvent can give control over $Co_2(OH)_3Cl$ particle size.

Interestingly, this study demonstrated how the change in $Co_2(OH)_3Cl$ particle size and shape affected the $Co_2(OH)_3Cl$-H_2O nanofluid properties. It was found that:

- Enhanced thermal conductivity is strongly dependent on the $Co_2(OH)_3Cl$ particle size.
- Increased viscosity is strongly dependent on the $Co_2(OH)_3Cl$ particle shape.

The findings in this study provides insight about the influence of propanol concentration on the growth of $Co_2(OH)_3Cl$ and their properties as nano heat transfer fluid, producing new vital information that will further promote understanding of the formation mechanisms of $Co_2(OH)_3Cl$ growth and their application as heat transfer fluid.

6.4 Future research recommendations

This study was based on propanol concentrations ranging from 0 to 100% and may be refined and enhanced by varying the type of alcohol used. The $Co_2(OH)_3Cl$-H_2O nanofluids used in this study were obtained via the two-step method. Since the stability of nanofluids is the main concern linked to the preparation method, the $Co_2(OH)_3Cl$-H_2O nanofluids prepared in this study should be prepared via a one-step technique such as the laser ablation technique as the stability of nanofluids will likely be enhanced. The impact of $Co_2(OH)_3Cl$ particle size and shape on the properties of their nanofluids has been reported. However, an

investigation of the effect of different $Co_2(OH)_3Cl$ particle concentrations on the nanofluid properties would benefit this study. The addition of $Co_2(OH)_3Cl$ nanoparticles to different heat transfer fluids should be carried out to evaluate the properties of the ensuing nanofluids. The $Co_2(OH)_3Cl$-H_2O nanofluids prepared in this study should be evaluated first in a nanofluid absorption system under simulated sunlight then in an actual solar thermal system.

REFERENCES

Abed, N., Afgan, I., Cioncolini, A., Iacovides, H. & Nasser, A. 2020. Assessment and evaluation of the thermal performance of various working fluids in parabolic trough collectors of solar thermal power plants under non-uniform heat flux distribution conditions. *Energies*, 13(15): 3776.

Ackerson, B.J. 1991. Shear induced order in equilibrium colloidal liquids. *Physica A: Statistical Mechanics and its Applications*, 174(1): 15–30.

Agarwal, D.K., Vaidyanathan, A. & Sunil Kumar, S. 2015. Investigation on convective heat transfer behaviour of kerosene-Al_2O_3 nanofluid. *Applied Thermal Engineering*, 84: 64–73.

Aghazadeh, M., Dalvand, S. & Hosseinifard, M. 2014. Facile electrochemical synthesis of uniform β-$Co(OH)_2$ nanoplates for high performance supercapacitors. *Ceramics International*, 40(2): 3485–3493.

Ahmadi, M.H., Mirlohi, A., Alhuyi Nazari, M. & Ghasempour, R. 2018. A review of thermal conductivity of various nanofluids. *Journal of Molecular Liquids*, 265: 181–188.

Akoh, H., Tsukasaki, Y., Yatsuya, S. & Tasaki, A. 1978. Magnetic properties of ferromagnetic ultrafine particles prepared by vacuum evaporation on running oil substrate. *Journal of Crystal Growth*, 45: 495–500.

Alam, T., Balam, N. B., Kulkarni, K. S., Siddiqui, M. I. H., Kapoor, N. R., Meena, C. S., Kumar, A., & Cozzolino, R. 2021. Performance augmentation of the flat plate solar thermal collector: a review. *Energies,* 14(19), 6203.

Ali, H.M., Babar, H., Shah, T.R., Sajid, M.U., Qasim, M.A. & Javed, S. 2018. Preparation techniques of TiO_2 nanofluids and challenges: a review. *Applied Sciences*, 8(4): 587.

Ali, N., Teixeira, J.A. & Addali, A. 2018. A review on nanofluids: fabrication, stability, and thermophysical properties. *Journal of Nanomaterials*, 2018.

Aligholami, M., Akbari, M. & Maaza, M. 2023. Thermal performance of copper-distilled water nanofluid in a wavy channel. *Materials Today: Proceedings*.

Alsboul, M., Ghazali, M.S.M., Gomaa, M.R. & Albani, A. 2022. Experimental and theoretical investigation of the thermophysical properties of cobalt oxide (Co_3O_4) in distilled water (DW), ethylene glycol (EG), and DW-EG mixture nanofluids. *Nanomaterials*, 12(16): 2779.

Anoop, K.B., Sundararajan, T. & Das, S.K. 2009. Effect of particle size on the convective heat transfer in nanofluid in the developing region. *International Journal of Heat and Mass Transfer*, 52(9–10): 2189–2195.

Ansari, S., Hussain, T., Yahya, S.M., Chaturvedi, P. & Sardar, N. 2018. Experimental investigation of viscosity of nanofluids containing oxide nanoparticles at varying shear rate. *Journal of Nanofluids*, 7(6): 1075–1080.

Athawale, A.A., Majumdar, M., Singh, H. & Navinkiran, K. 2010. Synthesis of cobalt oxide nanoparticles/fibres in alcoholic medium using γ-ray technique. *Defence Science Journal*, 60(5): 507–513.

Azizian, R., Doroodchi, E. & Moghtaderi, B. 2016. Influence of controlled aggregation on thermal conductivity of nanofluids. *Journal of Heat Transfer*, 138(2).

Baratpour, M., Karimipour, A., Afrand, M. & Wongwises, S. 2016. Effects of temperature and concentration on the viscosity of nanofluids made of single-wall carbon nanotubes in ethylene glycol. *International Communications in Heat and Mass Transfer*, 74: 108–113.

Batchelor, G.K. 1977. The effect of Brownian motion on the bulk stress in a suspension of spherical particles. *Journal of Fluid Mechanics*, 83(1): 97–117.

Beck, M.P., Yuan, Y., Warrier, P. & Teja, A.S. 2009. The effect of particle size on the thermal conductivity of alumina nanofluids. *Journal of Nanoparticle Research*, 11(5): 1129–1136.

Bejan, A. & Kraus, A.D. 2003. *Heat Transfer Handbook*. John Wiley & Sons.

Bhalla, V. & Tyagi, H. 2017. Solar energy harvesting by cobalt oxide nanoparticles, a nanofluid absorption based system. *Sustainable Energy Technologies and Assessments*, 24: 45–54.

Bhanvase, B.A. & Barai, Divya. 2021. *Nanofluids for Heat and Mass Transfer: : Fundamentals, Sustainable Manufacturing and Applications*. Academic Press.

Brinkman, H.C. 2004. The viscosity of concentrated suspensions and solutions. *The Journal of Chemical Physics*, 20(4): 571.

Campbell, C.T., Parker, S.C. & Starr, D.E. 2002. The effect of size-dependent nanoparticle energetics on catalyst sintering. *Science*, 298(5594): 811–814.

Cao, Y., Yuan, F., Yao, M., Bang, J.H. & Lee, J.H. 2014. A new synthetic route to hollow Co_3O_4 octahedra for supercapacitor applications. *CrystEngComm*, 16(5): 826–833.

Chakraborty, S. & Panigrahi, P.K. 2020. Stability of nanofluid: a review. *Applied Thermal Engineering*, 174: 115259.

Chakraborty, S., Sarkar, I., Ashok, A., Sengupta, I., Pal, S.K. & Chakraborty, S. 2018. Thermo-physical properties of Cu-Zn-Al LDH nanofluid and its application in spray cooling. *Applied Thermal Engineering*, 141: 339–351.

Chakraborty, S., Sarkar, I., Haldar, K., Pal, S.K. & Chakraborty, S. 2015. Synthesis of Cu-Al layered double hydroxide nanofluid and characterization of its thermal properties. *Applied Clay Science*, 107: 98–108.

Chamsa-ard, W., Brundavanam, S., Fung, C.C., Fawcett, D. & Poinern, G. 2017. Nanofluid types, their synthesis, properties and incorporation in direct solar thermal collectors: a review. *Nanomaterials*, 7(6): 131.

Chang, H., Jwo, C.S., Fan, P.S. & Pai, S.H. 2007. Process optimization and material properties for nanofluid manufacturing. *International Journal of Advanced Manufacturing Technology*, 34: 300–306.

Chatterjee, A., Verma, R., Umashankar, H.P., Kasthurirengan, S., Shivaprakash, N.C. & Behera, U. 2019. Heat conduction model based on percolation theory for thermal conductivity of composites with high volume fraction of filler in base matrix. *International Journal of Thermal Sciences*, 136: 389–395.

Chen, G., Yu, W., Singh, D., Cookson, D. & Routbort, J. 2008. Application of SAXS to the study of particle-size-dependent thermal conductivity in silica nanofluids. *Journal of Nanoparticle Research*, 10(7): 1109–1114.

Chen, H. & Ding, Y. 2009. Heat transfer and rheological behaviour of nanofluids – a review. In Wang, L. (eds). *Advances in Transport Phenomena*, vol 1. Springer, Berlin, Heidelberg.

Chen, H., Yang, W., He, Y., Ding, Y., Zhang, L., Tan, C., Lapkin, A.A. & Bavykin, D. V. 2008. Heat transfer and flow behaviour of aqueous suspensions of titanate nanotubes (nanofluids). *Powder Technology*, 183(1): 63–72.

Chen, L. & Xie, H. 2010. Surfactant-free nanofluids containing double- and single-walled carbon nanotubes functionalized by a wet-mechanochemical reaction. *Thermochimica Acta*, 497(1–2): 67–71.

Chen, L., Xie, H., Li, Y. & Yu, W. 2008. Nanofluids containing carbon nanotubes treated by mechanochemical reaction. *Thermochimica Acta*, 477(1–2): 21–24.

Chen, L., Xie, H., Yu, W. & Li, Y. 2011. Rheological behaviors of nanofluids containing multi-walled carbon nanotube. *Journal of Dispersion Science and Technology*, 32(4): 550–554.

Chevalier, J., Tillement, O. & Ayela, F. 2007. Rheological properties of nanofluids flowing through microchannels. *Applied Physics Letters*, 91(23).

Chhabra, R.P. & Richardson, J.F. 1999. Non-Newtonian fluid behaviour. In *Non-Newtonian Flow in the Process Industries: fundamentals and engineering applications*. Butterworth-Heinemann.

Choi, S.U.S. & Eastman, J. 1995. Enhancing thermal conductivity of fluids with nanoparticles. In *American Society of Mechanical Engineers, Fluids Engineering Division (Publication) FED*. 99–105.

Chopkar, I., Sudarshan, S., Das, P.K. & Manna, I. 2008. Effect of particle size on thermal conductivity of nanofluid. *Metallurgical and Materials Transactions A: Physical Metallurgy and Materials Science*, 39(7): 1535–1542.

Chopkar, M., Das, P.K. & Manna, I. 2006. Synthesis and characterization of nanofluid for advanced heat transfer applications. *Scripta Materialia*, 55(6): 549–552.

Choudhary, R., Khurana, D., Kumar, A. & Subudhi, S. 2017. Stability analysis of Al_2O_3/water nanofluids. *Journal of Experimental Nanoscience*, 12(1): 140–151.

Chow, T.S. 1993. Viscosities of concentrated dispersions. *Physical Review E*, 48(3): 1977–1983.

Chowdhury, M., Fester, V. & Kale, G. 2014. Growth kinetics evaluation of hydrothermally synthesized β-FeOOH nanorods. *Journal of Crystal Growth*, 387: 57–65.

Chowdhury, M.R., Fester, V., Kale, G. & Cespedes, O. 2014. Hydrothermal precipitation of β-FeOOH nanostructure(s) in mixed solvent: Study of their morphological and structural evolution. *Journal of Nanoparticle Research*, 16(5): 1–11.

Colla, L., Fedele, L., Scattolini, M. & Bobbo, S. 2012. Water-based Fe_2O_3 nanofluid characterization: thermal conductivity and viscosity measurements and correlation. *Advances in Mechanical Engineering*, 2012.

Cui, H., Zayat, M. & Levy, D. 2009. A chemical strategy to control the shape of oxide nanoparticles. *Journal of Nanoparticle Research*, 11(6): 1331–1338.

Cushing, B.L., Kolesnichenko, V.L. & O'Connor, C.J. 2004. Recent advances in the liquid-phase synthesis of inorganic nanoparticles. *Chemical Reviews*, 104(9): 3893–3946.

Dalmaschio, C.J., Ribeiro, C. & Leite, E.R. 2010. Impact of the colloidal state on the oriented attachment growth mechanism. *Nanoscale*, 2(11): 2336–2345.

Das, S., Choi, S., Yu, W. & Pradeep, T. 2008. *Nanofluids: science and technology*. John Wiley & Sons, Inc.

de Wolff, P.M. 1953. The crystal structure of $Co_2(OH)_3Cl$. *Acta Crystallographica*, 6(4): 359–360.

Denis, C.J., Tighe, C.J., Gruar, R.I., Makwana, N.M. & Darr, J.A. 2015. Nucleation and growth of cobalt oxide nanoparticles in a continuous hydrothermal reactor under laminar and turbulent flow. *Crystal Growth and Design*, 15(9): 4256–4265.

Devendiran, D.K. & Amirtham, V.A. 2016. A review on preparation, characterization, properties and applications of nanofluids. *Renewable and Sustainable Energy Reviews*, 60: 21–40.

Dharmalingam, R., Sivagnanaprabhu, K. K., Senthil Kumar, B., & Thirumalai, R. 2014. Nano materials and nanofluids: an Innovative technology study for new paradigms for technology enhancement. *Procedia Engineering*, *97*, 1434–1441.

Domingues, G., Volz, S., Joulain, K. & Greffet, J.J. 2005. Heat transfer between two nanoparticles through near field interaction. *Physical Review Letters*, 94(8).

Drotning, W.D. 1978. Optical properties of solar-absorbing oxide particles suspended in a molten salt heat transfer fluid. *Solar Energy*, 20(4): 313–319.

Einstein, A. 1906. Eine neue bestimmung der molekül-dimension (A determination of the molecular dimensions). *Annalen der Physik*, 324(2): 289–306.

Esfe, M.H. & Saedodin, S. 2014. An experimental investigation and new correlation of viscosity of ZnO-EG nanofluid at various temperatures and different solid volume fractions. *Experimental Thermal and Fluid Science*, 55: 1–5.

Esfe, M.H., Saedodin, S., Mahian, O. & Wongwises, S. 2014. Efficiency of ferromagnetic nanoparticles suspended in ethylene glycol for applications in energy devices: effects of particle size, temperature, and concentration. *International Communications in Heat and Mass Transfer*, 58: 138–146.

Esmaeilzadeh, E., Almohammadi, H., Nasiri Vatan, S. & Omrani, A.N. 2013. Experimental investigation of hydrodynamics and heat transfer characteristics of γ-Al_2O_3/water under laminar flow inside a horizontal tube. *International Journal of Thermal Sciences*, 63: 31–37.

Evangelisti, L., De Lieto Vollaro, R. & Asdrubali, F. 2019. Latest advances on solar thermal collectors: A comprehensive review. *Renewable and Sustainable Energy Reviews*, 114: 109318.

Fanney, A.H. & Klein, S.A. 1988. Thermal performance comparisons for solar hot water systems subjected to various collector and heat exchanger flow rates. *Solar Energy*, 40(1): 1–11.

Fazlali, A., Lashkarara, S. & Mohammadi, A.H. 2012. Rheological properties of paraffin-based Co_3O_4 nano-ferrofluid. *Advances in Nanotechnology*, 11: 88298190.

Feitknecht, W. & Fischer, G. 1935. On the chemistry and morphology of basic salts of divalent metals III. About basic cobalt chlorides. (X. Communication on basic salts). *Helvetica Chimica Acta*, 18(1): 555–569.

Feitknecht, W. 1935. On the chemistry and morphology of the basic salts of divalent metals I. General considerations. (VIII. Communication on basic salts). *Helvetica Chimica Acta*, 18(1): 28–40.

Feng, J. & Zeng, H.C. 2003. Size-controlled growth of Co_3O_4 nanocubes. *Chemistry of Materials*, 15(14): 2829–2835.

Fester, V., Slatter, P., Alderman, N.J. & Alderman, N. 2012. Resistance coefficients for non-Newtonian flows in pipe fittings. In *Rheology*. 151–186.

Fuchigami, T., Kimata, R., Haneda, M. & Kakimoto, K.I. 2020. Growth mechanism and CO oxidation catalytic activity of raspberry-shaped Co_3O_4 nanoparticles. *Journal of the Ceramic Society of Japan*, 128(5): 291–297.

Funk, J.E. & Dinger, D.R. 1994. Viscosity and Rheology. In *Predictive Process Control of Crowded Particulate Suspensions*. Springer, Boston, MA: 235–252.

Ganguli, S., Koppisetti, H.V.S.R.M., Ghosh, S., Biswas, T. & Mahalingam, V. 2019. Paradoxical observance of ‘intrinsic’ and ‘geometric’ oxygen evolution electrocatalysis in phase-tuned cobalt oxide/hydroxide nanoparticles. *ACS Applied Nano Materials*, 2(12): 7957–7968.

García-Martínez, O., Millán, P., Rojas, R.M. & Torralvo, M.J. 1988. Cobalt basic salts as inorganic precursors of cobalt oxides and cobalt metal: thermal behaviour dependence on experimental conditions. *Journal of Materials Science*, 23(4): 1334–1350.

Geankoplis, C. 2003. *Transport processes and separation process principles:(includes unit operations)*. 3rd ed.

Ghadimi, A., Saidur, R. & Metselaar, H.S.C. 2011. A review of nanofluid stability properties and characterization in stationary conditions. *International Journal of Heat and Mass Transfer*, 54(17–18): 4051–4068.

Ghobadi, N. 2013. Band gap determination using absorption spectrum fitting procedure. *International Nano Letters*, 3(1): 1–4.

Ghosh, M.M., Ghosh, S. & Pabi, S.K. 2013. Effects of particle shape and fluid temperature on heat-transfer characteristics of nanofluids. *Journal of Materials Engineering and Performance*, 22(6): 1525–1529.

Godson, L., Raja, B., Mohan Lal, D. & Wongwises, S. 2010. Enhancement of heat transfer using nanofluids—an overview. *Renewable and Sustainable Energy Reviews*, 14(2): 629–641.

Goharshadi, E.K., Ahmadzadeh, H., Samiee, S. & Hadadian, M. 2013. Nanofluids for heat transfer enhancement-a review. *Physical Chemistry Research*, 1(1): 1–33.

Gondal, M.A., Ilyas, A.M., Fasasi, T.A., Dastageer, M.A., Seddigi, Z.S., Qahtan, T.F., Faiz, M. & Khattak, G.D. 2015. Synthesis of green TiO_2/ZnO/CdS hybrid nano-catalyst for efficient light harvesting using an elegant pulsed laser ablation in liquids method. *Applied Surface Science*, 357: 2217–2222.

Green, A.A. & Hersam, M.C. 2010. Emerging methods for producing monodisperse graphene dispersions. *Journal of Physical Chemistry Letters*, 1(2): 544–549.

Gu, B., Hou, B., Lu, Z., Wang, Z. & Chen, S. 2013. Thermal conductivity of nanofluids containing high aspect ratio fillers. *International Journal of Heat and Mass Transfer*, 64: 108–114.

Gulicovski, J.J., Čerović, L.S. & Milonjić, S.K. 2008. Point of zero charge and isoelectric point of alumina. In *Materials and Manufacturing Processes*. Taylor & Francis Group.

Guo, W., Li, G., Zheng, Y. & Dong, C. 2018. Measurement of the thermal conductivity of SiO_2 nanofluids with an optimized transient hot wire method. *Thermochimica Acta*, 661: 84–97.

Gupta, H.K., Agrawal, G. Das & Mathur, J. 2015. An experimental investigation of a low temperature Al_2O_3-H_2O nanofluid based direct absorption solar collector. *Solar Energy*, 118: 390–396.

Gupta, V., Sharma, S., Magotra, U. & Sharma, M. 2021. Concentration and temperature dependent effects on acoustical parameters and thermal conductivity in cobalt oxide nanofluids. *Protection of Metals and Physical Chemistry of Surfaces*, 57(6): 1198–1205.

Hajian, R., Layeghi, M. & Abbaspour Sani, K. 2012. Experimental study of nanofluid effects on the thermal performance with response time of heat pipe. *Energy Conversion and Management*, 56: 63–68.

Hamilton, R.L. & Crosser, O.K. 1962. Thermal conductivity of heterogeneous two-component systems. *Industrial and Engineering Chemistry Fundamentals*, 1(3): 187–191.

He, T., Chen, D. & Jiao, X. 2004. Controlled Synthesis of Co_3O_4 nanoparticles through Oriented Aggregation. *Chemistry of Materials*, 16(4): 737–743.

He, T., Chen, D., Jiao, X., Xu, Y. & Gu, Y. 2004. Surfactant-assisted solvothermal synthesis of Co_3O_4 hollow spheres with oriented-aggregation nanostructures and tunable particle size. *Langmuir*, 20(19): 8404–8408.

He, Y., Jin, Y., Chen, H., Ding, Y., Cang, D. & Lu, H. 2007. Heat transfer and flow behaviour of aqueous suspensions of TiO_2 nanoparticles (nanofluids) flowing upward through a vertical pipe. *International Journal of Heat and Mass Transfer*, 50(11–12): 2272–2281.

He, Y.T., Wan, J. & Tokunaga, T. 2008. Kinetic stability of hematite nanoparticles: The effect of particle sizes. *Journal of Nanoparticle Research*, 10(2): 321–332.

Hemmati-Sarapardeh, A., Varamesh, A., Husein, M.M. & Karan, K. 2018. On the evaluation of the viscosity of nanofluid systems: modelling and data assessment. *Renewable and Sustainable Energy Reviews*, 81: 313–329.

Heuvel, W., Sone, B. & Fester, V. 2021. Effect of cobalt complexes on cobalt oxide particles for the activation of peroxymonosulphate in textile wastewater treatment. *International Journal of Environmental Science and Technology*: 1–16.

Hong, R.Y., Ren, Z.Q., Han, Y.P., Li, H.Z., Zheng, Y. & Ding, J. 2007. Rheological properties of water-based Fe_3O_4 ferrofluids. *Chemical Engineering Science*, 62(21): 5912–5924.

Hong, T.K., Yang, H.S. & Choi, C.J. 2005. Study of the enhanced thermal conductivity of Fe nanofluids. *Journal of Applied Physics*, 97(6).

Höök, M. & Tang, X. 2013. Depletion of fossil fuels and anthropogenic climate change-a review. *Energy Policy*, 52: 797–809.

Hosseini, S.M., Ghasemi, E., Fazlali, A. & Henneke, D.E. 2012. The effect of nanoparticle concentration on the rheological properties of paraffin-based Co_3O_4 ferrofluids. *Journal of Nanoparticle Research*, 14(7): 1–7.

Huang, F., Zhang, H. & Banfieldt, J.F. 2003. Two-stage crystal-growth kinetics observed during hydrothermal coarsening of nanocrystalline ZnS. *Nano Letters*, 3(3): 373–378.

Huang, X., Zhang, X. & Qing, S. 2024. The function of nano layer in enhancing the thermal conductivity of TiO_2/water nanofluids. *Thermal Science*, (00): 15–15.

Huxtable, S.T., Cahill, D.G., Shenogin, S., Xue, L., Ozisik, R., Barone, P., Usrey, M., Strano, M.S., Siddons, G., Shim, M. & Keblinski, P. 2003. Interfacial heat flow in carbon nanotube suspensions. *Nature Materials*, 2(11): 731–734.

Ilyas, S.U., Pendyala, R. & Marneni, N. 2013. Settling characteristics of alumina nanoparticles in ethanol-water mixtures. In *Applied Mechanics and Materials*. Trans Tech Publications Ltd.

Ilyas, S.U., Pendyala, R. & Marneni, N. 2017. Stability of nanofluids. In Korada, V.S. & Hamid, N.H. (eds). *Engineering Applications of Nanotechnology*. Springer International Publishing.

Jana, S., Salehi-Khojin, A., & Zhong, W. H. 2007. Enhancement of fluid thermal conductivity by the addition of single and hybrid nano-additives. *Thermochimica Acta*, *462*(1–2), 45–55.

Jarahnejad, M., Haghighi, E.B., Saleemi, M., Nikkam, N., Khodabandeh, R., Palm, B., Toprak, M.S. & Muhammed, M. 2015. Experimental investigation on viscosity of water-based Al_2O_3 and TiO_2 nanofluids. *Rheologica Acta*, 54(5): 411–422.

Jeong, J., Li, C., Kwon, Y., Lee, J., Kim, S.H. & Yun, R. 2013. Particle shape effect on the viscosity and thermal conductivity of ZnO nanofluids. *International Journal of Refrigeration*, 36(8): 2233–2241.

Jiang, H., He, Q., Li, X., Su, X., Zhang, Y., Chen, S., Zhang, S., Zhang, G., Jiang, J., Luo, Y., Ajayan, P.M. & Song, L. 2019. Tracking structural self-reconstruction and identifying true active sites toward cobalt oxychloride precatalyst of oxygen evolution reaction. *Advanced Materials*, 31(8): 1805127.

Jiang, L., Gao, L. & Sun, J. 2003. Production of aqueous colloidal dispersions of carbon nanotubes. *Journal of Colloid and Interface Science*, 260(1): 89–94.

Joesten, R.L. & Kerrick, D.M. 1991. Kinetics of coarsening and diffusion-controlled mineral growth. In *Journal of Applied Physics*. 4976–4980.

Jolivet, J.P., Henry, M. & Livage, J. 2000. *Metal oxide chemistry and synthesis : from solution to solid state*. John Wiley.

Kamila, S. & Venugopal, V.R. 2019. Acoustics and rheological studies of aqueous ethylene glycol blend copper oxide nanofluids. *Particulate Science and Technology*, 37(2): 131–140.

Kanie, K., Tsujikawa, Y. & Muramatsu, A. 2017. Direct hydrothermal synthesis of size-controlled Co_3O_4 Nanocubes under highly condensed conditions. *Materials Transactions*, 58(7): 1014–1019.

Karimi-Nazarabad, M., Goharshadi, E.K., Entezari, M.H. & Nancarrow, P. 2015. Rheological properties of the nanofluids of tungsten oxide nanoparticles in ethylene glycol and glycerol. *Microfluidics and Nanofluidics*, 19(5): 1191–1202.

Kashchiev, D. & Van Rosmalen, G.M. 2003. Review: nucleation in solutions revisited. *Crystal Research and Technology*, 38(7–8): 555–574.

Kashchiev, D. 1982. On the relation between nucleation work, nucleus size, and nucleation rate. *The Journal of Chemical Physics*, 76(10): 5098–5102.

Kaszuba, M., Corbett, J., Watson, F.M.N. & Jones, A. 2010. High-concentration zeta potential measurements using light-scattering techniques. *Philosophical Transactions of the Royal Society A: Mathematical, Physical and Engineering Sciences*, 368(1927): 4439–4451.

Katiyar, A., Dhar, P., Nandi, T. & Das, S.K. 2016. Magnetic field induced augmented thermal conduction phenomenon in magneto-nanocolloids. *Journal of Magnetism and Magnetic Materials*, 419: 588–599.

Keblinski, P., Phillpot, S.R., Choi, S.U.S. & Eastman, J.A. 2002. Mechanisms of heat flow in suspensions of nano-sized particles (nanofluids). *International Journal of Heat and Mass Transfer*, 45(4): 855–863.

Khamlich, S., Jakobi, J., Khamliche, T., Ismail, F., Nemraoui, O., Rehbock, C., Fester, V. & Barcikowski, S. 2023. Enhanced heat transfer of laser-fabricated copper nanofluid at ultra-low concentration driven by the nanoparticle surface area. *Journal of Molecular Liquids*, 383: 122104.

Khamlich, S., Manikandan, E., Ngom, B.D., Sithole, J., Nemraoui, O., Zorkani, I., McCrindle, R., Cingo, N. & Maaza, M. 2011. Synthesis, characterization, and growth mechanism of α-Cr_2O_3 monodispersed particles. *Journal of Physics and Chemistry of Solids*, 72(6): 714–718.

Khamlich, S., McCrindle, R., Nuru, Z. Y., Cingo, N., & Maaza, M. 2013. Annealing effect on the structural and optical properties of Cr/α-Cr_2O_3 monodispersed particles based solar absorbers. *Applied Surface Science*, *265*, 745–749.

Khamlich, S., Nemraoui, O., Mongwaketsi, N., McCrindle, R., Cingo, N., & Maaza, M. 2012. Black Cr/α-Cr_2O_3 nanoparticles based solar absorbers. *Physica B: Condensed Matter*, *407*(10), 1509–1512.

Khullar, V., Tyagi, H., Hordy, N., Otanicar, T.P., Hewakuruppu, Y., Modi, P. & Taylor, R.A. 2014. Harvesting solar thermal energy through nanofluid-based volumetric absorption systems. *International Journal of Heat and Mass Transfer*, 77: 377–384.

Khullar, V., Tyagi, H., Otanicar, T.P., Phelan, P.E., Singh, H. & Taylor, R.A. 2012. Solar energy harvesting using nanofluids-based concentrating solar collector. In *ASME 2012 3rd International Conference on Micro/Nanoscale Heat and Mass Transfer, MNHMT 2012*. American Society of Mechanical Engineers Digital Collection: 259–267.

Kim, H.J., Lee, S.H., Lee, J.H. & Jang, S.P. 2015. Effect of particle shape on suspension stability and thermal conductivities of water-based bohemite alumina nanofluids. *Energy*, 90: 1290–1297.

Kirchner, H.O.K. 1971. Coarsening of grain-boundary precipitates. *Metallurgical Transactions*, 2(10): 2861–2864.

Kleinstreuer, C. & Feng, Y. 2011. Experimental and theoretical studies of nanofluid thermal conductivity enhancement: A review. *Nanoscale Research Letters*, 6(1).

Kole, M. & Dey, T.K. 2010. Viscosity of alumina nanoparticles dispersed in car engine coolant. *Experimental Thermal and Fluid Science*, 34(6): 677–683.

Kole, M. & Dey, T.K. 2012. Effect of prolonged ultrasonication on the thermal conductivity of ZnO-ethylene glycol nanofluids. *Thermochimica Acta*, 535: 58–65.

Kong, L., Sun, J. & Bao, Y. 2017. Preparation, characterization and tribological mechanism of nanofluids. *RSC Advances*, 7(21): 12599–12609.

Kupfer, B., Majhi, K., Keller, D.A., Bouhadana, Y., Rühle, S., Barad, H.N., Anderson, A.Y. & Zaban, A. 2015. Thin film Co_3O_4/TiO_2 heterojunction solar cells. *Advanced Energy Materials*, 5(1): 1401007.

Kwek, D., Crivoi, A. & Duan, F. 2010. Effects of temperature and particle size on the thermal property measurements of Al_2O_3-water nanofluids. *Journal of Chemical and Engineering Data*, 55(12): 5690–5695.

Lee, J., Yang, J., Kwon, S.G. & Hyeon, T. 2016. Nonclassical nucleation and growth of inorganic nanoparticles. *Nature Reviews Materials*, 1(8).

Lee, J.H., Hwang, K.S., Jang, S.P., Lee, B.H., Kim, J.H., Choi, S.U.S. & Choi, C.J. 2008. Effective viscosities and thermal conductivities of aqueous nanofluids containing low volume concentrations of Al_2O_3 nanoparticles. *International Journal of Heat and Mass Transfer*, 51(11–12): 2651–2656.

Leite, E.R., Giraldi, T.R., Pontes, F.M., Longo, E., Beltrán, A. & Andrés, J. 2003. Crystal growth in colloidal tin oxide nanocrystals induced by coalescence at room temperature. *Applied Physics Letters*, 83(8): 1566–1568.

Lemes, M.A., Rabelo, D. & De Oliveira, A.E. 2017. A novel method to evaluate nanofluid stability using multivariate image analysis. *Analytical Methods*, 9(39): 5826–5833.

Lenert, A. & Wang, E.N. 2012. Optimization of nanofluid volumetric receivers for solar thermal energy conversion. *Solar Energy*, 86(1): 253–265.

Lenin, R., Joy, P. A., & Bera, C. 2021. A review of the recent progress on thermal conductivity of nanofluid. *Journal of Molecular Liquids*, *338*, 116929.

Leong, K.Y., Najwa, Z.A., Ku Ahmad, K.Z. & Ong, H.C. 2017. Investigation on stability and optical properties of titanium dioxide and aluminium oxide water-based nanofluids. *International Journal of Thermophysics*, 38(5): 77.

Levy, F.L. 1981. A modified Maxwell-Eucken equation for calculating the thermal conductivity of two-component solutions or mixtures. *International Journal of Refrigeration*, 4(4): 223–225.

Li, C.H. & Peterson, G.P. 2007. The effect of particle size on the effective thermal conductivity of Al_2O_3-water nanofluids. *Journal of Applied Physics*, 101(4): 044312.

Li, D., Hong, B., Fang, W., Guo, Y., & Lin, R. 2010. Preparation of well-dispersed silver nanoparticles for oil-based nanofluids. *Industrial and Engineering Chemistry Research*, *49*(4), 1697–1702.

Li, H., Hao, X., Gong, H., Jin, Z. & Zhao, T. 2021. Efficient hydrogen production at a rationally designed $MoSe_2@Co_3O_4$ p-n heterojunction. *Journal of Colloid and Interface Science*, 586: 84–94.

Li, X., Zeng, G. & Lei, X. 2020. The stability, optical properties and solar-thermal conversion performance of SiC-MWCNTs hybrid nanofluids for the direct absorption solar collector (DASC) application. *Solar Energy Materials and Solar Cells*, 206: 110323.

Liang, R., Ma, L., Zhang, J. & Zhao, D. 2011. Theoretical and experimental investigation of the filled-type evacuated tube solar collector with U tube. *Solar Energy*, 85(9): 1735–1744.

Liang, R., Zhang, B., Du, Y., Han, X., Li, S. & Xu, P. 2023. Understanding the anion effect of basic cobalt salts for the electrocatalytic oxygen evolution reaction. *ACS Catalysis*, 13(13): 8821–8829.

Lin, H., Jian, Q., Bai, X., Li, D., Huang, Z., Huang, W., Feng, S. & Cheng, Z. 2023. Recent advances in thermal conductivity and thermal applications of graphene and its derivatives nanofluids. *Applied Thermal Engineering*, 218: 119176.

Liu, B. & Zeng, H.C. 2005. Symmetric and asymmetric Ostwald ripening in the fabrication of homogeneous core-shell semiconductors. *Small*, 1(5): 566–571.

Liu, F., Zhao, B., Wu, W., Yang, H., Ning, Y., Lai, Y. & Bradley, R. 2018. Low cost, robust, environmentally friendly geopolymer–mesoporous carbon composites for efficient solar powered steam generation. *Advanced Functional Materials*, 28(47): 1803266.

Liu, X.D., Hagihala, M., Zheng, X.G., Tao, W.J., Meng, D.D., Zhang, S.L. & Guo, Q.X. 2011. Trimeric hydrogen bond in geometrically frustrated hydroxyl cobalt halogenides. *Chinese Physics Letters*, 28(1): 017803.

Liu, X.D., Meng, D.D., Hagihala, M., Zheng, X.G. & Guo, Q. 2011. Raman and mid-infrared spectroscopic study of geometrically frustrated hydroxyl cobalt halides at room temperature. *Chinese Physics B*, 20(7): 077801.

Lu, W.Q. & Fan, Q.M. 2008. Study for the particle's scale effect on some thermophysical properties of nanofluids by a simplified molecular dynamics method. *Engineering Analysis with Boundary Elements*, 32(4): 282–289.

Ma, H., Zhang, Y., Zhu, L., Majima, T. & Wang, N. 2021. Efficient activation of peroxymonosulfate on cobalt hydroxychloride nanoplates through hydrogen bond for degradation of tetrabromobisphenol A. *Chemical Engineering Journal*, 413: 127480.

Ma, J., Yuan, T., He, Y.S., Wang, J., Zhang, W., Yang, D., Liao, X. Z., & Ma, Z. F. 2014. A novel graphene sheet-wrapped $Co_2(OH)_3Cl$ composite as a long-life anode material for lithium ion batteries. *Journal of Materials Chemistry A*, *2*(40), 16925–16930.

Ma, R., Liu, Z., Takada, K., Fukuda, K., Ebina, Y., Bando, Y. & Sasaki, T. 2006. Tetrahedral Co(II) coordination in α-type cobalt hydroxide: Rietveld refinement and X-ray absorption spectroscopy. *Inorganic Chemistry*, 45(10): 3964–3969.

Ma, W., Feng, Y., Wang, L., Li, Y., Shi, M. & Cui, H. 2017. $Co_2(OH)_3Cl$ nanoparticles as new-type electrode material with high electrochemical performance for application in supercapacitor. *Advanced Powder Technology*, 28(10): 2642–2647.

Mahbubul, I.M., Saidur, R., Amalina, M.A. & Niza, M.E. 2016. Influence of ultrasonication duration on rheological properties of nanofluid: An experimental study with alumina-water nanofluid. *International Communications in Heat and Mass Transfer*, 76: 33–40.

Malik, M. M., Jeyakumar, M., Hamed, M. S., Walker, M. J., & Shankar, S. 2010. Rotational rheometry of liquid metal systems: Measurement geometry selection and flow curve analysis. *Journal of Non-Newtonian Fluid Mechanics*, *165*(13–14), 733–742.

Manoram, R.B. & Moorthy, R.S. 2022. Experimental investigation on energy and exergy analysis of solar water heating system using cobalt oxide based nanofluid. *Heat and mass transfer*, 58(1): 83–98.

Mansournia, M. & Rakhshan, N. 2017. Hydrothermal synthesis and tuning of size and morphology of α-$Co(OH)_2$ and α-$Co_2(OH)_3Cl$ nanostructures as precursors for nanosized Co_3O_4. *Ceramics International*, 43(9): 7282–7289.

Mariano, A., Pastoriza-Gallego, M.J., Lugo, L., Mussari, L. & Piñeiro, M.M. 2015. Co_3O_4 ethylene glycol-based nanofluids: thermal conductivity, viscosity and high pressure density. *International Journal of Heat and Mass Transfer*, 85: 54–60.

Matusiak, J. & Grządka, E. 2017. Stability of colloidal systems - a review of the stability measurements methods. *Annales Universitatis Mariae Curie-Sklodowska, sectio AA – Chemia*, 72(1): 33.

Maxwell, J.C. 1881. *Treatise on Electricity and Magnetism*. 3rd edition. J. J. Thomson, ed. London: Oxford University Press.

McNaught, A.D. & Wilkinson, A. 2014. *Compendium of Chemical Terminology*.

Mei, D., Fang, Y., Zhang, Z., Guo, D., Chen, Z. & Sun, C. 2021. Analysis of surface tension for nano-fuels containing disparate types of suspended nanoparticles. *Powder Technology*, 388: 526–536.

Meng, X. & Deng, D. 2017. A new approach to facilely synthesize crystalline $Co_2(OH)_3Cl$ microstructures in an eggshell reactor system. *CrystEngComm*, 19(21): 2953–2959.

Mezger, T.G. 2012. *The Rheology Handbook*. 4th ed. Vincentz Network.

Minakov, A. V., Guzei, D. V., Pryazhnikov, M.I., Zhigarev, V.A. & Rudyak, V.Y. 2016. Study of turbulent heat transfer of the nanofluids in a cylindrical channel. *International Journal of Heat and Mass Transfer*, 102: 745–755.

Minardi, J.E. & Chuang, H.N. 1975. Performance of a 'black' liquid flat-plate solar collector. *Solar Energy*, 17(3): 179–183.

Mingzheng, Z., Guodong, X., Jian, L., Lei, C. & Lijun, Z. 2012. Analysis of factors influencing thermal conductivity and viscosity in different kinds of surfactant solutions. *Experimental Thermal and Fluid Science*, 36: 22–29.

Mintsa, H.A., Roy, G., Nguyen, C.T. & Doucet, D. 2009. New temperature dependent thermal conductivity data for water-based nanofluids. *International Journal of Thermal Sciences*, 48(2): 363–371.

Mitchell, J.G. & Kogure, K. 2006. Bacterial motility: Links to the environment and a driving force for microbial physics. *FEMS Microbiology Ecology*, 55(1): 3–16.

Mitra, D., Kumar Chattopadhyay, K. & Chattopadhyay, P. 2021. Generation of stable thermal gradient by solar energy harvesting in porous cobalt oxide based nanofluid. *Sustainable Energy Technologies and Assessments*, 47: 101390.

Moghadassi, A.R., Hosseini, S.M. & Henneke, D.E. 2010. Effect of CuO nanoparticles in enhancing the thermal conductivities of monoethylene glycol and paraffin fluids. *Industrial and Engineering Chemistry Research*, 49(4): 1900–1904.

Mohammadfam, Y. & Zeinali Heris, S. 2023. Thermophysical characteristics and forced convective heat transfer of ternary doped magnetic nanofluids in a circular tube: An experimental study. *Case Studies in Thermal Engineering*, 52: 103748.

Moldovan, D., Yamakov, V., Wolf, D. & Phillpot, S.R. 2002. Scaling behavior of grain-rotation-induced grain growth. *Physical Review Letters*, 89(20): 206101.

Mukherjee, S. & Paria, S. 2013. Preparation and stability of nanofluids-a review. *IOSR Journal of Mechanical and Civil Engineering (IOSR-JMCE*, 9(2): 63–69.

Mullin, J.W. 2001. *Crystallization*. 4th edition. Butterworth-Heinemann.

Murshed, S.M.S., Leong, K.C. & Yang, C. 2008. Investigations of thermal conductivity and viscosity of nanofluids. *International Journal of Thermal Sciences*, 47(5): 560–568.

Nadooshan, A.A., Eshgarf, H. & Afrand, M. 2018. Evaluating the effects of different parameters on rheological behavior of nanofluids: a comprehensive review. *Powder Technology*, 338: 342–353.

Nallusamy, S. 2015. Thermal conductivity analysis and characterization of copper oxide nanofluids through different techniques. *Journal of Nano Research*, 40: 102–112.

Namburu, P.K., Das, D.K., Tanguturi, K.M. & Vajjha, R.S. 2009. Numerical study of turbulent flow and heat transfer characteristics of nanofluids considering variable properties. *International Journal of Thermal Sciences*, 48(2): 290–302.

Namburu, P.K., Kulkarni, D.P., Dandekar, A. & Das, D.K. 2007. Experimental investigation of viscosity and specific heat of silicon dioxide nanofluids. *Micro and Nano Letters*, 2(3): 67–71.

Nandkishor, P. & Omprakash, C. 2020. Effect of particle size, shape upon rheological properties of methanol based nanofluids at 303 K. *Recent Trends in Mathematical, Physical, Chemical, Library*, A7: 326-330.

Nassar, M.Y. & Ahmed, I.S. 2011. Hydrothermal synthesis of cobalt carbonates using different counter ions: an efficient precursor to nano-sized cobalt oxide (Co_3O_4). *Polyhedron*, 30(15): 2431–2437.

Nguyen, C.T., Desgranges, F., Galanis, N., Roy, G., Maré, T., Boucher, S. & Angue Mintsa, H. 2008. Viscosity data for Al_2O_3-water nanofluid-hysteresis: is heat transfer enhancement using nanofluids reliable? *International Journal of Thermal Sciences*, 47(2): 103–111.

Nguyen, C.T., Desgranges, F., Roy, G., Galanis, N., Maré, T., Boucher, S. & Angue Mintsa, H. 2007. Temperature and particle-size dependent viscosity data for water-based nanofluids - hysteresis phenomenon. *International Journal of Heat and Fluid Flow*, 28(6): 1492–1506.

Nguyen, T.D. & Do, T.O. 2011. Size- and shape-controlled synthesis of monodisperse metal oxide and mixed oxide nanocrystals. In Masuda Y. *Nanocrystal*. IntechOpen.

Noroozi, M., Radiman, S. & Zakaria, A. 2014. Influence of sonication on the stability and thermal properties of Al_2O_3 nanofluids. *Journal of Nanomaterials*, 2014.

Oh, D.W., Jain, A., Eaton, J.K., Goodson, K.E. & Lee, J.S. 2008. Thermal conductivity measurement and sedimentation detection of aluminium oxide nanofluids by using the 3ω method. *International Journal of Heat and Fluid Flow*, 29(5): 1456–1461.

Oskam, G. 2006. Metal oxide nanoparticles: synthesis, characterization and application. In *Journal of Sol-Gel Science and Technology*. 161–164.

Ostwald, W. 1897. Studien über die Bildung und Umwandlung fester Körper. *Zeitschrift für Physikalische Chemie*, 22U(1): 289–330. [Language used is that of article.]

Ostwald, W. 1900. Über die vermeintliche Isomerie des roten und gelben Quecksilberoxyds und die Oberflächenspannung fester Körper. *Zeitschrift für Physikalische Chemie*, 34U(1): 495–503. [Language used is that of article.]

Oswald, H.R. & Feitknecht, W. 1964. About the hydroxide halides $Me_2(OH)_3Cl$, -Br, -J of divalent metals (Me= Mg, Ni, Co, Cu, Fe, Mn). *Helvetica Chimica Acta*, 47(1): 272–289.

Otanicar, T.P., Phelan, P.E. & Golden, J.S. 2009. Optical properties of liquids for direct absorption solar thermal energy systems. *Solar Energy*, 83(7): 969–977.

Otanicar, T.P., Phelan, P.E., Prasher, R.S., Rosengarten, G. & Taylor, R.A. 2010. Nanofluid-based direct absorption solar collector. *Journal of Renewable and Sustainable Energy*, 2(3): 33102.

Özerinç, S., Kakaç, S. & Yazlcloğlu, A.G. 2010. Enhanced thermal conductivity of nanofluids: A state-of-the-art review. *Microfluidics and Nanofluidics*, 8(2): 145–170.

Park, G.D., Ko, Y.N. & Kang, Y.C. 2014. Electrochemical properties of cobalt hydroxychloride microspheres as a new anode material for Li-ion batteries. *Scientific Reports*, 4(1): 1–7.

Paradis, P.L., Rousse, D.R., Hallé, S., Lamarche, L. & Quesada, G. 2015. Thermal modeling of evacuated tube solar air collectors. *Solar Energy*, 115: 708–721.

Pastoriza-Gallego, M.J., Casanova, C., Legido, J.L. & Piñeiro, M.M. 2011. CuO in water nanofluid: Influence of particle size and polydispersity on volumetric behaviour and viscosity. *Fluid Phase Equilibria*, 300(1–2): 188–196.

Patil, M.S., Seo, J.H., Kang, S.J. & Lee, M.Y. 2016. Review on synthesis, thermo-physical property, and heat transfer mechanism of nanofluids. *Energies,* 9(10): 840.

Patil, P.G. 1975. Field performance and operation of a flat-glass solar heat collector. *Solar Energy*, 17(2): 111–117.

Peng, X., Wickham, J. & Alivisatos, A.P. 1998. Kinetics of II-VI and III-V colloidal semiconductor nanocrystal growth: "focusing" of size distributions. *Journal of the American Chemical Society*, 120(21): 5343–5344.

Penn, R.L. & Banfield, J.F. 1999. Morphology development and crystal growth in nanocrystalline aggregates under hydrothermal conditions: Insights from titania. *Geochimica et Cosmochimica Acta*, 63(10): 1549–1557.

Penn, R.L. 2004. Kinetics of oriented aggregation. *Journal of Physical Chemistry B*, 108(34): 12707–12712.

Petzold, G., Rojas-Reyna, R., Mende, M. & Schwarz, S. 2009. Application relevant characterization of aqueous silica nanodispersions. *Journal of Dispersion Science and Technology*, 30(8): 1216–1222.

Pietsch, W. 2004. *Agglomeration in industry: occurrence and applications*. Weinheim, Wiley-VCH.

Piriyawong, V., Thongpool, V., Asanithi, P. & Limsuwan, P. 2012. Preparation and characterization of alumina nanoparticles in deionized water using laser ablation technique. *Journal of Nanomaterials*, 2012.

Prasad, D.M.R., Senthilkumar, R., Lakshmanarao, G., Krishnan, S. & Naveen Prasad, B.S. 2019. A critical review on thermal energy storage materials and systems for solar applications. *AIMS Energy*, 7(4): 507–526.

Prasher, R., Evans, W., Meakin, P., Fish, J., Phelan, P. & Keblinski, P. 2006. Effect of aggregation on thermal conduction in colloidal nanofluids. *Applied Physics Letters*, 89(14): 143119.

Prasher, R., Song, D., Wang, J. & Phelan, P. 2006. Measurements of nanofluid viscosity and its implications for thermal applications. *Applied Physics Letters*, 89(13): 133108.

Předota, M., Machesky, M.L. & Wesolowski, D.J. 2016. Molecular origins of the zeta potential. *Langmuir*, 32(40): 10189–10198.

Pyrz, W.D. & Buttrey, D.J. 2008. Particle size determination using TEM: a discussion of image acquisition and analysis for the novice microscopist. *Langmuir*, 24(20): 11350–11360.

Rabenau, A. 1985. The role of hydrothermal synthesis in preparative Chemistry. *Angewandte Chemie International Edition in English*, 24(12): 1026–1040.

Rahman Salari, S., Khavarpour, M., Masoumi, M. & Mosivand, S. 2022. Preparation of cobalt oxide and tin dioxide nanofluids and investigation of their thermophysical properties. *Microfluidics and Nanofluidics*, 26(10): 1–16.

Rajaee, F., Rad, M.A.V., Kasaeian, A., Mahian, O. & Yan, W.M. 2020. Experimental analysis of a photovoltaic/thermoelectric generator using cobalt oxide nanofluid and phase change material heat sink. *Energy Conversion and Management*, 212: 112780.

Raki, E., Afrand, M. & Abdollahi, A. 2021. Influence of magnetic field on boiling heat transfer coefficient of a magnetic nanofluid consisting of cobalt oxide and deionized water in nucleate regime: An experimental study. *International Journal of Heat and Mass Transfer*, 165: 120669.

Ranganatha, S., Kumar, S., Penki, T.R., Kishore, B. & Munichandraiah, N. 2017. $Co_2(OH)_3Cl$ xerogels with 3D interconnected mesoporous structures as a novel high-performance supercapacitor material. *Journal of Solid State Electrochemistry*, 21(1): 133–143.

Rashidi, S., Esfahani, J.A. & Rashidi, A. 2017. A review on the applications of porous materials in solar energy systems. *Renewable and Sustainable Energy Reviews*, 73: 1198–1210.

Ravi Dhas, C., Venkatesh, R., Jothivenkatachalam, K., Nithya, A., Suji Benjamin, B., Moses Ezhil Raj, A., Jeyadheepan, K. & Sanjeeviraja, C. 2015. Visible light driven photocatalytic degradation of Rhodamine B and Direct Red using cobalt oxide nanoparticles. *Ceramics International*, 41(8): 9301–9313.

Ren, P., Song, M., Lee, J., Zheng, J., Lu, Z., Engelhard, M., Yang, X., Li, X., Kisailus, D. & Li, D. 2019. Edge dislocations induce improved photocatalytic efficiency of colored TiO_2. *Advanced Materials Interfaces*, 6(17): 1901121.

Riahi, A., Khamlich, S., Balghouthi, M., Khamliche, T., Doyle, T. B., Dimassi, W., Guizani, A., & Maaza, M. 2020. Study of thermal conductivity of synthesized Al_2O_3-water nanofluid by pulsed laser ablation in liquid. *Journal of Molecular Liquids*, *304*, 112694.

Ribeiro, C., Lee, E.J.H., Longo, E. & Leite, E.R. 2005. A kinetic model to describe nanocrystal growth by the Oriented attachment mechanism. *ChemPhysChem*, 6(4): 690–696.

Ritchie, I.T. & Window, B. 1977. Applications of thin graded-index films to solar absorbers. *Applied Optics*, 16(5): 1438.

Rocha, F.S., Gomes, A.J., Lunardi, C.N., Kaliaguine, S. & Patience, G.S. 2018. Experimental methods in Chemical Engineering: Ultraviolet visible spectroscopy—UV-Vis. *The Canadian Journal of Chemical Engineering*, 96(12): 2512–2517.

Rubbi, F., Das, L., Habib, K., Aslfattahi, N., Saidur, R. & Rahman, M.T. 2021. State-of-the-art review on water-based nanofluids for low temperature solar thermal collector application. *Solar Energy Materials and Solar Cells*, 230: 111220.

Rudyak, V.Y., Minakov, A. V. & Krasnolutskii, S.L. 2016. Physics and mechanics of heat exchange processes in nanofluid flows. *Physical Mesomechanics*, 19(3): 298–306.

Sahoo, P., Djieutedjeu, H. & Poudeu, P.F.P. 2013. Co_3O_4 nanostructures: The effect of synthesis conditions on particles size, magnetism and transport properties. *Journal of Materials Chemistry A*, 1(47): 15022–15030.

Saidina, D.S., Abdullah, M.Z. & Hussin, M. 2020. Metal oxide nanofluids in electronic cooling: a review. *Journal of Materials Science: Materials in Electronics*, 31(6): 4381–4398.

Sampanthar, J.T. & Zeng, H.C. 2002. Arresting butterfly-like intermediate nanocrystals of β-$Co(OH)_2$ via ethylenediamine-mediated synthesis. *Journal of the American Chemical Society*, 124(23): 6668–6675.

San Martin, R.L. & Fjeld, G.J. 1975. Experimental performance of three solar collectors. *Solar Energy*, 17(6): 345–349.

Sani, E., Mercatelli, L., Barison, S., Pagura, C., Agresti, F., Colla, L. & Sansoni, P. 2011. Potential of carbon nanohorn-based suspensions for solar thermal collectors. *Solar Energy Materials and Solar Cells*, 95(11): 2994–3000.

Sarviya, R.M. & Fuskele, V. 2017. Review on thermal conductivity of nanofluids. *Materials Today: Proceedings*, 4(2): 4022–4031.

Sekhar, T., Nandan, G., Prakash, R. & Muthuraman, M. 2018. Investigations on viscosity and thermal conductivity of cobalt oxide-water nano fluid. *Materials Today: Proceedings*, 5(2): 6176–6182.

Sekhar, T.V.R., Prakash, R., Nandan, G. & Muthuraman, M. 2017. Preparation of Co_3O_4-H_2O nanofluid and application to CR-60 concentrating solar collector. *Progress in Industrial Ecology*, 11(3): 227–246.

Sengers, J.V. & Watson, J.T.R. 1986. Improved international formulations for the viscosity and thermal conductivity of water substance. *Journal of Physical and Chemical Reference Data*, 15(4): 1291–1314.

Serrano de la Rosa, L., Portillo Moreno, O., Portillo, M.C., Téllez, V.C., Mora-Ramírez, M.A., Santiesteban, H.J. & Castillo, M.P. 2021. Maxwell-Boltzmann statistics to elucidate the luminescent emission bands in $Co(OH)_2$ and Co_3O_4 nanocrystals. *Optik*, 227: 165473.

Setia, H., Gupta, R. & Wanchoo, R.K. 2013. Stability of nanofluids. *Materials Science Forum*, 757: 139–149.

Shafiee, S. & Topal, E. 2009. When will fossil fuel reserves be diminished? *Energy Policy*, 37(1): 181–189.

Singh, A.K. & Raykar, V.S. 2008. Microwave synthesis of silver nanofluids with polyvinylpyrrolidone (PVP) and their transport properties. *Colloid and Polymer Science*, 286(14–15): 1667–1673.

Singh, A.K. 2008. Thermal conductivity of nanofluids. *Defence Science Journal*, 58(5): 600–607.

Sinkó, K., Szabó, G. & Zrínyi, M. 2011. Liquid-phase synthesis of cobalt oxide nanoparticles. *Journal of Nanoscience and Nanotechnology*, 11(5): 4127–35.

Son, Y., No, Y. & Kim, J. 2020. Geometric and operational optimization of 20-kHz probe-type sonoreactor for enhancing sonochemical activity. *Ultrasonics Sonochemistry*, 65: 105065.

Špeťuch, V., Petrík, J., Grambálová, E., Medveď, D., & Palfy, P. 2015. The capability of the viscosity measurement process. *Acta Metallurgica Slovaca*, 21(1), 53–60.

Su, F., Ma, X. & Lan, Z. 2011. The effect of carbon nanotubes on the physical properties of a binary nanofluid. *Journal of the Taiwan Institute of Chemical Engineers*, 42(2): 252–257.

Suganthi, K.S. & Rajan, K.S. 2017. Metal oxide nanofluids: review of formulation, thermo-physical properties, mechanisms, and heat transfer performance. *Renewable and Sustainable Energy Reviews*, 76: 226–255.

Sugimoto, T. 2007. Underlying mechanisms in size control of uniform nanoparticles. *Journal of Colloid and Interface Science*, 309(1): 106–118.

Suman, S., Khan, M.K. & Pathak, M. 2015. Performance enhancement of solar collectors - a review. *Renewable and Sustainable Energy Reviews*, 49: 192–210.

Sundar, L.S., Sharma, K.V., Naik, M.T. & Singh, M.K. 2013. Empirical and theoretical correlations on viscosity of nanofluids: A review. *Renewable and Sustainable Energy Reviews*, 25: 670–686.

Tang, S., Tang, Y., Vongehr, S., Zhao, X. & Meng, X. 2009. Nanoporous carbon spheres and their application in dispersing silver nanoparticles. *Applied Surface Science*, 255(11): 6011–6016.

Tehrani, A.A., Omranpoor, M.M., Vatanara, A., Seyedabadi, M. & Ramezani, V. 2019. Formation of nanosuspensions in bottom-up approach: theories and optimization. *DARU Journal of Pharmaceutical Sciences*, 27(1): 451.

Teng, T.P., Hung, Y.H., Teng, T.C., Mo, H.E. & Hsu, H.G. 2010. The effect of alumina/water nanofluid particle size on thermal conductivity. *Applied Thermal Engineering*, 30(14–15): 2213–2218.

Tian, L., Huang, K., Liu, Y. & Liu, S. 2011. Topotactic synthesis of Co_3O_4 nanoboxes from $Co(OH)_2$ nanoflakes. *Journal of Solid State Chemistry*, 184(11): 2961–2965.

Timofeeva, E.V., Routbort, J.L. & Singh, D. 2009. Particle shape effects on thermophysical properties of alumina nanofluids. *Journal of Applied Physics*, 106(1): 014304.

Timofeeva, E. V., Smith, D.S., Yu, W., France, D.M., Singh, D. & Routbort, J.L. 2010. Particle size and interfacial effects on thermo-physical and heat transfer characteristics of water-based α-SiC nanofluids. *Nanotechnology*, 21(21): 215703.

Turian, R.M., Sung, D.J. & Hsu, F.L. 1991. Thermal conductivity of granular coals, coal-water mixtures and multi-solid/liquid suspensions. *Fuel*, 70(10): 1157–1172.

Tyagi, H., Phelan, P. & Prasher, R. 2009. Predicted efficiency of a Low-temperature Nanofluid-based direct absorption solar collector. *Journal of Solar Energy Engineering, Transactions of the ASME*, 131(4): 0410041–0410047.

Vargas, J.V.C., Ordonez, J.C., Hovsapian, R. & Dias, F.G. 2009. Modeling, simulation and optimization of a solar system for water heating and absorption cooling. In *2008 Proceedings of the 2nd International Conference on Energy Sustainability*, 2: 489–498.

Verwey, E.J.W., Overbeek, J.T.G. & van Nes, K. 1948. *Theory of the Stability of Lyophobic Colloids: The Interaction of Sol Particles Having an Electric Double Layer*. Elsevier

Vickers, D., Archer, L.A. & Floyd-Smith, T. 2009. Synthesis and characterization of cubic cobalt oxide nanocomposite fluids. *Colloids and Surfaces A: Physicochemical and Engineering Aspects*, 348(1–3): 39–44.

Voorhees, P.W. 1985. The theory of Ostwald ripening. *Journal of Statistical Physics*, 38(1–2): 231–252.

Wagner, C. 1961. Theorie der Alterung von Niederschlägen durch Umlösen (Ostwald-Reifung). *Zeitschrift für Elektrochemie, Berichte der Bunsengesellschaft für physikalische Chemie*, 65(7–8): 581–591. [Language used is that of article.]

Wang, G., Liang, J., Li, D., Li, M. & Li, L. 2022. Formation of hierarchical cobalt hydroxychloride nanostructures with enhanced performance for lithium-ion batteries. *Crystal Research and Technology*, 57(3): 2100133.

Wang, J.J., Zheng, R.T., Gao, J.W. & Chen, G. 2012. Heat conduction mechanisms in nanofluids and suspensions. *Nano Today*, 7(2): 124–136.

Wang, X., Peng, Q., Zhu, W. & Lei, G. 2015. High performance of inverted polymer solar cells with cobalt oxide as hole-transporting layer. *Semiconductor Science and Technology*, 30(5): 1–5.

Wang, X., Xu, X. & Choi, S.U.S. 1999. Thermal conductivity of nanoparticle-fluid mixture. *Journal of thermophysics and heat transfer*, 13(4): 474–480.

Wang, X., Zhang, N., Zhang, S., Chen, X., Chen, L. & Shao, G. 2019. A novel compound $Co_2(OH)_3Cl$ as a long-life supercapacitor electrode material. *Materials Letters*, 237: 344–347.

Wang, Z., Hong, P., Peng, S., Zhang, X., Zou, T., Yang, Y., Zhao, R. & Wang, Y. 2020. Hierarchitecture $Co_2(OH)_3Cl@FeCo_2O_4$ composite as a novel and high-performance electrode material applied in supercapacitor. *International Journal of Energy Research*, 44(4): 3122–3133.

Wei, X. & Wang, L. 2010. Synthesis and thermal conductivity of microfluidic copper nanofluids. *Particuology*, 8(3): 262–271.

Wei, X., Zhu, H., Kong, T. & Wang, L. 2009. Synthesis and thermal conductivity of Cu_2O nanofluids. *International Journal of Heat and Mass Transfer*, 52(19–20): 4371–4374.

Werz, T., Baumann, M., Wolfram, U. & Krill, C.E. 2014. Particle tracking during Ostwald ripening using time-resolved laboratory X-ray microtomography. *Materials Characterization*, 90: 185–195.

Witharana, S., Hodges, C., Xu, D., Lai, X. & Ding, Y. 2012. Aggregation and settling in aqueous polydisperse alumina nanoparticle suspensions. *Journal of Nanoparticle Research*, 14(5): 1–11.

Wole-Osho, I., Okonkwo, E.C., Abbasoglu, S. & Doga, K. 2020. Nanofluids in solar thermal collectors: review and limitations compound parabolic collector. *International Journal of Thermophysics*, 41: 157.

Won, D. & Kim, C. 2004. Alignment and aggregation of spherical particles in viscoelastic fluid under shear flow. *Journal of Non-Newtonian Fluid Mechanics*, 117(2–3): 141–146.

Xian-Ju, W. & Xin-Fang, L. 2009. Influence of pH on nanofluids' viscosity and thermal conductivity. *Chinese Physics Letters*, 26(5): 056601.

Xie, H., Wang, J., Xi, T. & Liu, Y. 2002. Thermal conductivity of suspensions containing nanosized SiC particles. *International Journal of Thermophysics*, 23(2): 571–580.

Xu, G., Fu, J., Dong, B., Quan, Y. & Song, G. 2019. A novel method to measure thermal conductivity of nanofluids. *International Journal of Heat and Mass Transfer*, 130: 978–988.

Xuan, Y. & Li, Q. 2003. Investigation on convective heat transfer and flow features of nanofluids. *ASME Journal of Heat Transfer*, 125(1): 151-155.

Xuan, Y., Li, Q. & Hu, W. 2003. Aggregation structure and thermal conductivity of nanofluids. *AIChE Journal*, 49(4): 1038–1043.

Yang, B. & Han, Z.H. 2006. Temperature-dependent thermal conductivity of nanorod-based nanofluids. *Applied Physics Letters*, 89(8): 083111.

Yang, L. & Du, K. 2020. A comprehensive review on the natural, forced, and mixed convection of non-Newtonian fluids (nanofluids) inside different cavities. *Journal of Thermal Analysis and Calorimetry*, 140(5): 2033–2054.

Yang, L., Guan, W., Bai, B., Xu, Q. & Xiang, Y. 2010. Synthesis of yeast-assisted Co_3O_4 hollow microspheres—a novel biotemplating technique. *Journal of Alloys and Compounds*, 504(1): L10–L13.

Yang, X.F. & Liu, Z.H. 2011. Pool boiling heat transfer of functionalized nanofluid under sub-atmospheric pressures. *International Journal of Thermal Sciences*, 50(12): 2402–2412.

Yasmin, H., Giwa, S.O., Noor, S. & Sharifpur, M. 2023. Thermal conductivity enhancement of metal oxide nanofluids: a critical review. *Nanomaterials,* 13(3): 597.

Yoo, D.H., Hong, K.S. & Yang, H.S. 2007. Study of thermal conductivity of nanofluids for the application of heat transfer fluids. *Thermochimica Acta*, 455(1–2): 66–69.

Yu, C.J., Richter, A.G., Datta, A., Durbin, M.K. & Dutta, P. 2000. Molecular layering in a liquid on a solid substrate: an X-ray reflectivity study. *Physica B: Condensed Matter*, 283(1–3): 27–31.

Yu, W. & Choi, S.U.S. 2003. The role of interfacial layers in the enhanced thermal conductivity of nanofluids: a renovated Maxwell model. *Journal of Nanoparticle Research*, 5: 167–171.

Yu, W. & Choi, S.U.S. 2004. The role of interfacial layers in the enhanced thermal conductivity of nanofluids: a renovated Hamilton-Crosser model. *Journal of Nanoparticle Research*, 6(4): 355–361.

Yu, W. & Xie, H. 2012. A review on nanofluids: preparation, stability mechanisms, and applications. *Journal of Nanomaterials*, 2012.

Yu, W., France, D.M., Routbort, J.L. & Choi, S.U.S. 2008. Review and comparison of nanofluid thermal conductivity and heat transfer enhancements. *Heat Transfer Engineering*, 29(5): 432–460.

Yüksel, N. 2016. The Review of some commonly used methods and techniques to measure the thermal conductivity of insulation materials. In Almusaed, A. & Almssad, A. (eds.) *Insulation Materials in Context of Sustainability*. IntechOpen.

Zafarani-Moattar, M.T. & Majdan-Cegincara, R. 2012. Effect of temperature on volumetric and transport properties of nanofluids containing ZnO nanoparticles poly(ethylene glycol) and water. *Journal of Chemical Thermodynamics*, 54: 55–67.

Zanatta, A.R. 2019. Revisiting the optical bandgap of semiconductors and the proposal of a unified methodology to its determination. *Scientific reports*, 9(1): 11225.

Zenmyo, K. & Tokita, M. 2009. Magnetic structure of geometrically frustrated compound $Co_2Cl(OH)_3$ determined by proton NMR. *Journal of Magnetism and Magnetic Materials*, 321(14): 2192–2196.

Zhan, H., Deng, C., Shi, X.L., Wu, C., Li, X., Xie, Z., Wang, C. & Chen, Z.G. 2020. Correlation between the photocatalysis and growth mechanism of SnO_2 nanocrystals. *Journal of Physics D: Applied Physics*, 53(15): 154005.

Zhang, F., Wang, X., Liu, H., Liu, C., Wan, Y., Long, Y. & Cai, Z. 2019. Recent advances and applications of semiconductor photocatalytic technology. *Applied Sciences (Switzerland)*, 9(12): 2489.

Zhang, H., Yang, Z., Zhang, X. & Mao, N. 2014. Photocatalytic effects of wool fibers modified with solely TiO_2 nanoparticles and N-doped TiO_2 nanoparticles by using hydrothermal method. *Chemical Engineering Journal*, 254: 106–114.

Zhang, J., Huang, F. & Lin, Z. 2010. Progress of nanocrystalline growth kinetics based on oriented attachment. *Nanoscale*, 2(1): 18–34.

Zhang, T., Zou, Q., Cheng, Z., Chen, Z., Liu, Y. & Jiang, Z. 2021. Effect of particle concentration on the stability of water-based SiO_2 nanofluid. *Powder Technology*, 379: 457–465.

Zhang, Y., Chen, Y., Westerhoff, P., Hristovski, K. & Crittenden, J.C. 2008. Stability of commercial metal oxide nanoparticles in water. *Water Research*, 42(8–9): 2204–2212.

Zhao, Zhigang, Geng, F., Bai, J. & Cheng, H.M. 2007. Facile and controlled synthesis of 3D nanorods-based urchinlike and nanosheets-based flowerlike cobalt basic salt nanostructures. *Journal of Physical Chemistry C*, 111(10): 3848–3852.

Zhao, Zihua, Liang, F., Hu, P., Guo, L., Zhong, Q., He, L. & Chen, C. 2007. Nanorods of ammine cobalt chloride $[Co(NH_3)_6Cl_3]$: Synthesis, characterization, and magnetic properties. *Physica E: Low-dimensional Systems and Nanostructures*, 39(1): 99–102.

Zhu, H.T., Lin, Y.S. & Yin, Y.S. 2004. A novel one-step chemical method for preparation of copper nanofluids. *Journal of Colloid and Interface Science*, 277(1): 100–103.

Zhuang, Z., Zhang, J., Huang, F., Wang, Y. & Lin, Z. 2009. Pure multistep Oriented attachment growth kinetics of surfactant-free SnO_2 nanocrystals. *Physical Chemistry Chemical Physics*, 11(38): 8516–8521.

Zwinkels, J.C. 2015. Light, Electromagnetic Spectrum. In Luo, M.R. (eds). *Encyclopedia of Color Science and Technology*. Springer Berlin Heidelberg.

APPENDICES

APPENDIX A. Additional TEM images of $Co_2(OH)_3Cl$ nanoparticles synthesised from different propanol concentrations

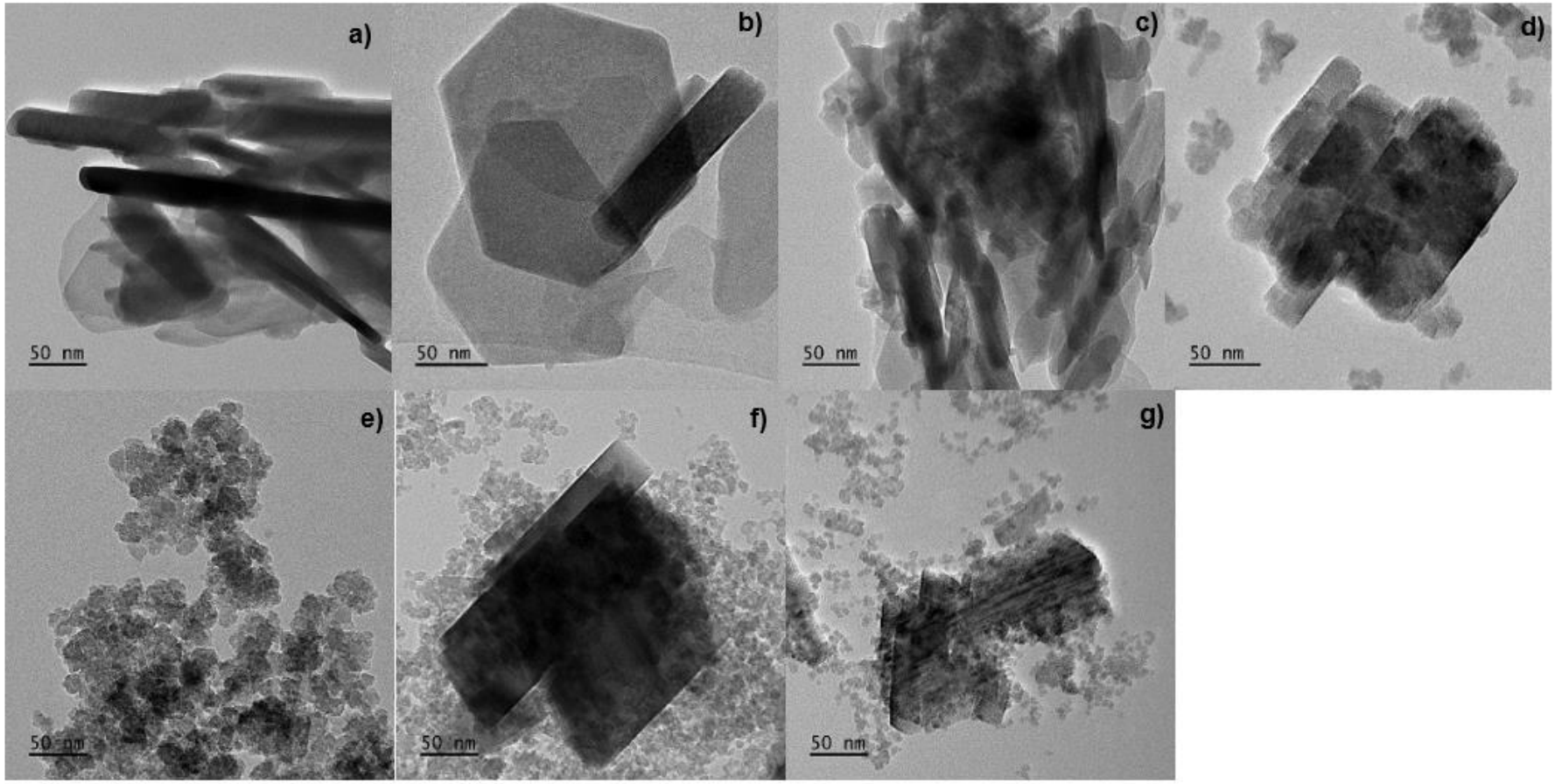

Figure A.1: $Co_2(OH)_3Cl$ nanoparticles synthesised in propanol concentrations at a) 0%, b) 10%, c) 30%, d) 70%, e) 95%, f) 98% and g) 100%

APPENDIX B. Additional TEM images of $Co_2(OH)_3Cl$ nanoparticles synthesised in water at different synthesis times

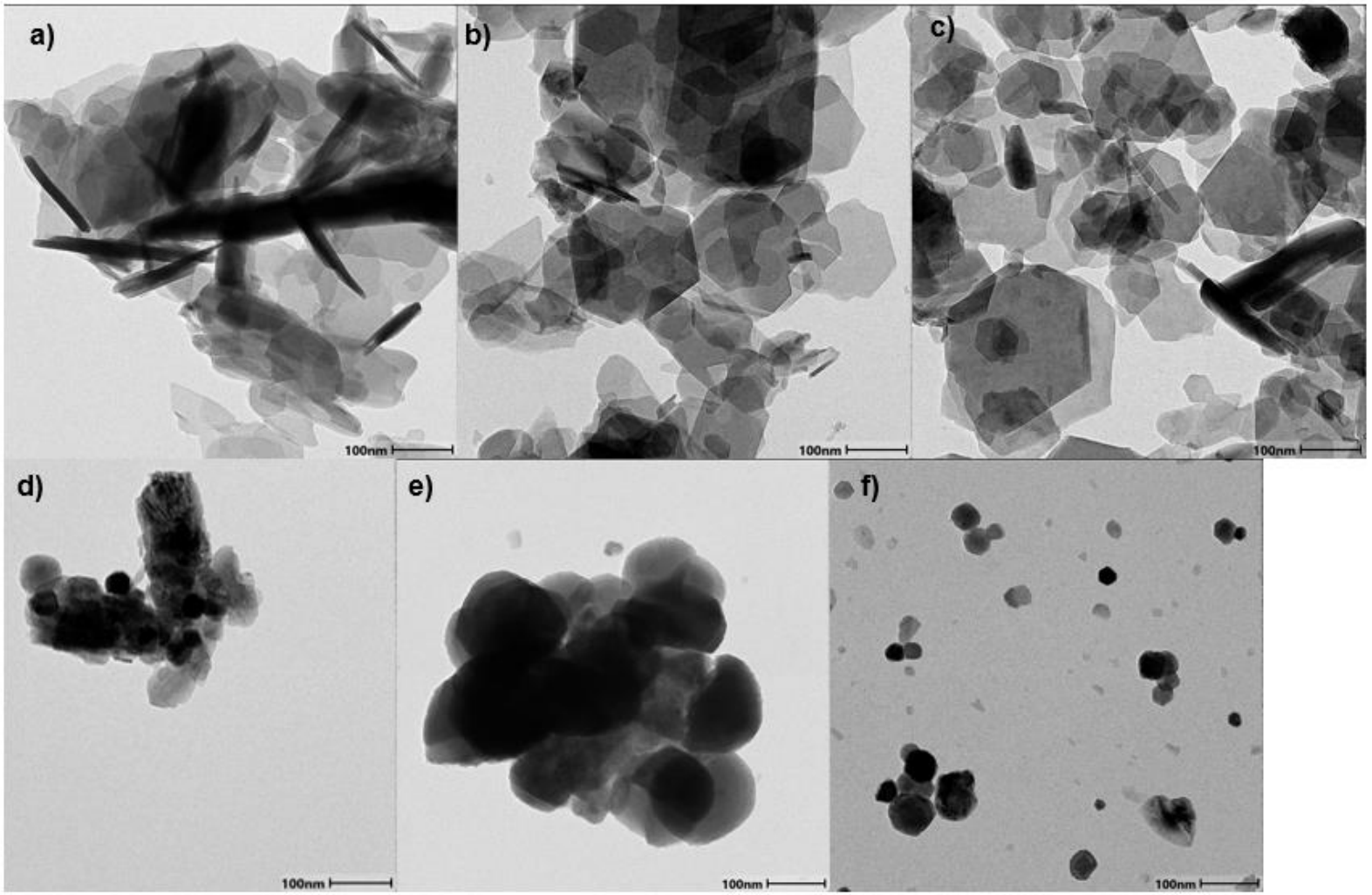

Figure B.1: $Co_2(OH)_3Cl$ nanoparticles synthesised in water after a) 60 min, b) 180 min, c) 360 min, d) 540 min, e) 720 min and g) 960 min

APPENDIX C. TEM images of $Co_2(OH)_3Cl$ nanoparticles synthesised in 70% propanol for 540 min and 720 min

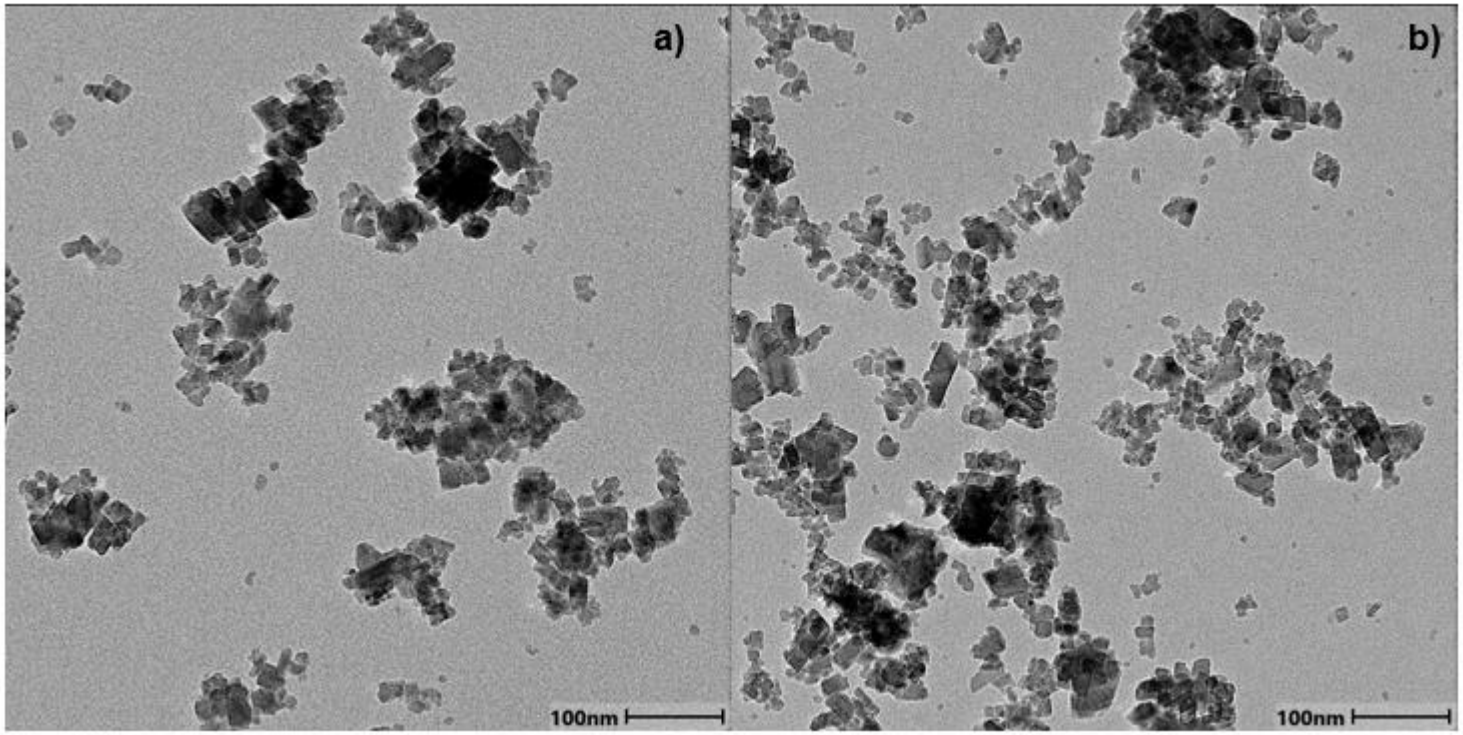

Figure C.1: $Co_2(OH)_3Cl$ nanoparticles synthesised in 70% propanol after a) 540 min and b) 720 min